Positioning and addressing single molecule magnets with an STM tip

Rabei Barhoumi

UNIVERSITÉ DE STRASBOURG

ÉCOLE DOCTORALE DE PHYSIQUE ET CHIMIE-PHYSIQUE

INSTITUT DE PHYSIQUE ET DE CHIMIE DES MATERIAUX DE STRASBOURG

THÈSE présentée par :

Rabei BARHOUMI

Soutenue le : **30 septembre 2019**

Pour obtenir le grade de : **Docteur de l'université de Strasbourg**

Discipline/ Spécialité: Physique / Nanophysique

Positioning and addressing single molecule magnets with an STM tip

THÈSE dirigée par :

Pr. Jean-Pierre BUCHER Directeur de Thèse, Université de Strasbourg

et co-dirigée par :

Pr. Mario RUBEN Co-directeur de Thèse, Institut de technologie de Karlsruhe

RAPPORTEURS :

Dr. Franck BALESTRO Rapporteur, Université de Grenoble-Alpes

Pr. Uta SCHLICKUM Rapporteuse, Université de Braunschweig

EXAMINATEURS :

Pr. Bernard DOUDIN Examinateur, Université de Strasbourg

Pr. Eva RENTSCHLER Examinatrice, Université de Mainz

Remerciements

Ce travail de thèse a été effectué au sein de l'institut de physique et chimie des Matériaux à Strasbourg (IPCMS). Tout d'abord je remercie la direction de m'avoir accueilli et accordé sa confiance. Je remercie profondément le professeur Jean-Pierre Bucher ainsi que le professeur Mario Ruben de m'avoir permis d'effectuer ce doctorat.

Je souhaite remercier Uta Schlickum, professeure à l'université de Braunschweig ainsi que Franck Balestro, chercheur à l'université Grenoble Alpes pour avoir accepté d'´évaluer ce travail en tant que rapporteur. Je remercie également la professeure Eva Rentschler de l'université Johannes Gutenberg de Mainz ainsi que le professeur Bernard Doudin de l'université de Strasbourg pour leurs participations au jury de thèse.

Je remercie également Nicolas Beyer et Christophe Kieber pour leur aide technique et matérielle, ainsi que Svetlana Klyatskaya pour la synthèse de molécules, qui était nécessaire pour l'accomplissement de cette thèse. Je tiens à remercier Anis Amokrane pour son assistance et son aide avec le microscope pendant la période de démarrage de cette thèse.

Je tiens à remercier profondément ma famille, mes parents (Tlili et Khaddouja), mes frères (Mosbah, Majdi et Helmi) et ma sœur Lamia pour leur soutien tout au long de mon parcours doctoral. Je remercie également tous les membres de ma seconde famille, le beau-père Lotfi, la belle-mère Rabiia, le beau-Frère Akram et la belle-sœur Amal.

Une pensée particulière à mes amis et mes collèges avec lesquels j'ai partagé mon quotidien, je vous souhaite une bonne continuation.

Je ne pourrais pas finir ses remerciements sans mentionner celle qui était toujours là, à chaque instant, celle qui m'a soutenu dans les moments les plus difficiles, Ouns. Sans toi, je n'aurai jamais fait cette thèse. Tu as su me supporter quand je devenais pourtant insupportable. Cette thèse est aussi la tienne. Merci infiniment.

…… A mon grand amour Chifa

Table of contents

Chapter 3 : Structural properties of MPc_2 (M = Tb,Y) growth on metal surfaces Au(111), Ag(111) and Cu(111)

Chapter 4 : Kondo issue in lanthanide double-decker molecular magnets on metal surfaces with ligand and 4f electron contributions

Chapter 5 : Positioning $TbPc_2$ on the cavities of $Co(NC\text{-}Ph_n\text{-}CN)_3$ metal-organic networks

Résumé étendu

Ces dix dernières années, la physique de l'effet Kondo a connu un regain d'intérêt grâce au développement des nanotechnologies. Des études menées sur les objets de taille nanométrique tels que les boîtes quantiques, les nanotubes de carbones, les nanoparticules de composés intermétalliques ou encore la molécule unique. Depuis quelques temps, les molécules magnétiques adsorbées sur des surfaces métalliques offrent un terrain d'exploration de l'effet Kondo en basse dimensionnalité.

Avec l'essor de l'électronique moléculaire, discipline pour laquelle la molécule unique est la brique de base des composants électroniques. Des recherches approfondies se sont tournées vers l'étude de l'effet Kondo au sein des molécules adsorbées sur des surfaces métalliques. L'intérêt grandissant pour les molécules provient de la facilité de mise en œuvre ainsi que de la robustesse des systèmes qu'offre l'ingénierie chimique. Une classe de molécule intéressante est la classe des molécules $LnPc_2$ caractérisée par des propriétés magnétiques exceptionnelles telles que l'anisotropie magnétique élevée et le temps de relaxation lent, en font des candidats majeurs pour le codage de l'information.

Les études menées ces dernières années sur ces systèmes ont montré la difficulté de bien comprendre l'effet Kondo. En particulier, les interactions intramoléculaires entre les états 4f et les états π ainsi que les interactions avec le substrat métallique sont encore mal comprises à ce jour. De plus, sonder les électrons 4f avec une sonde locale reste un défi du fait de leurs extensions spatiales très localisées autour du noyau et des niveaux d'énergie profondes. Bien que les états 4f dans le lanthanide terbium (Tb), offrant le caractère magnétique aux molécules double-decker $TbPc_2$, n'ont jamais été mis en évidence jusqu'à ce jour.

La molécule $TbPc_2$ est constituée d'atome de lanthanide terbium pris en sandwich entre deux ligands de phtalocyanine (Pc). Pour les applications envisagées, il est important de comprendre l'influence du substrat sur les propriétés électroniques et magnétiques de la molécule. De plus, la formation de réseaux moléculaires périodiques nécessite, néanmoins, une synthèse de blocks moléculaires appropriés. Ces réseaux sont généralement basés sur les interactions non-covalentes, interactions hydrogène ou des interactions métal-ligand.

La première mise en évidence d'une résonance Kondo par spectroscopie tunnel au sein d'une molécule de $TbPc_2$ adsorbée sur Au(111) a été effectuée en 2011. Toutefois dans cette expérience, l'origine de l'effet Kondo ne réside pas dans l'interaction entre les électrons de conduction du substrat et le spin porté par le Tb, mais un spin résultant d'un électron non apparié dans le ligand Pc de la molécule. Les états 4f ont été sondés plus tard par spectroscopie tunnel dans les deux systèmes de $NdPc_2$/Cu(100) et de $DyPc_2$/Cu(111) grâce à la forte interaction entre le ligand et la surface.

C'est dans ce contexte que nous nous sommes intéressés à l'interface molécule/métal susceptible de présenter un effet Kondo original. L'interface est composé d'une molécule de MPc_2 (M=Tb, Y) en contact avec différents substrats métalliques Au(111), Ag(111) et Cu(111). La molécule YPc_2 non magnétique (états d et f sont vides) composée par un ion central Yttrium permet de faire un point de comparaison avec le $TbPc_2$ et de rendre compte du rôle des électrons 4f dans les propriétés électroniques et magnétiques moléculaires. Dans cette thèse les principaux objectifs ont été les suivant : étudier la structure des arrangements moléculaires, étudier les propriétés électroniques de la molécule MPc_2 sur différents substrats et mettre en évidence l'effet Kondo ainsi comprendre l'origine physique.

Le premier chapitre comporte une introduction au magnétisme moléculaire où nous présentons des éléments théoriques permettant de comprendre le comportement des centres magnétiques (Lanthanides) dans leur environnement moléculaire. Une deuxième partie concerne l'observation de l'effet Kondo sur un métal noble et sa modélisation par une résonance Fano, illustrée par quelques résultats expérimentaux publiés sur l'effet Kondo dans les molécules organiques ou métal-organiques.

Dans le deuxième chapitre nous présentons les méthodes expérimentales principalement dédiées à la préparation et à la caractérisation des échantillons sous ultravide. Nous décrivons les techniques de préparation des échantillons y compris les techniques d'évaporation moléculaires et métalliques. La caractérisation topographique ainsi que les mesures spectroscopiques de la conductance dI/dV sont réalisées à très basse température (4.6 K) à l'aide d'un microscope à effet tunnel (LT-STM) dont le principe de fonctionnement est également présenté.

Le troisième chapitre rapporte les mesures structurales obtenus sur les molécules $TbPc_2$ déposées sur différents substrats tel que Au(111), Ag(111) et Cu(111) ainsi que sur les molécules YPc_2 déposées sur Au(111). Les analyses topographiques démontrent que les

molécules apparaissent comme des structures à huit lobes correspondant à la distribution électronique du ligand supérieur, ces molécules s'adsorbent différemment en fonction de la nature de substrat. Sur l'Au(111) et sur Ag(111), les molécules adoptent deux configurations (Phases I et II comme montre la Figure 1 (a) et (b)), caractérisées par l'absence ou la présence des interactions latérales entre lobes des ligands adjacentes. Sur le Cu(111), les molécules ne sont pas aussi mobiles que sur les autres substrats, les molécules s'adsorbent cote à cote.

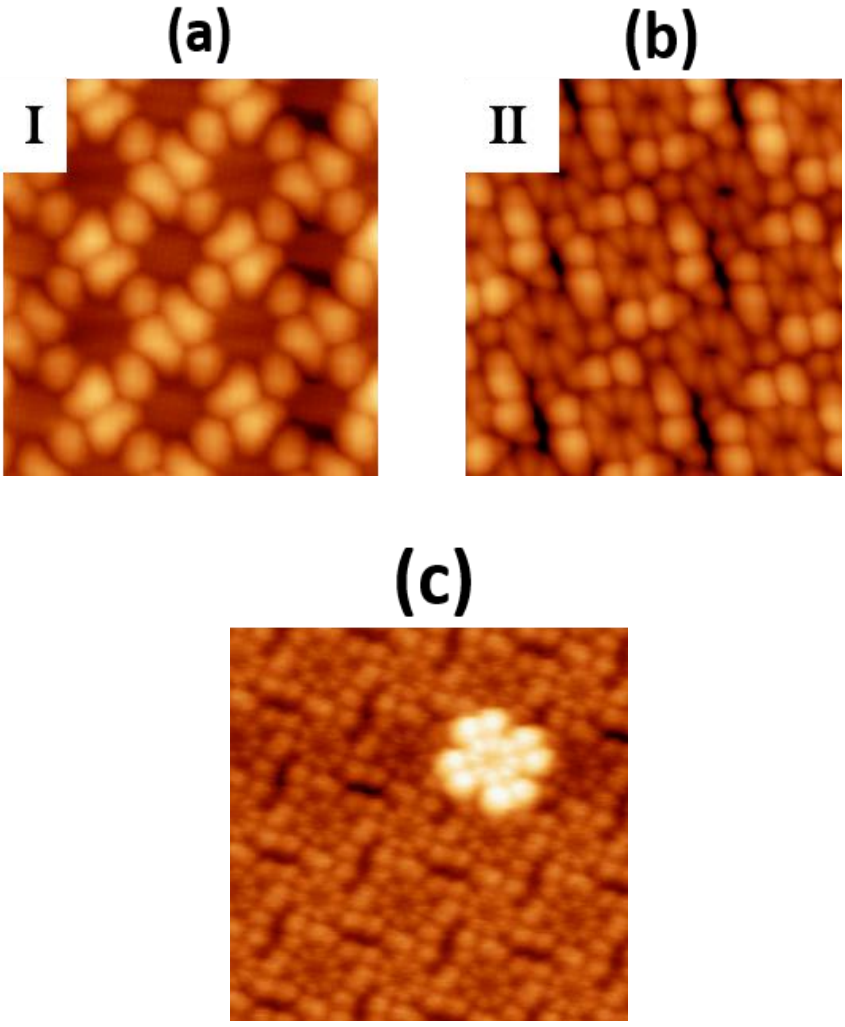

Figure 1 : Images STM topographiques de domaines d'adsorption de $TbPc_2$ sur Au(111) avec (a) Phase I et (b)Phase II et sur Ag(111) première et deuxième MC (c).

Ce chapitre revient aussi sur une étude de la molécule $TbPc_2$ adsorbée en deuxième monocouche (MC) sur Ag(111) (Figure 1 (c)) et sur Cu(111). Dans les deux cas, la molécule de deuxième MC forme un empilement parallèle avec une rotation de 45° par rapport à la molécule de dessous (première MC). Cette situation nous permet par la suite d'évaluer l'influence de substrat sur les propriétés électroniques de la molécule adsorbée en première MC.

Dans le quatrième chapitre, nous nous intéressons aux mesures spectroscopiques (STS) des assemblages moléculaires de $TbPc_2$ sur les trois substrats. Les spectres de conductance différentielle dI/dV relevés (Figure 2) laissent apparaitre une importante modification des états occupés et inoccupés des orbitales moléculaires de $TbPc_2$, cette modification est due principalement au degré d'interaction de la molécule avec le substrat. En raison de sa forte stabilité sur le Cu (111), la molécule présente un gap HOMO-LUMO de 1.4 eV (spectre noir Figure 2 (a)). Tandis que sur les autres substrat nous remarquons une légère réduction du gap lorsque la molécule est déposée sur Ag(111) et une réduction importante du gap d'environ 0.3 eV (spectre bleu Figure 2 (a)) lorsqu'elle est déposée sur Au(111). A travers une étude spectroscopique approfondie de l'effet Kondo réalisée sur la molécule déposée sur les trois substrats, nous avons étudié les manifestations de l'électron excédentaire délocalisé. Sur l'Au (111), nous détectons une résonnance Kondo au niveau de Fermi sur les lobes de la molécule (pic bleu, Figure 2 (b)). Cette résonnance s'explique par la présence d'un moment de spin sur la molécule, un électron π non apparié (radical) est alors localisé sur le ligand Pc supérieur. Sur Ag (111), un transfert de charge se produit entre le substrat et la molécule et induit par conséquent un appariement des radicaux de spin sur le ligand. Cela conduit à l'absence de la résonance Kondo sur les lobes de la molécule (spectre rouge, Figure 2 (b)). Sur le Cu (111), en raison de la forte hybridation de la molécule avec le substrat, nous détectons des pic Kondo sur le centre et le ligand de la molécule (pic noir Figure 2 (b)). Par une étude comparative, nous avons mis en évidence la croissance de molécules de YPc_2 sur Au(111) afin évaluer l'impact des électrons π localisés sur le ligand Pc sur les électrons 4f de l'ion central.

Dans le même chapitre nous présentons aussi les mesures spectroscopiques effectuées sur la molécule TbPc2 adsorbée en deuxième MC sur les deux substrats Ag(111) et Cu(111). Sur l'Ag(111), nous détectons un effet Kondo sur le ligand de la molécule adsorbée en deuxième MC, ce qui est cohérent si on considère l'appariement des radicaux de spin sur le ligand de la première MC. Sur le Cu(111), aucun effet Kondo n'est détecté sur la molécule en deuxième MC, nous suggérons dans ce cas que l'interaction spin-spin moléculaire entre les deux monocouches à travers les ligands Pc est responsable de l'appariement des radicaux de spin sur le ligand de la deuxième MC.

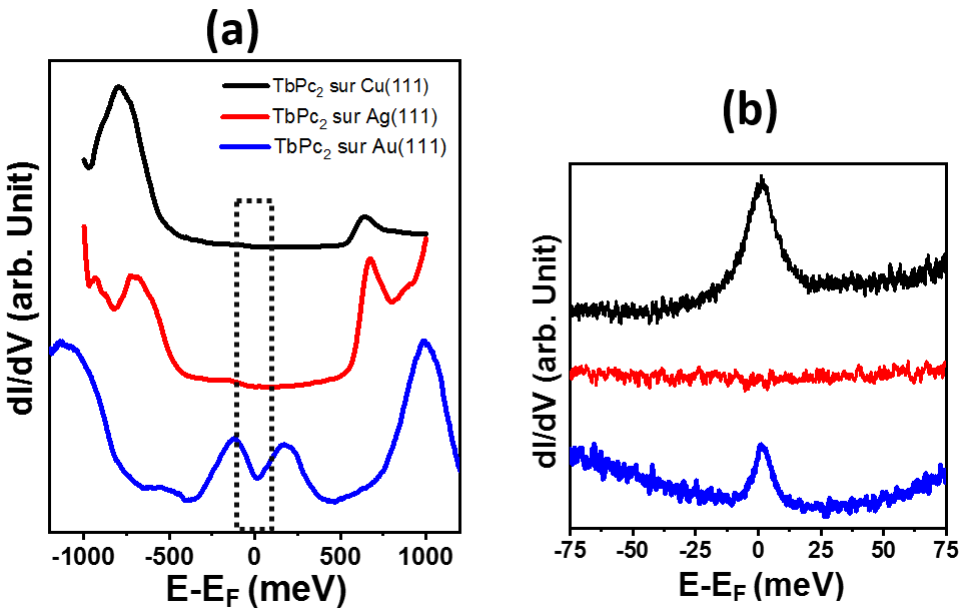

Figure 2 : (a) Spectres dI/dV enregistrées sur le ligand de $TbPc_2$ déposée sur Cu(111) (noir), sur Ag(111) (rouge) et sur Au(111) (bleu). (b) rectangle marqué sur (a) spectres dI/dV montrant deux résonnances Kondo (noir et bleu) sur le ligand de la molécule $TbPc_2$ déposée sur Cu(111) et Au(111), Pas de Kondo (rouge) sur le ligand de la molécule déposée sur Ag(111).

Nous avons vu que quand les molécules de $TbPc_2$ sont évaporées sur l'une des surfaces Au (111) et Ag (111), elles forment spontanément des domaines moléculaires. Une étude spectroscopique a révélé que la conductance dI/dV enregistrée sur la molécule (ligand et centre) varie selon la nature de substrat ainsi la nature des interactions mutuelles existantes dans le domaine moléculaire. Dans le but de former un système *Host-guest* et ainsi de confiner une molécule individuelle ou des molécules rassemblées (dimère, trimère ou tétramère) dans les nanopores du réseau, dans le cinquième chapitre nous avons fabriqué des réseaux métal-organiques $Co(NC\text{-}Ph_n\text{-}CN)_3$ ayant des pores hexagonaux avec une périodicité ajustable. Ces pores seront exploités pour localiser les molécules $TbPc_2$ et mesurer leurs propriétés électroniques et magnétiques. La localisation de la molécule *guest* $TbPc_2$ dans les nanopores du réseau *Host* $Co(NC\text{-}Ph_n\text{-}CN)_3$ semble être complexe à la température 77 K. En effet, le dépôt de $TbPc_2$ entraine une rupture du réseau de coordination, ceci est dû à la diffusion des îlots moléculaires de $TbPc_2$ sur la surface. L'architecture globale du réseau devient désordonnée à cause de l'instabilité de l'interaction de coordination entre le métal Co et les précurseurs organiques $NC\text{-}Ph_n\text{-}CN$.

Introduction

In the last ten years, the physics of the Kondo effect has recaptured interest by the development of nanotechnologies. Studies on nanoscale objects such as quantum dots [1, 2], nanotubes of carbon [3], nanoparticles of intermetallic compounds or the single molecule [4]. For some time, the single magnetic molecules (SMMs) adsorbed on metallic surfaces offer a field of exploration of the Kondo effect in low dimensions.

With the rise of molecular electronics, a discipline for which the single molecule is the basic building block of electronic components, extensive research has turned to studying the Kondo effect in adsorbed molecules on metallic surfaces. The growing interest in molecules comes from the ease of implementation as well as the robustness of the systems offered by chemical engineering. A class of interesting molecules is the class of lanthanide-based molecules where the Ln ion is sandwiched between two macrocycles of phthalocyanine (Pc).

Studies conducted in recent years on these systems have shown the difficulty of understanding the Kondo effect. In particular, intramolecular interactions between 4f-states and π-states as well as interactions with the metallic substrate are still poorly understood today [5, 6, 7]. In addition, probing 4f electrons with a local probe remains a challenge because of their spatial extension which is very localized around the nucleus and deep energy levels.

The first demonstration of a Kondo resonance by tunnel spectroscopy of these lanthanide double decker molecules was carried out in 2011 on $TbPc_2$ adsorbed on Au(111) by Komeda et al. [7]. However, in this experiment, the origin of the Kondo effect does not lie in the interaction between the conduction electrons of the substrate and the spin carried by terbium, but a spin resulting from an unpaired π-electron localized in the ligand (Pc) of the molecule. The 4f-states were later probed by tunnel spectroscopy in both the $NdPc_2$ / Cu(100) [5] and $DyPc_2$ / Cu(111) [6] systems due to the strong interaction between the ligand and the surface.

Studies have been carried out using transport measurements in molecular transistors [8,9] or in planar geometries where the double-decker molecules are adsorbed on metallic surfaces and probed by tunnel spectroscopy [10]. The combination of these molecules on such surfaces forms self-assemblies with specific geometries. Molecular blocks are based on lateral

intermolecular interactions allowing the appearance or disappearance of delocalized π- radicals [11].

Here, we are interested in the molecule/metal interface likely to present an original Kondo effect. The interface is composed of an MPc_2 molecule (M = Tb, Y) in contact with different metallic substrates Au(111), Ag(111) and Cu(111). The non-magnetic YPc_2 molecule (empty 4f-states) composed of a central Yttrium ion makes it possible to compare $TbPc_2$ and to account the role of 4f-electrons in the electronic and magnetic molecular properties. In this thesis, the main objectives have been the following: Study the structure of molecular arrangements, study the electronic properties of the molecule on different substrates and highlight the physical origin of the Kondo effect.

Accordingly, this manuscript is divided into five chapters.

The **first chapter** contains two parts, the first one is an introduction to molecular magnetism where we will present the theoretical elements that allow the understanding of the magnetic centers behavior (lanthanides) in its molecular environment, whereas the second part, which is an introduction of the Kondo effect, is dedicated to the observation of the Kondo effect on a noble metal and its modelling by a Fano resonance. Then, some published experimental findings of the Kondo effect in organic or metal-organic molecules will be presented.

The **second chapter** is a presentation of the experimental methods mainly dedicated to the preparation and characterization of ultra-high vacuum samples. This chapter describes sample preparation techniques including molecular and metal evaporation techniques. The characterization of the samples is carried out at very low temperature by microscopy and tunneling spectroscopy (STM / STS) whose operating principle is presented.

The **third chapter** is dedicated to the structural study of $TbPc_2$ molecules deposited on Au(111), Ag(111) and Cu(111) substrates as well as YPc_2 molecules deposited on Au(111). In this chapter, we will show that the molecules deposited on Au(111) or Ag(111) adopt two configurations (Phases I and II), characterized by the absence or the presence of lateral interactions between lobes of adjacent ligands. On Cu(111), the molecules are not as mobile as on the other substrates and the molecules rather adsorb side by side.

In the **fourth chapter**, we are interested in the study of $TbPc_2$ molecular assemblies in very low temperature tunnel spectroscopy. We present measurements of the differential conductance associated with different molecular configurations and on different substrates. In

particular, a study of the Kondo effect by tunnel spectroscopy is achieved on the first monolayer as well as on the second monolayer. We will show that the appearance or disappearance of this effect is mainly due to the degree of interaction with the substrate or the lateral interactions of the molecule with its neighborhood.

In the **fifth chapter**, we have manufactured metal-organic coordination networks Co $(NC\text{-}Ph_n\text{-}CN)_3$ with hexagonal pores with adjustable periodicity. These pores will be exploited to locate and confine the SMM molecules of $TbPc_2$. We will show by topographic STM measurements that the co-deposition of $TbPc_2$ brakes the coordination network, making the localization of these molecules in the nanopores of the network impossible.

REFERENCES

[1] M. Pustilnik, Y. Avishai and K. Kikoin. Quantum Dots with Even Number of Electrons. Kondo Effect in a Finite Magnetic Field. *Physical Review Letters* 84, 1756. (2000)

[2] S. Sasaki, S. De Franceschi and J. M. Elzerman. Kondo Effect in an Integer-Spin Quantum Dot. *Nature* 405, 764. (2000)

[3] J. Nygård, D. H. Cobden and P. E. Lindelof. Kondo Physics in Carbon Nanotubes. *Nature* 408, 342. (2000)

[4] G. D. Scott and D. Natelson. Kondo Resonances in Molecular Devices. *ACS Nano* 4, 3560. (2010)

[5] S. Fahrendorf, N. Atodiresei, C. Besson, V. Caciuc, F. Matthes, S. Blügel, P. Kögerler, D. E. Bürgler and C. M. Schneider. Accessing 4f-States in Single-Molecule Spintronics. *Nature Communications* 4, 2425. (2013)

[6] B. Warner, F. El Hallak, P. Seibt, H. P. ser, V. Caciuc, M. Waters, A. J. Fisher, S. B. Fischer, J. van Slageren, N. Atodiresei and C. F. Hirjibehedin. Sub-Molecular Modulation of a 4f Driven Kondo Resonance by Surface-Induced Asymmetry. *Nature Communications* 7, 12785. (2016)

[7] T. Komeda, H. Isshiki, J. Liu, Y.-F. Zhang, N. Lorente, K. Katoh, B. K. Breedlove and M. Yamashita. Observation and Electric Current Control of a Local Spin in a Single-Molecule Magnet. *Nature Communications* 2, 217. (2011)

[8] L. Bogani and W. Wernsdorfer. Molecular spintronics using single-molecule magnets, *Journal of Nanotechnology*, 7, 186. (2008)

[9] W. Wernsdorfer. Molecular Nanomagnets: Towards molecular spintronics. *International Journal of Nanotechnology* 7, 497. (2010)

[10] L. Vitali, S. Fabris, A. Mosca Conte, S. Brink, M. Ruben, S. Baroni and K. Kern. Electronic Structure of Surface Supported Bis(phthalocyonato) Terbium (III) Single Molecular Magnets. *Nano Letters* 8, 4471. (2008)

[11] A. Amokrane, S. Klyatskaya, M. Boero, M. Ruben and J-P. Bucher. The Role of π-Radicals in the Spin Connectivity of Clusters and Networks of Tb Double-Decker Single Molecule Magnets. *ACS Nano* 11, 10750. (2017)

CHAPTER 1

Theoretical overview

1.1 Introduction

In this section, we are interested in defining fundamental concepts related to the spin detection in Single Molecular Magnets (SMMs). Brief definitions of molecular magnetism and magnetism carried by lanthanide ions and the ligand field theory associated where the contribution of 4f-electrons is highlighted. In this approach, we introduce the physics necessary to understand the Kondo effect and the state of the art of the tunnel spectroscopy study of Kondo adatoms.

1.2 Molecular magnetism

In 1990, a new class of magnetic materials called molecular magnets has been discovered. Several studies have demonstrated the presence of spin on Mn_{12} molecules [1], a molecule with a high ground state [2] that shows a slow magnetic relaxation giving rise to a magnetic hysteresis [3]. The magnetism of the molecular magnet can be based on the orientation of the magnetic moments present on the single magnetic atoms, the magnetic anisotropy defines the directional dependence of the moments in the material. In the simplest case of uniaxial anisotropy, an easy axis defines the preferred magnetization axis. The two opposite directions along this axis are degenerated and the direction of the magnetization may be one or the other.

In the case of a single spin S, this can be described by an anisotropy energy $E = DS_z^2$ with $D<0$ and the direction z defined as easy axis. If the sample is prepared in a defined state m= -10, the energy DS^2 is needed to "climb up the ladder" of states to reach m = + 10. This energy called anisotropy barrier which can define the relaxation time τ of the system by the relation $\tau = \tau_0 \exp(\frac{DS^2}{k_B T})$. For systems of multiple spins, the total anisotropy energy scales vary with the

number of magnetic atoms. Anisotropy can be caused by the structure of spin lattice, the coupling of several spins inside a molecule or even the interaction with a non-magnetic substrate in the case of an individual atom.

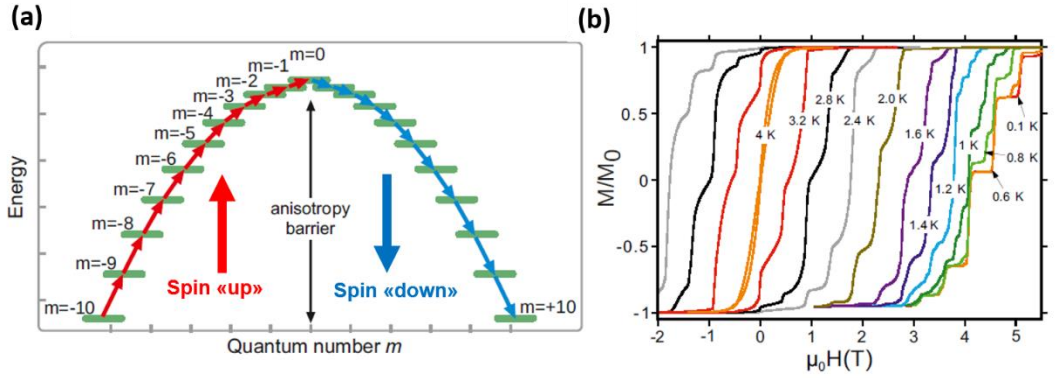

Fig. 1.1: (a) The potential energy versus the magnetization direction for the Mn_{12} SMM with an S=10 ground state experiencing axial zero-field (D), image reproduced from [4]. (b) Hysteresis loops for Mn_{12} SMM at different temperatures. At lower temperatures the loops display steps and plateaus due to the quantum tunneling of magnetization, an effect in which the system tunnels through the anisotropy barrier even at energies below DS_z^2 . (Image adapted from [4])

Molecular magnets describe a class of spin-carrying molecules with ferromagnetic properties such as hysteresis (Figure 1.1 (b)) or a slow relaxation time of magnetization. The total molecular spin is often composed of several atomic spins found inside the molecule. Molecular magnets usually have a core-shell structure: the core consisting of spin-bearing metallic atoms and an organic shell protecting the core in its environment against charge transfer and chemical reactions.

The most well-known molecule magnet is Mn_{12}. This molecule consists of a core of 12 Manganese atoms carrying the spin. Other magnet molecules consisting of the Mn atom have been identified such as Mn_6 [5] and Mn_{14} [6] or the Fe atom such as Fe_8 [7]. In addition, there are hetero-metallic molecular magnets such as Cr_7Ni, where the individual spins are antiferromagnetically coupled. A simple form was developed in 2003 and consists of a single metal atom shielded by an organic surrounding as $TbPc_2$ [8].

Molecular magnets are nanoscale magnets, so they are good candidates for data storage. The flow of research is often directed towards increasing the height of the anisotropy energy barrier to achieve a longer relaxation time at usable temperatures. Magnetic relaxation in SMMs occurs not only through the thermal process but can also be induced by the tunneling of magnetization [9].

Various studies carried out on SMMs bring into play the molecular nature and the corresponding magnetic properties. These studies conducted to highlight the self-assembly of SMMs molecules on crystallographic substrates, so that quantum behavior is observed by very large varieties of methods. Although the magnetism of a magnet does not depend on neighboring spins, it can also be influenced by its environment: either by the effect of charge transfer or by modification of the intramolecular coupling (by chemical reactions modifying the structure).

1.3 The Lanthanides

1.3.1 Generalities

Lanthanides are chemical elements that make up the f block of the periodic table between the lanthanum and the lutecium. Their discovery began in 1787 in a Swedish town named Ytterby in the form of a black mineral, the gadolinite. The first obtained lanthanide was the yttrium, isolated in its oxide form by Pr. Gadolin from this mineral [10]. In 1803, Berzelius and Klaproth isolated the cerium from another mineral, the cerite. Subsequently, Henry Moseley proved that there were fourteen elements between the lanthanum and the hafnium through the use of X-rays. They were classified as "rare earths" because they are obtained from rare minerals although they are in fact very abundant in the earth's crust (Table 1.1).

The lanthanides (Ln) are also defined by the progressive filling of the underlayer 4f conferring them similar electronic configurations varying from [Xe]$5d^1$ $6s^2$ to [Xe]$4f^{14}5d^1$ $6s^2$ (Table 1.1). After the lanthanum, the addition of protons in the nucleus induces the contraction of the 4f orbitals becoming more stable than the 5d orbitals and the 4f sub-layers are thus filled before the 5d under-layers [10]. The increase in the nuclear charge will act more on the peripheral electrons causing the decrease of the atomic radius when the atomic number increases. This phenomenon is called the lanthadinic contraction. Lanthanides have the ability to lose three electrons to form a Ln^{3+} ion that largely dominates the lanthanide complexing chemistry [11]. Ln^{3+} ions have an electronic configuration [Xe]f^{n+1}.

	Chemical Symbol	Atomic Number (Z)	Electron configuration (Ln)	Electron configuration (Ln^{3+})
Lanthane	La	57	$[Xe]5d^16s^2$	$[Xe]6f^0$
Cerium	Ce	58	$[Xe]6f^15d^16s^2$	$[Xe]6f^1$
Praséodyme	Pr	59	$[Xe]6f^36s^2$	$[Xe]6f^2$
Néodyme	Nd	60	$[Xe]6f^46s^2$	$[Xe]6f^3$
Prométhéum	Pm	61	$[Xe]6f^56s^2$	$[Xe]6f^4$
Samarium	Sm	62	$[Xe]6f^66s^2$	$[Xe]6f^5$
Europium	Eu	63	$[Xe]6f^76s^2$	$[Xe]6f^6$
Gadolinium	Gd	64	$[Xe]6f^75d^16s^2$	$[Xe]6f^7$
Terbium	Tb	65	$[Xe]6f^96s^2$	$[Xe]6f^8$
Dysprosium	Dy	66	$[Xe]6f^{10}6s^2$	$[Xe]6f^9$
Holmium	Ho	67	$[Xe]6f^{11}6s^2$	$[Xe]6f^{10}$
Erbium	Er	68	$[Xe]6f^{12}6s^2$	$[Xe]6f^{11}$
Thulium	Tm	69	$[Xe]6f^{13}6s^2$	$[Xe]6f^{12}$
Ytterbium	Yb	70	$[Xe]6f^{14}6s^2$	$[Xe]6f^{13}$
Lutecium	Lu	71	$[Xe]6f^{14}5d^16s^2$	$[Xe]6f^{14}$

Tab. 1.1: Electron configuration of lanthanides (Ln) and lanthanide ions (Ln^{3+}).

1.3.2 Magnetism of Lanthanides

The description of the electronic structure of the lanthanide atoms is essential for understanding the magnetism in the lanthanide complexes. The 4f-orbitals show a strong angular dependence and lie deeply buried in core electron density as shown in Figure 1.2 (a) [12,13]. This figure indicates that the 4f-electrons are well shielded by the 5s and 5p states from their surroundings and their angular variation is obvious in the magnetic quantum number m_l. Therefore, this leads to a strong spin-orbit interaction. To better describe the electronic structure of lanthanide ions, we refer to the Russel-Saunders model [14] describing the L - S coupling noted by the multiplet ${}^{2S+1}L_J$ ($|L-S| \leq J \leq |L+S|$), as shown in the figure, where the total momentum J is calculated from the total orbital momentum $L = \sum_i l_i$ and the total spin momentum $S = \sum_i s_i$. The energy of multiplet levels is defined by the following relation:

$$E\left({}^{2S+1}L_J\right) = \left(\frac{\lambda}{2}\right)[J(J+1) - L(L+1) - S(S+1)] \qquad (1.1)$$

Where λ is the spin-orbit coupling. The lower multiplet J (L-S) is called the ground state mutiplet level and it is well separated from the excited ones because of the large spin-orbit coupling energies except for the two ions Eu^{3+} and Sm^{3+}. For describing the magnetic properties of the lanthanide ions, it may be sufficient to consider only the ground level characterized by the angular momentum quantum number J [15].

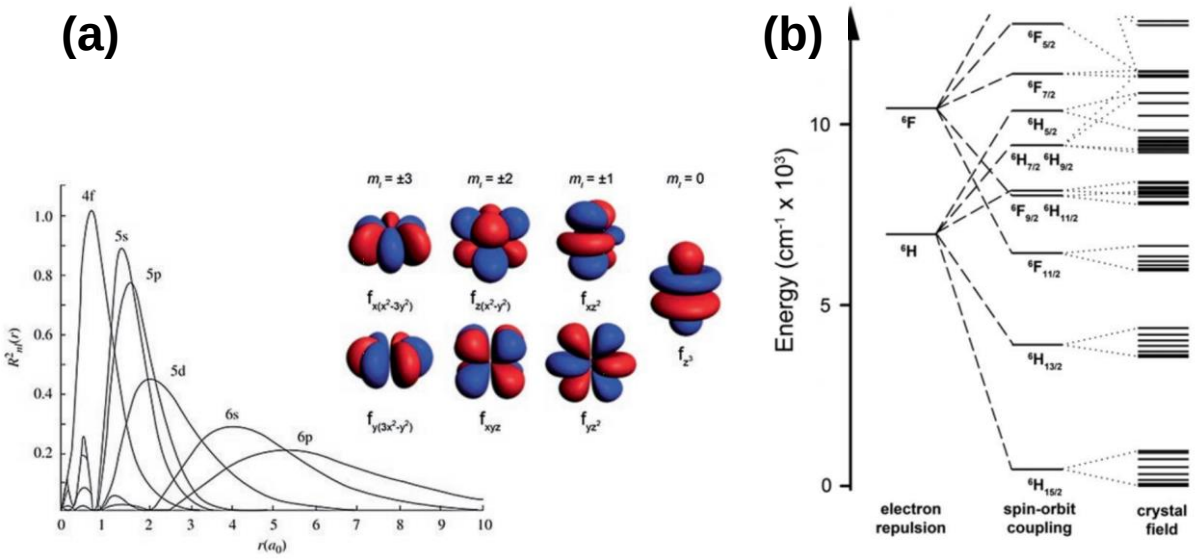

Fig. 1.2: (a) Radial distribution functions of 4f, 5s, 5p, 5d, 6s and 6p electrons for cerium [12]. *Inset* The 4f orbitals from highest magnitude to lowest magnitude m_l [12]. (b) level scheme of the electronic structures of the Dy^{3+} ion obtained after the electronic repulsion, spin-orbit coupling and crystal field [13]

1.4 Ligand field theory

Ligand field theory is a formalism that takes into account the interactions and the coordinations contributing overall cohesion of elements in a metal-organic complex [17]. This theory has a prominent role in creating a highly anisotropic ground state. The ligand field is the electrostatic field experienced by the unpaired electrons of a given magnetic ion from the surrounding coordinated atoms, as shown in the Figure 1.3. Here, a given ligand field is able to orient the electronic charge cloud to an energetically favorable direction and decides the type of anisotropy based on the shape of the lanthanide ions. For example, in Figure 1.3 (a) the cubic crystal field makes the lanthanide ions with the prolate electron distribution the easy-axis configuration, because the planar distribution of the negative crystal-field charges minimizes the repulsive contacts to f-electron charge clouds. Inversely, the anisotropy is in plane for the lanthanide ions with the prolate electron distribution in elongated cubic crystal-field because of the large repulsive contacts between coordinate atoms and f-electron charge clouds. In contrast, the opposite is true for the lanthanide ion with oblate electron distribution, such as Dy(III) and Tb(III).

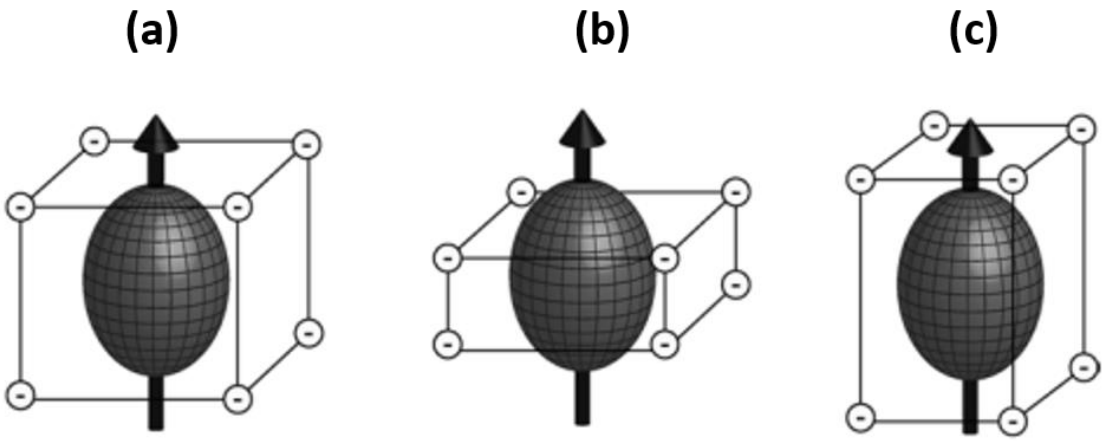

Fig. 1.3: The anisotropy of the 4f-shell electron distribution for tripositive lanthanides associated with the point-charge model in cubic crystal field (a) and tetragonal crystal fields (b and c).

In the phtalocyanine double-decker lanthanides complexes (Figure 1.4) the interactions between the f-orbital electron density and the crystal field (sandwich-type) creates a bistable ground state with large magnetic moment (m_J) for the lanthanide ions with oblate electron density like Dy(III) and Tb(III), because the small contact between charge cloud and ligands.

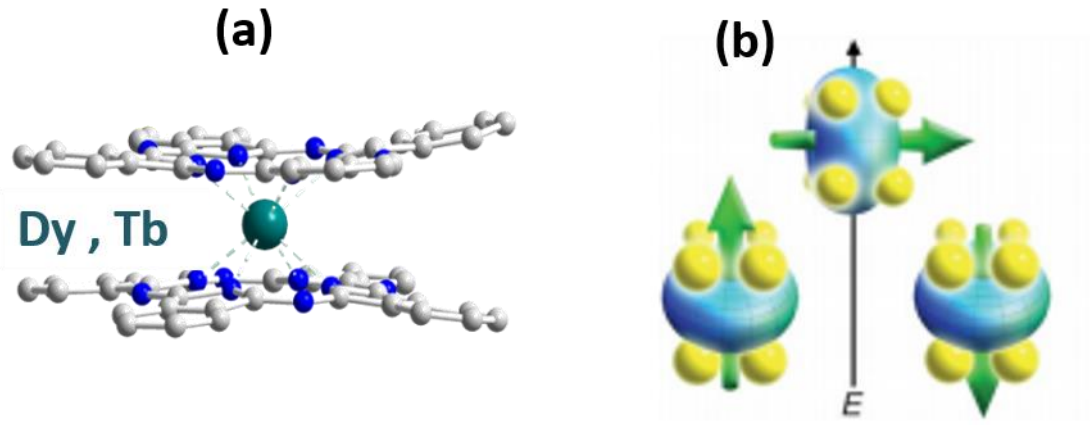

Fig. 1.4: (a) Sandwich-type crystal field for $LnPc_2$ single-molecule magnet design. (b) Depictions of low- and high-energy configurations of the f-orbital electron density with respect to the crystal field environment for a 4f ion of oblate electron density. The green arrow represents the orientation of the spin angular momentum coupled to the orbital moment. reproduced from [17].

In order to describe the fundamental magnetic behavior of lanthanide ions in ligand field, the crystal field calculation is based on an effective crystal field Hamiltonian [17-19]:

$$H_{LF}(J) = \sum_{k=2,4,6} \sum_{q=-k}^{k} B_k^q O_k^q = \sum_{k=2,4,6} \sum_{q=-k}^{k} a_k A_k^q \langle r^k \rangle O_k^q \qquad (1.2)$$

where q and k are the operator orders, the first one must be an even integer because of the symmetry inversion of the crystal field potential and the second varies between −k and +k. Here, $a_{2,4,6}$ are the Stevens equivalent operators for α, β and γ respectively. A_k^q and and B_k^q called ligand field parameters to be determined experimentally. O_k^q represents the Stevens main operators which are combination of the components of the J operator.

1.5 $TbPc_2$ Single molecule magnet (SMM)

The first exploration of the $LnPc_2$ family of organometallic complexes with a "Double-decker" structure was done by Ishikawa et al. [20], where the terbium (Tb^{3+}) species exhibits a high effective barrier, U_{eff} = 440 cm^{-1}. This discovery has also prompted researchers for the conception of lanthanide-based SMMs such as polyxymetalalates (LnPOM) [21] and lanthanide double-decker [22] complexes. As shown in Figure 1.5, both phthalocyanine ligands demonstrate a high local symmetry with the coplanar coordination to the atom [23]. In general, the two planes are leading to the typical square antiprismatic (SAP) geometry producing a large magnetic anisotropy of the central lanthanide ion.

The $TbPc_2$ molecule is characterized by a large unquenched magnetic moment and a high magnetic anisotropy carried by the Tb metal. At very low temperatures, the spin relaxation time in the molecule becomes large leading to a hysteresis loop. The magnetic character in the molecule is mainly due to the partial filling of the 4f orbitals ($[Xe]4f^8 6s^2$) of the Tb^{3+} ion. According to Hund's rules, leads to a total angular momentum is J = 6, with equal contribution, from the orbital magnetic moment L = 3, and magnetic moments of spin S = 3.

The Pc ligands have a formal charge of (2-) with a closed shell π-electronic system, this discovery has been reported by Ishikawa et al. [20]. However, the oxidation of the anionic $[TbPc2]^-$ generates one π-electron delocalized over two Pc ligands which constitutes a second source of spin (S = 1/2) in the molecule. Recent work by STS Kondo has been reported on the detection of π-radical in the combination of terbium double-decker molecules on metallic substrates [24-27]. These studies have shown a difficulty in detecting the Kondo effect on these systems. In particular, intermolecular interactions between 4f-states and π-states and interactions with the metal substrate are still poorly understood today [29]. Moreover, probing 4f-states (of the central ion) by STS remains a challenge until today for researchers.

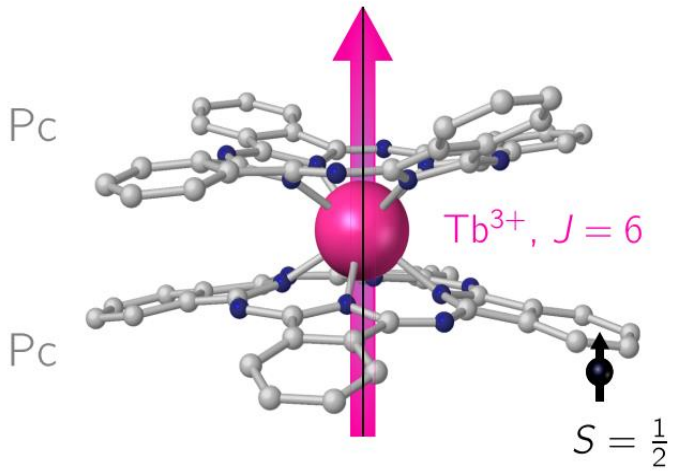

Fig. 1.5: Single molecule magnet $TbPc_2$, shows the spin (J=6) of the terbium central ion (Tb^{3+}) and the spin (S=1/2) of the Pc ligand by the pink and black arrows respectively. (taken from [29]).

1.6 Kondo effect

The Kondo effect is a very large subject, that is very difficult to treat theoretically. Here we give a summary of its historical developments as well as commonly accepted ideas by solid-state quantum physicists. This succinct presentation is intended to give an idea of what the Kondo effect is and to set the context in which we set ourselves to carry out the experiments on the Kondo effect induced by a single magnetic adatom.

1.6.1 History

In the 1930s, diluted magnetic alloys had been discovered. These alloys show an abnormal rise in electrical resistivity at low temperature (red curve, Figure 1.6 (a)). Since this anomaly has been much studied experimentally and theoretically by Friedel, Yosida and J. Kondo [31-33], their investigations are still very active until today. The Kondo model predicts the minimum of the finite temperature resistance as well as a divergence of the resistivity as the temperature tends to zero. This divergence is known by the name "Kondo problem". This has been confirmed by several articles and still persists today. In 1965, Abrikosov and Suhl establish the existence of a resonance in the amplitude of diffusion of an electron by a magnetic atomic impurity, called Abrikosov-Suhl resonance [34-36]. There is still some confusion between ASR and the Kondo resonance, where ASR is the resonant diffusion of conduction electrons by the impurity, whereas the Kondo resonance is the density of the impurity states. These are two complementary theoretical approaches to the Kondo state.

At the end of the 1960s, Anderson [37] had solved the problem of divergence, and Schrieffer [38] showed that the Kondo Hamiltonian is a simply special case of Anderson's. In 1974, Wilson [39] invented a resolution procedure that exists until today in the study of Kondo Systems called the Normalization Digital Group Method (NRG). This method considers that the spin of the impurity is screened by the spins of the conduction electrons of the non-magnetic metal. This screening occurred under a critical temperature is called Kondo temperature (T_K), which leads to the Kondo effect. Below this temperature, the electrons that have energy close to the Fermi level are strongly scattered by the impurity. At zero temperature, the Kondo theory predicts the formation of a singulet state, *i.e.* the spin disappearance of the spin impurity. In the same year of 1974, Nozières had shown that the case of the simplest Kondo model is a spin ½ shielded by the electrons from the Fermi liquid [40].

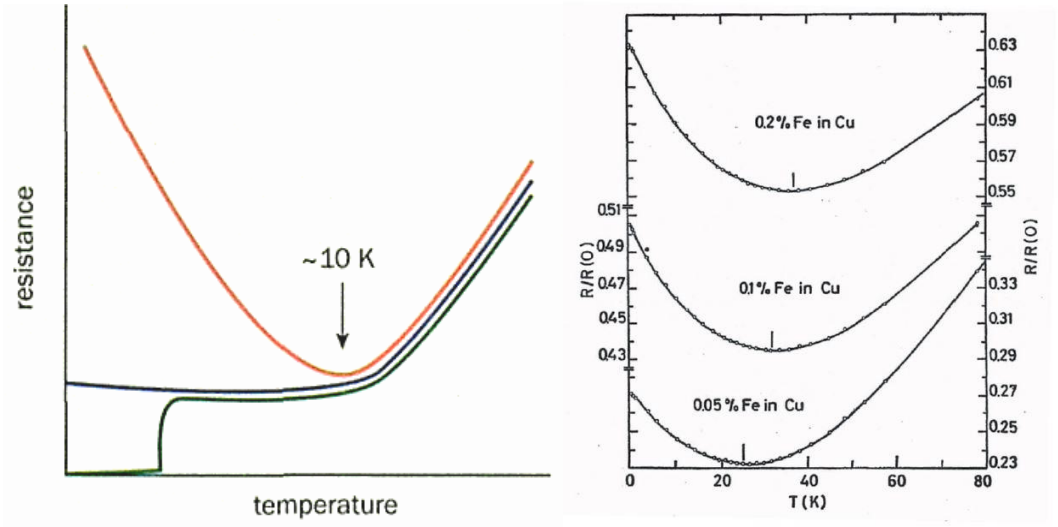

Fig. 1.6: (a) Qualitative variation of the resistivity of a metal with temperature. Normal metal (blue), superconducting metal (green), diluted magnetic alloy (red) (extract of [41]). (b) The minimum resistance as a function of temperature for the copper (Cu) crystal with different concentration of iron (Fe) impurities.

In the last 30 years, many theoretical methods have been conducted to describe the physics of a magnetic impurity in a conduction electron bath leading to exact solutions for the Kondo problem [42].

The Kondo phenomenon seems today to be a reference to the behavior of systems comprising one or more non-zero isolated spin impurities in antiferromagnetic interaction with one or more conduction electron bands. All Kondo systems are characterized by dI/dV

conductance below the critical temperature. This conductance is observed by STS at the Fermi level.

We show herein the mechanism of appearance of the Kondo resonance in the LDOS of systems in the context of the Anderson model of the impurity, represented by an isolated orbital in a doubly degenerate non-magnetic lattice which occupancy is controlled by Coulomb repulsion, while interacting with a band of conduction electrons.

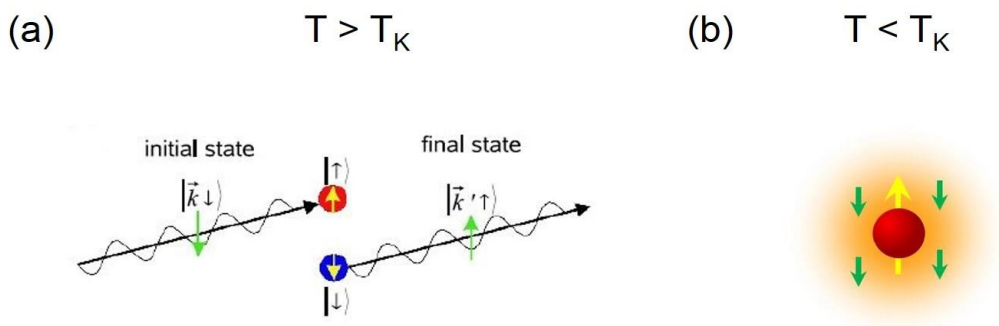

Fig. 1.7: (a) Below the Kondo temperature, host-metal conduction electrons can interact with the impurity spin, moving from an initial state $|\vec{k},\downarrow\rangle$ to a final state $|\vec{k}',\uparrow\rangle$ by a spin-flip mechanism in which the spin of the impurity and that of the electron are exchanged. (b) Kondo screening of the impurity moment by the conduction electrons of host-metal. Below the Kondo temperature T_K, the localized moment of impurity permanently falls into a many-body singlet ground state. (adapted from [43]).

The unpaired electron level, initially discrete in the isolated adatom, is enlarged by the state continuum coupling of the metal substrate to a Lorentzian of width $\Delta = \rho_0|V|^2$ (ρ_0 is the density state of the substrate and V is the hybridization matrix element corresponding to the continuum coupling). An additional electron in the orbital appears with a Coulomb repulsion energy U, as shown in the Figure 1.8, the spin exchange between the conduction electron and the impurity can be done according to two distinct mechanisms: The electron in the metal can pass into the d-orbital and allow an opposite spin electron to return to the metal (process 1) or opposite, the unpaired electron of the impurity can leave the orbital and an electron of opposite spin of the metal comes to replace it (process 2). This spin exchange process results in the appearance of a narrow peak (Kondo peak) at the Fermi level energy (Figure 1.8 (b)).

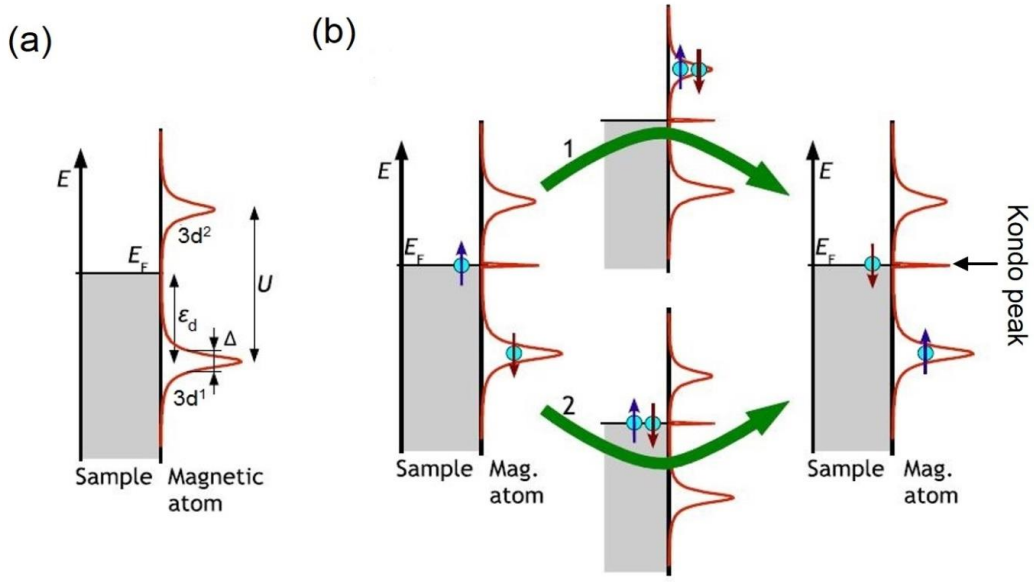

Fig. 1.8: (a) Schematic representation density of states of substrate and isolated magnetic impurity. (b) Two spin exchange mechanisms are possible: Process 1, corresponds to the transfer of an electron to the impurity resulting in a final state where the two spins are reversed; Process 2, corresponds to the transfer of an electron from the impurity to the host-metal and then to the return of an electron after spin inversion. The intermediate states are virtual states whose lifetime is of the order of 10 to 15 s. (Extracted from [45]).

The Kondo model takes into account, in the electron gas Hamiltonian, an exchange interaction term J_K between the impurity spin (Spin ½) and the electron gas spins. We recall here, in order to illustrate important quantities, the initial Hamiltonian of Kondo, which models the interaction between the spin $\vec{S}$ of the impurity and the electron band of energies ε_k:

$$H_K = \sum_{k,\sigma} \varepsilon_k a^{\dagger}_{k\sigma} + J_K \vec{s}_0 \vec{S} \qquad (1.3)$$

The first term gives the energy of free electrons in the metallic network, where the operators of creation and annihilation of an electron in the spin state σ appear, wave vector k and energy ε_k. The second term is the Kondo interaction energy, where the local electronic spin density $\vec{s}_0$ is antiferromagnetically coupled to the spin of the impurity. In this model, the Kondo temperature is related to the density of states at Fermi level ρ_0 (ε_F) by the following relation:

$$T_K \propto \exp\left[-\frac{1}{\rho_0(\varepsilon_F) J_K}\right] \qquad (1.4)$$

The Kondo contribution appears when pushing the calculation to highlight the dependence of the resistivity of the linear alloy in n_i (concentration of impurities) and describes the scattering

of the conduction electrons of the metal by the magnetic impurity. As a result, the general transport properties of the material express as.

$$\rho(T) = \rho_0 + A.T^5 + BJ_K.\log\left(\frac{T}{C}\right) \qquad (1.5)$$

Where A, B and C are constants proper to the system.

The expression of conductance in Equ. (1.5) combines the behavior of the conductance at high and low temperature. At high temperature, the term containing T^5 dominates the overall conductivity through phonons scattering whereas the logarithmic term dominates the behavior of the system at low temperatures. This approach is not valid below the Kondo temperature T_K. Therefore, Equ. 1.5 proved valid only in the regime $T >> T_K$ [43]. Figure 1.9 shows the spectral density calculated for a d- or f-orbital in the framework of the Anderson model in which a strong Coulomb repulsion U between two electrons is a necessary condition for the appearance of a Kondo resonance [44].

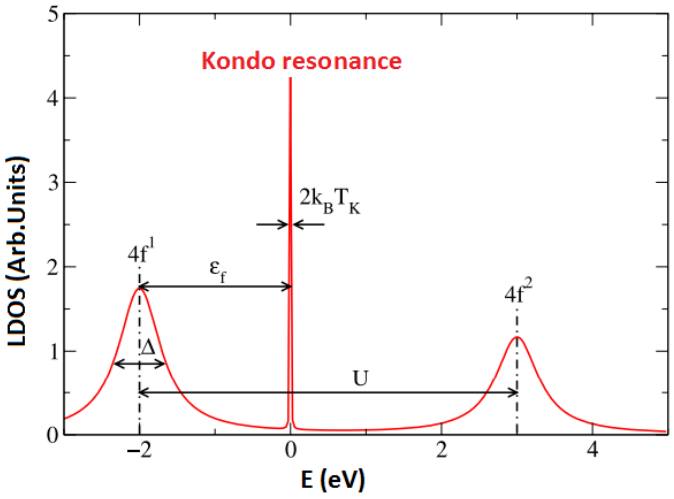

Fig. 1.9 : Simulation of LDOS of the cerium impurity. The half-width at half height is worth $k_BT_K \equiv \Gamma$. The parameters used for the calculation are ε_F = -2 eV, U = 5 eV, Δ = 0.34 eV, (Adapted from [45])

1.6.2 Kondo resonance Observation on STS spectra

Experimental observations of the Kondo effect were limited to overall measurements on a set of impurities. The invention of the STM and the progress in the detection electronics at an atomic resolution have allowed the investigation of the Kondo effect induced by a single magnetic atom adsorbed on a metallic surface. The first observations of the Kondo effect were

made in 1998 by Madavan et al. [44] on the Co/Au(111) system and by Li et al. [46] on the Ce/Ag(111) system.

Over the last decade, similar systems have been studied experimentally and theoretically by varying the nature of adatoms and substrate [44-50]. Many questions were left open, particularly the quantitative interpretation of the spectra remains difficult. An example of a spectrum measured by STS above an atom of Co on Cu(111) substrate is shown in Figure 1.10 (b). This spectrum has been fitted with a Fano resonance, which we introduce here.

Fano Resonance: This is the spectroscopic signature what appears in many physical issues where one or more discrete energy levels interact with a continuum of states. This problem has been resolved by Ugo Fano [36] in the context of optical adsorption spectroscopy in atomic physics, then summarized in 1961 using the formalism of the Green function. It is the interference between the paths leading from a basic state, either to the continuum or to the discrete levels that generates the resonance.

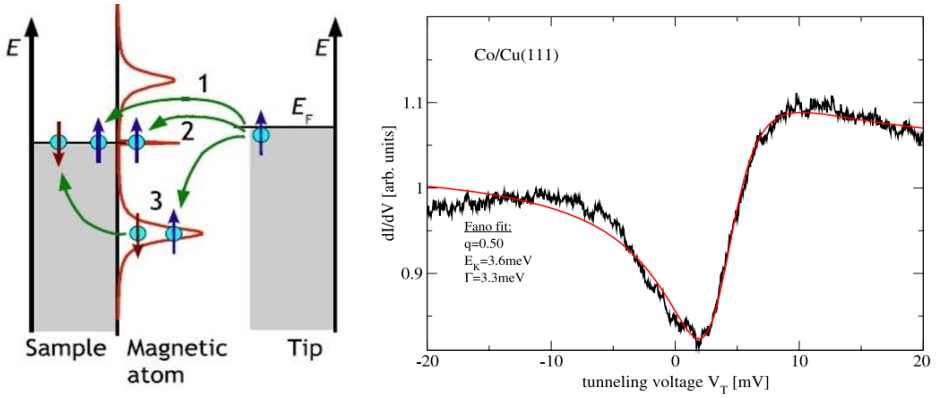

Fig. 1.10: Schematics of the tunneling paths for the electron from a probe tip to the magnetic impurity [45]: The electrons of the tip can tunnel directly into the metal continuum (path 1) or via the Kondo resonance (path 2). These two paths retain the spin and their interferences results a Fano resonance. A third path is possible, via the electron of the impurity, with spin inversion (path 3). (b) Tunnel spectrum measured above a cobalt adatom on Cu(111), fitted by Fano resonance (equation) with q = 0.5. The resonance width Γ gives a Kondo temperature of T_K= 75 ±6K [45].

The signature observed in STS on an adatom generating a Kondo resonance on a non-magnetic metal is a Fano resonance [44]. The interpretation is given in the Figure 1.10: The Kondo resonance is considered as a discrete level coupled to the continuum of the metal-host, and the electronic waves coming from the tip can take two paths towards the electron bath of the metallic substrate, either passing through the Kondo state, or directly to the continuum of

the metal. The probability of these paths is different, and their ratio determines the shape of the Fano resonance, given by the Fano parameter q.

$$q = \frac{1}{2\pi\rho_0 V}\frac{t_2}{t_1} \propto \frac{probability\ to\ pass\ via\ the\ kondo\ resonance}{probability\ to\ pass\ directly\ to\ the\ continuum} \qquad (1.6)$$

where t_1 and t_2 are the tip-substrate and tip-impurity couplings respectively (proportional to the probability of the paths 1 and 2 in the Figure 1.10 (a) and ρ_0 is the density of the quasi continuum, considered constant.

The spectral profile resulting from the interference of a single discrete level with a continuum is written as follows:

$$\rho(E) \propto \rho_0 + \frac{(q+\frac{E-E_e}{\Gamma})^2}{1+(\frac{E-E_e}{\Gamma})^2} \qquad (1.7)$$

Where Γ is the half-width of the resonance. The values of q = 0 correspond to an antiresonance (Lorentzian antiresonance) and $q \rightharpoonup \infty$ corresponds to a Lorentzian resonance. The values of the order of 1 or 2 give typical profiles, an example of which is shown on a fit of an experimental spectroscopic resonance in Figure 1.11.

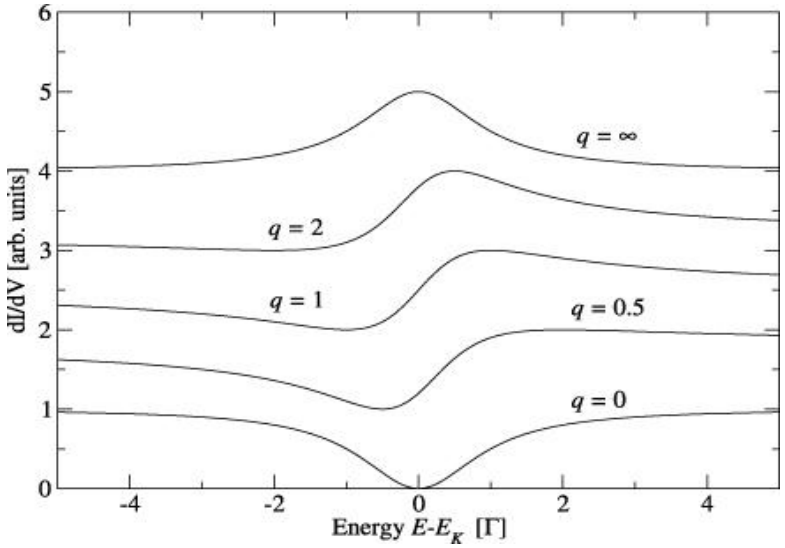

Fig. 1.11: Set of curves calculated with the normalized Fano equation for different q values [45]. At q = 0 a Lorentzian dip is detected which corresponds to mainly direct tunneling. In the limit of large q, a Lorentzian peak is formed corresponding to mainly indirect tunneling. Intermediate values of q result in an s-like curve.

1.6.3 Kondo effect on molecules

The molecule, by its electronic structure, can have a localized moment, either intrinsically as shown by their electronic structure represented by the Figure 1.12 (b), or by its transfer charge when it interacts with a surface electron donor (as in the case of TCNE [52] and $TbPc_2$ [25]). There are many examples of organometallic molecules, complexes of the form L_nM where L_n is an organic ligand and M a metal, adsorbed on metallic surfaces and have a Kondo effect [52, 53]. In this type of molecule, two cases can be distinguished: one where the moment is carried by the metallic atom M and the other where the moment is carried by the ligand L_n.

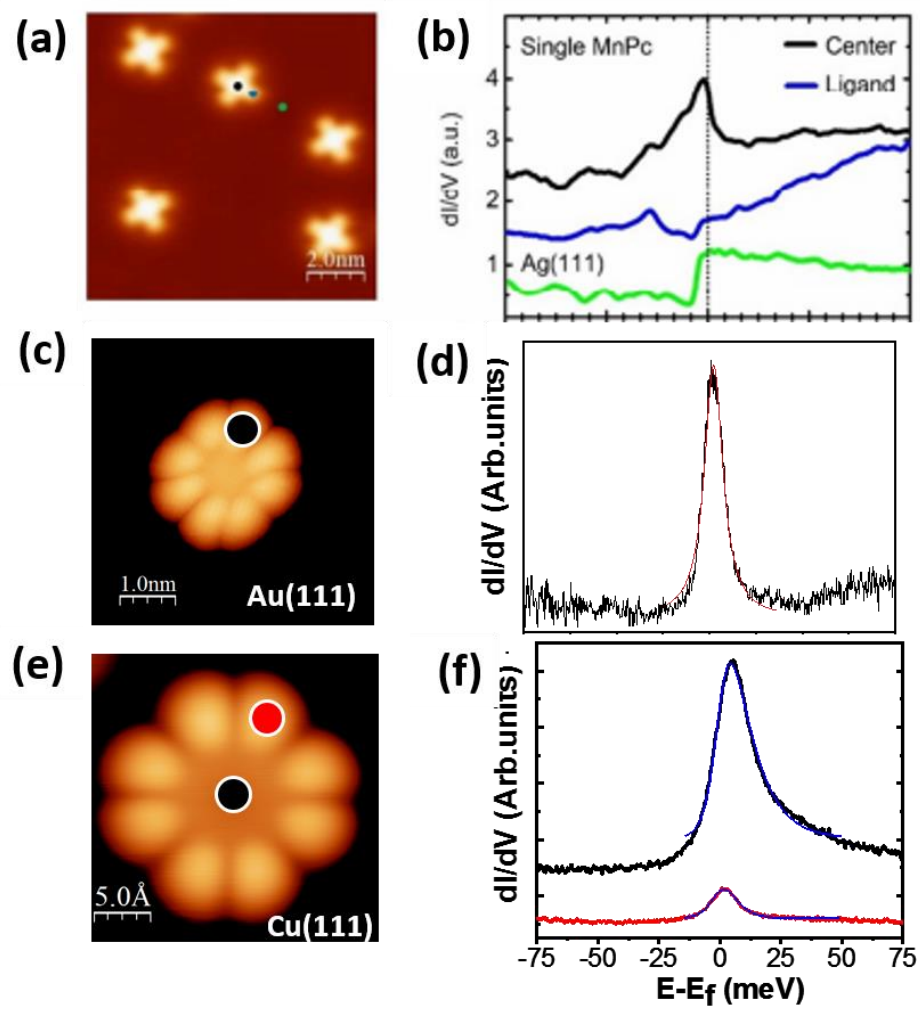

Fig. 1.12: (a) STM image of an MnPc molecule deposited on Ag(111). (b) dI/dV specta on MnPc sites shows the Kondo resonance in center (extracted from [53]). (c) STM image of an isolated $TbPc_2$ molecule deposited on Au(111). (d) Kondo peak detected on the Pc ligand. (e) STM image of an isolated $TbPc_2$ molecule deposited on Cu(111). (f) Kondo peaks acquired above the ligand (red) and center (black) of the molecule.

The STM allows the detection of the local state density and thus to know if the Kondo resonance is observed on the metallic atom, on the organic ligand or in both (metal and ligand). For example, in the case of the MnPc on Ag(111) [53], the moment is carried by the Mn atom (Figure 1.12 (a) and (b)). In the case where the molecule is inserted in the molecular network, it preserves the same Kondo properties. Another example is the $TbPc_2$ / Au(111) system where the moment is carried by the molecular orbital of the Pc ligand (Figure 1.12 (c) and (d)). When the $TbPc_2$ molecule is deposited on Cu(111), the magnetic moment is carried by the 4f-electron and the π- radical leading to the Kondo effect detection as shown in the Figure 1.12 (e) and (f).

Recent work has been carried out to show the presence of the Kondo effect on purely organic compounds (without transition metal ion or rare earth ion in the molecule). This effect could be observed in the carbon structures such as carbon nanotubes [54] and the C_{60} molecules or the TCNE molecules [52]. As shown in the Figure 1.13, an STM / STS study was carried on that TCNE molecule deposited on Cu(111) showing the Kondo peaks localization.

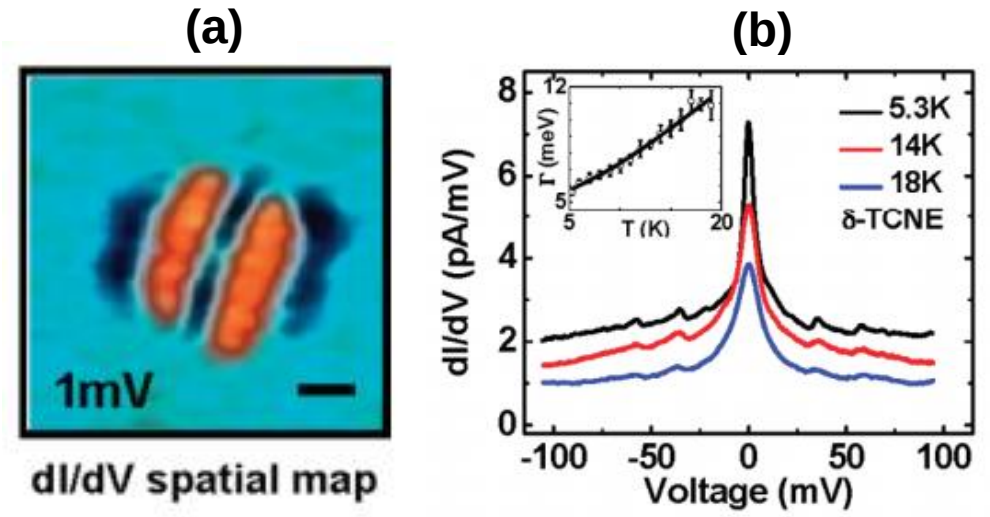

Fig. 1.13: (a) dI/dV Mapping of the density of state near Fermi level for a TCNE molecule showing the localization of Kondo resonance. (b) dI/dV spectroscopy near Fermi level on a TCNE molecule deposited on Cu(111) showing Kondo resonance at different temperatures (5.3 K, 14 K and 18 K). (Extracted from [52])

1.6.4 Temperature & Magnetic field dependence of Kondo resonance

The measurement of Kondo temperature depends explicitly on two important factors: the temperature and the applied magnetic field. At zero temperature, the spin of the impurity is completely screened by the conduction electrons which corresponds to a quasi-particle, so we have a non-magnetic singlet fundamental state. When we increase the temperature to near the

Kondo temperature, the spin of the impurity appear at the Fermi level and the Kondo state stays in its excited state. Figure 1.14 (b) shows an example illustrating the influence of temperature on the width and height of the Kondo Peak. However, Zhang. Y-H et al. [55] have examined the change in width and height of the Kondo peak measured on the organic radical molecule ($C_{28}H_{25}O_2N_4$) with a nitronyl-nitroxide deposited on Au(111). When the temperature becomes higher than the Kondo temperature, the spin of the impurity is no longer screened, and we lose the quasi-particle nature characteristic of the Kondo effect

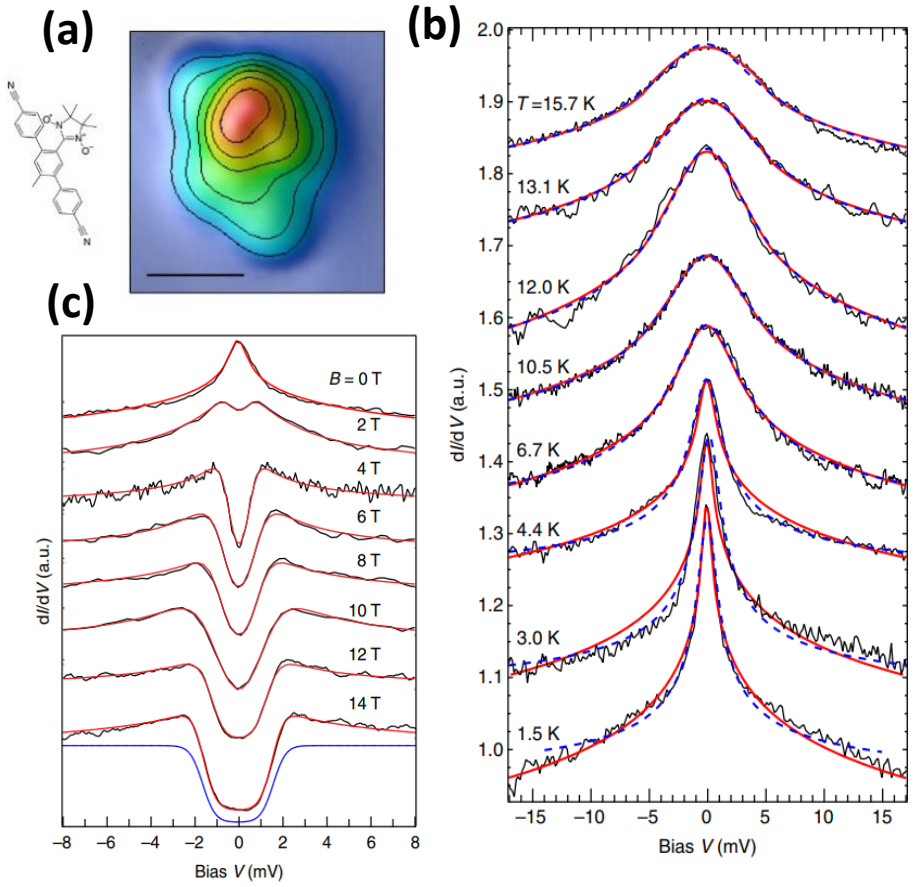

Fig. 1.14: (a) Chemical structure of the studied organic radical molecule ($C_{28}H_{25}O_2N_4$) with a nitronyl-nitroxide side group deposited on Au(111). (b) Temperature dependence of the peaks measured in the radical side group of the molecule of 1.5–15.7K. (b) Magnetic field dependence of the peaks taken on the radical side group of the molecule. (Adapted from [55])

In this thesis, we fit the Kondo resonances by a Fano function. The width of Kondo resonance depends on the temperature of measurement, given by the following relation [56].

$$\Gamma(T) = \sqrt{(3.5K_BT)^2 + (\sqrt{6}eV_{rms})^2 + 2(k_BT_K)^2} \qquad (1.8)$$

In the case where an external magnetic field is applied, two new peaks show up and replace the initial Kondo peak. Indeed, the Kondo resonance splits into two peaks with symmetric steps, as soon as, the Zeeman energy exceeds the thermal energy (Figure 1.14 (c)), that is, $Bg\mu_B < k_BT$ (μ_B is the Bohr magneton and g is the Landé factor of free electron) [51]. These two steps in the differential conductance are due to the inelastic spin-flip excitation. The difference between the peaks due to the coupling of the localized spin with the conduction electrons and their polarization by the magnetic field and the effective Landé factor [55].

REFERENCES

[1] M. Tamura, Y. Nakazawa, D. Shiomi, and K. Nozawa. Bulk ferromagnetism in the beta-phase crystal of the p-nitrophenyl nitronyl nitroxide radical. *Chemical Physics Letters*, 186(4), 401-404. (1991)

[2] A. Caneschi, D. Gatteschi, R. Sessoli, A. Barra, L. Brunel, and M. Guillot. Alternating Current Susceptibility, High Field Magnetization, and Millimeter Band EPR Evidence for a Ground S = 10 State in $[Mn_{12}O_{12}(CH_3COO)_{16}(H_2O)_4]$ $2CH_3COOH_4H_2O$. *Journal of the American Chemical Society*, 113(15):5873-5874. (1991)

[3] R. Sessoli, D. Gatteschi, A. Caneschi, and M. Novak. Magnetic bistability in a metal-ion cluster. *Nature* 365, 141. (1993)

[4] W. Wernsdorfer, M. Murugesu, and G. Christou. Resonant Tunneling in Truly Axial Symmetry Mn12 Single-Molecule Magnets: Sharp Crossover between Thermally Assisted and Pure Quantum Tunneling. *Physical Review Letters* 96, 3-6. (2006)

[5] C. Milios, A. Vinslava, W. Wernsdorfer, S. Moggach, S. Parsons, S. Perlepes, G. Christou, and E. Brechin. A record anisotropy barrier for a single-molecule magnet. *Journal of the American Chemical Society* 129(10), 2754. (2007)

[6] A. Tasiopoulos, A. Vinslava, W. Wernsdorfer, K. Abboud, and G. Christou. Giant Single-Molecule Magnets: A Mn_{84} Torus and Its Supramolecular Nanotubes. *Angewandte Chemie*, 116(16), 2169. (2004)

[7] A. Barra, P. Debrunner, D. Gatteschi, Ch. Schulz, and R. Sessoli. Superparamagnetic-like behavior in an octanuclear iron cluster. *Europhysics Letters* 35(2), 133. (1996)

[8] N. Ishikawa, M. Sugita, T. Ishikawa, S. Koshihara, and Y. Kaizu. Lanthanide double-decker complexes functioning as magnets at the single molecular level. *Journal of the American Chemical Society* 125(29), 8694. (2006)

[9] J.R. Friedman, M. Sarachik, J. Tejada, and R. Ziolo. Macroscopic measurement of resonant magnetization tunneling in high-spin molecules. *Physical Review Letters*, 76(20), 3830. (1996)

[10] Cotton, S. A. Lanthanide and actinide chemistry; Inorganic chemistry; Wiley: Chichester, England ; Hoboken, NJ, 2006.

[11] R. Joseph. Principles of Fluorescence Spectroscopy. Lakowicz, Springer 2006

[12] Rinehart J-D, Long JR. Exploiting single-ion anisotropy in the design of f-element single-molecule magnets. Chem Sci 2(11), 2078. (2011)

[13] Z-B. Goldschmidt. Atomic properties (free atom) Chap. 1. In: Gschneidner KA Jr, Eyring LR (eds) Handbook on the physics and chemistry of rare earths, vol 1. Elsevier, Amsterdam, pp 1–171. (1978)

[14] K-H-J. Buschow. Physics of magnetism and magnetic materials. Kluwer Academic/Plenum Publishers. (2003)

[15] C. Benelli, Gatteschi D. Magnetism of lanthanides in molecular materials with transition-metal ions and organic radicals. *Chemical Reviews* 102(6), 2369. (2002)

[16] J. H. van Vleck. Theory of the variations in paramagnetic anisotropy among different salts of the iron group. *Physical Review* 41(2), 208. (1932)

[17] K. W. H. Stevens. Matrix elements and operator equivalents connected with the magnetic properties of rare earth ions. *Proceedings of the Physical Society* 65(3), 209. (1952)

[18] L. Sorace, C. Benelli, and D. Gatteschi. Lanthanides in molecular magnetism: old tools in a new field. *Chemical Society reviews* 40(6), 3092. (2011)

[19] J. Tang and P. Zhang. Lanthanide Single Molecule Magnets. *Springer Berlin Heidelberg*. (2015)

[20] N. Ishikawa, M. Sugita, T. Ishikawa, S. Koshihara, and Y. Kaizu. Lanthanide Double-Decker Complexes Functioning as Magnets at the Single-Molecular Level. *Journal of the American Chemical Society* 125, 8694. (2003)

[21] M. A. Aldamen, J. M. Clemente-Juan, E. Coronado, C. Marti-casraldo and A. Gaita-Arino. Mononuclear lanthanide single-molecule magnets based polyoxometalates. *Journal American Chemical Society* 125 (29), 8694. (2008).

[22] S. D. Jiang, B.W. Wang, G. Su. An organometallic single-ion magnet. *Journal American Chemical Society* 133(13), 4730. (2011).

[23] A. Dolbecq, E. Dumas, C.R. Mayer and P. Mialane. Hybrid Organic−Inorganic Polyoxometalate Compounds: From Structural Diversity to Applications. *Chemical Reviews* 110 (10), 6009. (2010)

[24] A. Amokrane, S. Klyatskaya, M. Boero, M. Ruben and J-P. Bucher. The Role of π-Radicals in the Spin Connectivity of Clusters and Networks of Tb Double-Decker Single Molecule Magnets, *ACS Nano* 11, 10750. (2017)

[25] T. Komeda, H. Isshiki, J. Liu ,Y. Zhang, N. Lorente, K. Katoh, B. Breedlove and M. Yamashita. Observation and electric current control of a local spin in a single-molecule magnet. *Nature Communication* 2, 217. (2011)

[26] Y. Zhang, H. Isshiki, K. Katoh, Y. Yoshida, M. Yamashita, M. Hitoshi, B. Breedlove, T. Kajiwara, S. Takaishi and T. Komeda, Low-Temperature Scanning Tunneling Microscopy Investigation of Bis(phthalocyaninato)Yttrium Grown on Au(111): From Individual Molecules to Two-Dimensional Domains. *Journal of Physical Chemistry C* 113, 9826. (2009)

[27] F. Ara, Z.K. Qi, J. Hou, T. Komeda, K. Katoh, M.Yamashita. A Scanning Tunneling Microscopy Study of the Electronic and Spin States of Bis (phthalocyaninato) terbium(III) ($TbPc_2$) Molecules on Ag(111). *Dalton Transactions* 45, 16644. (2016)

[28] L. Malavolti, M. Mannini, P.E. Car, G. Campo, F. Pineider and R. Sessoli. Erratic magnetic hysteresis of $TbPc_2$ molecular nanomagnets. *Journal of Materials Chemistry C* 16, 2935. (2013)

[29] I.V. Krainov, J. Klier, A.P. Dmitriev, S. Klyatskaya, M. Ruben, W. Wernsdorfer and I.V. Gornyi. Giant magnetoresistance in carbon nanotubes with single-molecule magnets $TbPc_2$, *ACS Nano* 11, 6868. (2017)

[30] J. Kondo, Anomalous Density of States in Dilute Magnetic Alloys. *Progress of Theoretical Physics* 33**,** 575. (1965)

[31] J. Kondo, Resistance minimum in dilute magnetic alloys. *Progress of Theoretical Physics.* 32**,** 37. (1964).

[32] J. Friedel, On some electrical and magnetic properties of metallic solid solutions. *Canadian Journal of physics.* 34, 1190. (1956)

[33] K. Yosida, Anomalous Electrical Resistivity and Magnetoresistance Due to an s-d Interaction in Cu-Mn Alloys. *Physical Review* 107**,** 396. (1957)

[34] A. Abrikosov, A. On the Anomalous Temperature Dependence of the Resistivity of Non-magnetic Metals with a Weak Concentration of Magnetic Impurities. *Soviet Journal of Experimental and Theoretical Physics.*

[35] H. Suhl, Dispersion Theory of the Kondo Effect. *Physical Review* 138**,** 515. (1965)

[36] U. Fano, Sullo spettro di assorbimento dei gas nobili presso il limite dello spettro d'arco, *Nuovo Cimento* 12, 156. (1935)

[37] P.W. Anderson, A poor man's derivation of scaling laws for the Kondo problem. *Journal of Physics C: Solid State Physics* 3**,** 2436. (1970)

[38] J.R. Schrieffer and, P. A. Wolff, Relation between the Anderson and Kondo Hamiltonians. *Physical Review* 149**,** 491. (1966)

[39] K.G. Wilson. The renormalization group: Critical phenomena and the Kondo problem. *Reviews of Modern Physics.* 47, 773. (1975)

[40] P. Nozières, A Fermi-liquid description of the Kondo problem at low temperatures. *Journal of Low Temperature Physics* 17**,** 31. (1974)

[41] M. Plihal and J.W. Gadzuk. Nonequilibrium theory of scanning tunneling spectroscopy via adsorbate resonances: Nonmagnetic and Kondo impurities. *Physical Review B,* 63**,** 85404. (2001)

[42] A. Rosch, J. Paaske, J. Kroha, and P. Wolfle, The Kondo Effect in Non- Equilibrium Quantum Dots: Perturbative Renormalization Group. *Journal of the Physical Society of Japan* 74**,** 118. (2005)

[43] A. Hewson, *The Kondo Problem to Heavy Fermions,* 43, 102. (1993)

[44] V. Madhavan, W. Chen, T. Jamneala, M.F. Crommie and N.S Wingreen. Local spectroscopy of a Kondo impurity : Co on Au(111). *Physical Review* 64**,** 1. (2001)

[45] M.Ternes, A.J. Heinrich, and W.D. Schneider. Spectroscopic manifestations of the Kondo effect on single adatoms. *Journal of Physics: Condensed Matter* 21**,** 053001. (2009)

[46] J. Li, W.D. Schneider, R. Berndt and B. Delley. Kondo Scattering Observed at a Single Magnetic Impurity. *Physical Review Letters* 80, 2893. (1998)

[47] Zhang, Zhao, Wang & Xiao. Kondo effect of single Co atoms adsorbed on Pb / Si (111) nanoislands. *Physical Review B* 78, 35431. (2008)

[48] P. Wahl. Kondo Temperature of Magnetic Impurities at Surfaces. *Physical Review Letters* 93, 176603. (2004)

[49] W. Chen, T. Jamneala, V. Madhavan and M. Crommie. Disappearance of the Kondo resonance for atomically fabricated cobalt dimers. *Physical Review B* 60**,** 8529. (1999)

[50] P. Wahl, Exchange Interaction between Single Magnetic Adatoms. *Physical Review Letters* 98, 56601. (2007)

[51] V. Iancu, A. Deshpande and S.W. Hla. Manipulation of the Kondo Effect via Two-Dimensional Molecular Assembly. *Physical Review Letters* 97, 266. (2006)

[52] T. Choi, S. Bedwani, A. Rochefort, C-Y. Chen, A. Epstein and J-A. Gupta. A single Molecule Kondo Switch: Multistability of Tetracyanoethylene on Cu(111). *Nano Letters* 10, 4175. (2010)

[53] R. Tuerhong, F. Ngassam, S. Watanabe, J. Onoe, M. Alouani and J.P. Bucher, Two-Dimensional Organometallic Kondo Lattice with Long-Range Antiferromagnetic Order. *Journal of Physical Chemistry C* 122, 20046. (2018)

[54] C. Dekker. Carbon Nanotubes as Molecular Quantum Wires. *Physics Today* 52, 22. (1999).

[55] Y-H. Zhang, S. Kahle, T. Herden, C. Stroh, M. Mayor, U.Schlickum, M. Ternes, P. Wahl and K. Kern. Temperature and magnetic field dependence of a Kondo system in the weak coupling regime. Nature, 4, 2110. (2013)

[56] Hellwig, R.; Paintner, T.; Chen, Z.; Ruben, M.; Seitsonen, A. P.; Klappenberger, F.; Brune, H.; Barth, J.V. Epitaxy-Induced Assembly and Enantiomeric Switching of an On-Surface Formed Dinuclear Organocobalt Complex. *ACS Nano* 11, 1347. (2017

CHAPTER 2

Experimental methods

In this chapter, we will describe the implemented experimental methods of molecular and metal evaporation. Afterwards, we present the description of the experimental equipment used in the Institute of Physics and Chemistry of Materials of Strasbourg (IPCMS), including the Scanning Tunneling Microscopy (STM) and the Scanning Tunneling Spectroscopy (STS) operating at very low temperatures.

2.1 Evaporation methods

2.1.1 Molecular evaporation

The evaporation of the molecules is ensured by a home-built evaporator (see Figure 2.1 (a)). This evaporator consists of a crucible surrounded by a tungsten filament (W) of the diameter of 0.25 mm. A thermocouple is immersed directly in the crucible to control the evolution of the temperature as a function of the current injected into the filament. The crucible containing the molecules powder is degassed beforehand for several hours, it is heated to a temperature slightly lower than that of the evaporation.

For the MPc_2 (M = Tb, Y), this molecular evaporator was calibrated at the evaporation rate of 0.4 ML/min at the evaporation temperature of 630 K. The pressure in the evaporation room during deposition is of the order of 10^{-9} mbar.

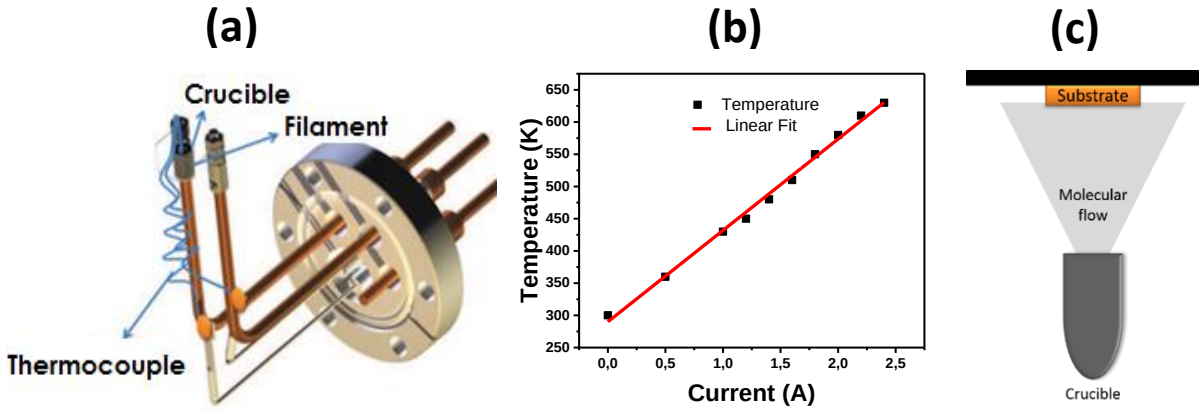

Fig. 2.1: (a) The home-built molecular evaporator. (b) The temperature as function of the current intensity through the filament. (c) Simplified schematic representation of the molecular evaporation procedure under UHV, The distance between the substrate and crucible is about 6 cm.

The Table 2.1 below reports a summary of all the molecules used in this thesis, evaporation temperatures and deposition time.

Molecule	Evaporation temperature (K)	Deposition time ($ML.min^{-1}$)
$TbPc_2$	630	2.5
YPc_2	630	2.5
NC-Ph_3-CN	320	6
NC-Ph_5-CN	470	4.5
NC-Ph_6-CN	520	3.5

Tab. 2.1: Deposition time as a function of evaporation time and temperature.

2.1.2 Metal evaporator

The deposition of the metal atoms (Co and Fe) is carried out using an Electron-Beam Evaporator (EFM3). The evaporator is degassed under vacuum before use. The control of temperature is ensured by a feedback loop. The entire body of the cell is cooled by a circulation of water to keep low temperatures inside the evaporator. The cell is equipped with a shutter at the end to ensure good calibration during the deposit. As shown in the Figure 2.2 (b), a filament produces electrons, while a high voltage up to 860 V is applied to the cobalt or iron rod. Locally the rod is heated and evaporates metal ions onto the sample with a rate of less than 1 ML/minute. The flow of metal atoms is controlled by the microprocessor Focus EVC power supplies.

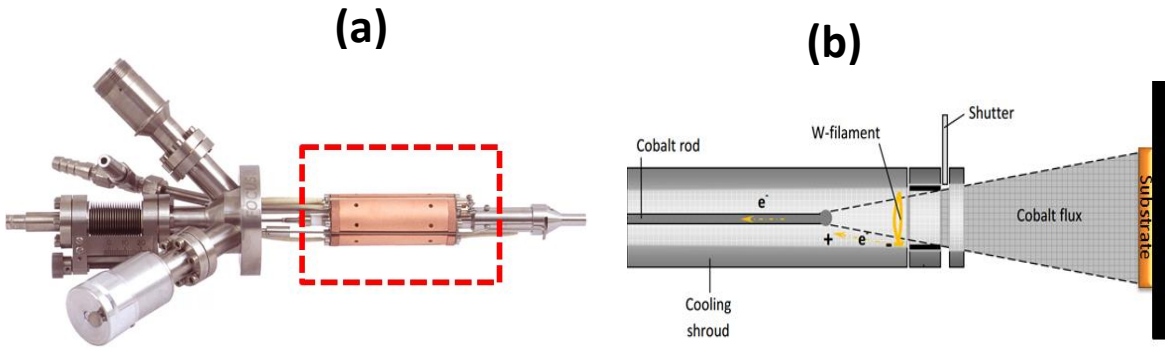

Fig. 2.2: (a) Photography of EFM3 evaporator showing a general view with marked cell (red dashed-line rectangle). (b) Simplified representation illustrates the principle of evaporator operation.

2.2 Tip and sample preparation

2.2.1 Tip preparation

During this thesis, we have used exclusively W-tips prepared by the electrochemical etching method of a tungsten (W) wire, 0.25 mm in diameter. The etching is carried out with a solution of NaOH (10%). After having cut with the pliers and mounted the tip on a tip-holder, the holder is introduced in a UHV chamber in order to be treated by Ne^+ bombardment. Then, electron bombardment at 10 mA for less than 5 minutes is used in order to clean the tip of any contamination caused by the etching process. Finally, the tip is introduced into the STM chamber to perform the nano-indentation of the tip into a pristine crystal. This process is repeated until stable and contamination-free apex is obtained.

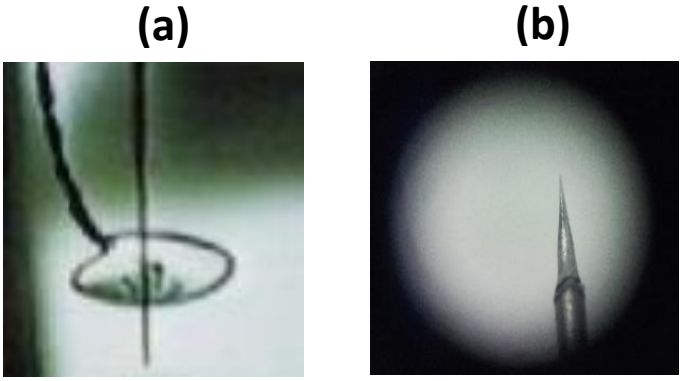

Fig. 2.3: Preparation method of an STM tip: (a) Electrochemical etching of a tungsten (W) piece with an NaOH solution (10%). (b) Real photo of an STM Tip.

2.2.2 Sample preparation

In order to investigate the MPc_2 (M = Tb, Y) molecule adsorbed on Au(111), Ag(111) and Cu(111) substrates we prepared several samples at various molecular coverages. All substrates are prepared by multiple cycles of Ne^+ bombardment and *in-situ* annealing. Extended contamination free terraces under STM investigation were an indication of success. Once prepared, the crystal is transferred back into the evaporation chamber where molecular deposition is performed at suitable conditions. The sample is subsequently transferred to the STM head to be characterized at very low temperatures (4.6 K).

2.3 Experimental UHV equipment

The ultra-high vacuum (UHV, $P \approx 10^{-10}$ mbar) equipment used for the preparation and characterization of the samples *in-situ* by tunneling microscopy / spectroscopy is represented by the Figure 2.4. This equipment is composed of 4 main chambers:

- A chamber (1) is dedicated for the preparation of samples where the surface is cleaned by alternating cycles of sputtering and annealing.
- An evaporation chamber (2) where home-built evaporation sources are housed.
- A chamber (3) called Load-lock is dedicated to the sample and tip introduction from atmospheric area to avoid any vacuum breaking in the main chambers.
- A chamber (4) in which a Createc® low temperature microscope is installed.

The chambers are separated from each other by gate valves and the vacuum is achieved by a set of Turbo and Ionic pumps running permanently. The complete system is supported by Newport active vibration isolation dampers (5).

In our experimental equipment, it is possible to characterize a sample at several scales. The structural or electronic properties can be studied using a tunneling microscope operating at temperatures between 4.6 and 300 K. During this thesis, the temperatures at which the STM images and the STS spectroscopy is performed is 4.6 K (Helium liquid temperature) or 77 K (Nitrogen liquid temperature). We can see in the Figure 2.5, an image obtained with our microscope on an Au(111) surface showing a chevron reconstruction ($22 \times \sqrt{3}$) and a spectrum dI/dV showing a step in conductance, characteristic of Schockley state of Au(111).

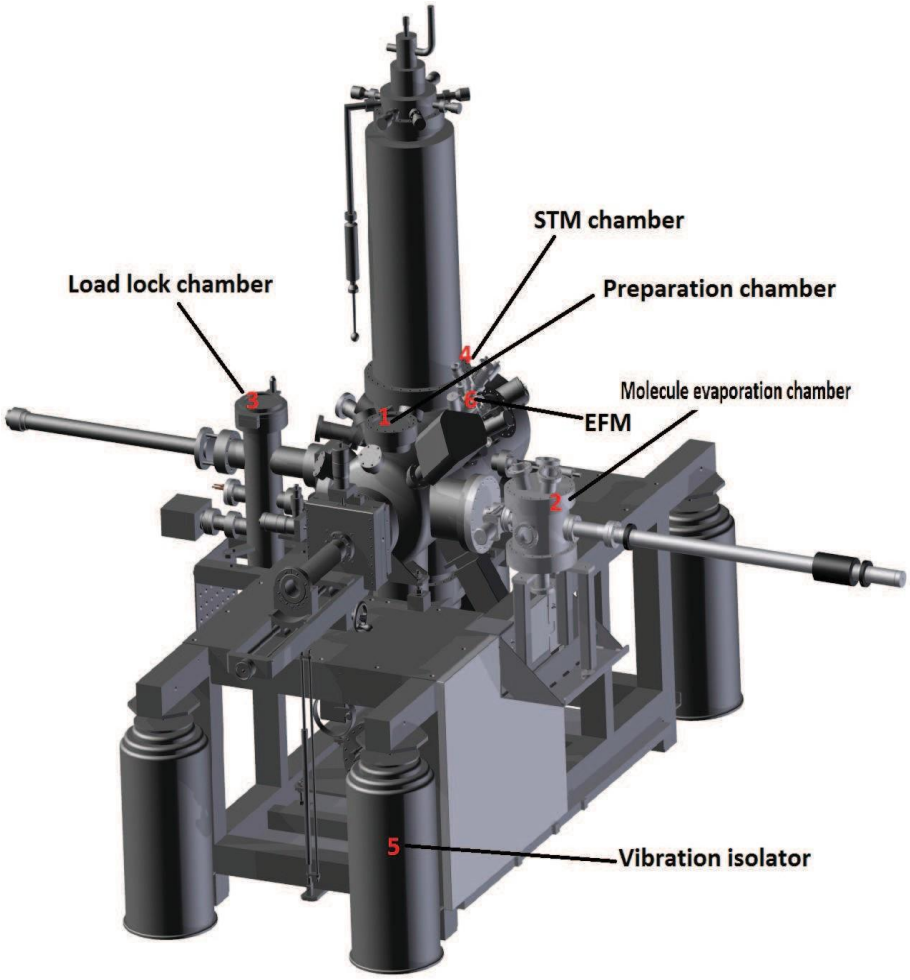

Fig. 2.4: Perspective view of the UHV system with its components: (1) preparation chamber, (2) evaporation chamber, (3) load-lock chamber, (4) STM chamber and vibration system (5).

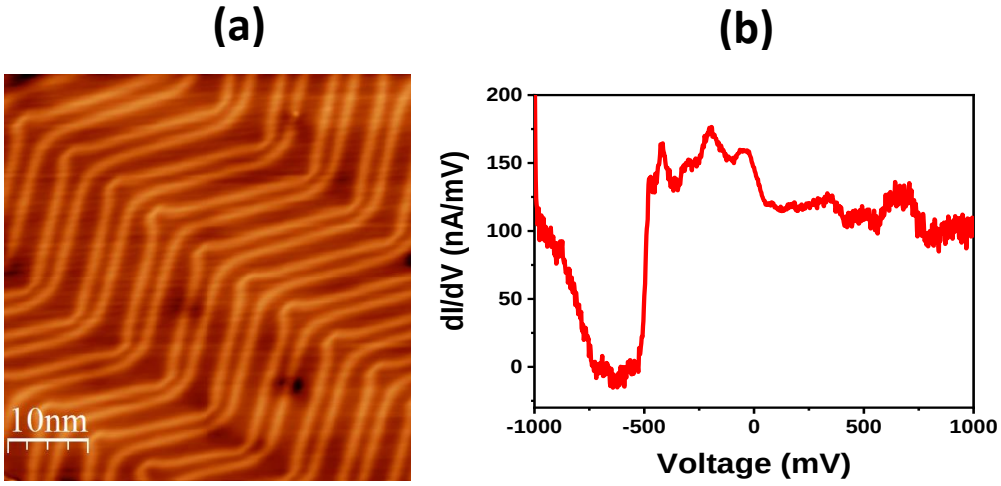

Fig. 2.5: Example of experimental results obtained by STM / STS on an Au(111) surface. (a) Topographic STM image showing surface reconstruction. (b) conductance spectrum revealing Shockley state (-500 mV) as a step.

2.4 Scanning Tunneling Microscope (STM)

2.4.1 Introduction

The scanning tunneling microscope (STM) was developed in 1982 by Gerd Binnig and Heinrich Rohrer [1]. Thanks to this discovery, the two inventors received the Nobel Prize in 1986. This technique is the most fascinating because it allows to probe the matter on the atomic scale and to discover the inaccessible nanoworld of atoms. The first success of the STM was to observe the reconstruction (7 × 7) of surface Si (111) reported by the Figure 2.6 (a). This instrument allows the characterization and manipulation of nanostructures on metal surfaces, see for example the work Cromie et al. [2] where a quantum corral was built by manipulating Fe atoms on the surface of Cu(111) (Figure 2.6 (b)).

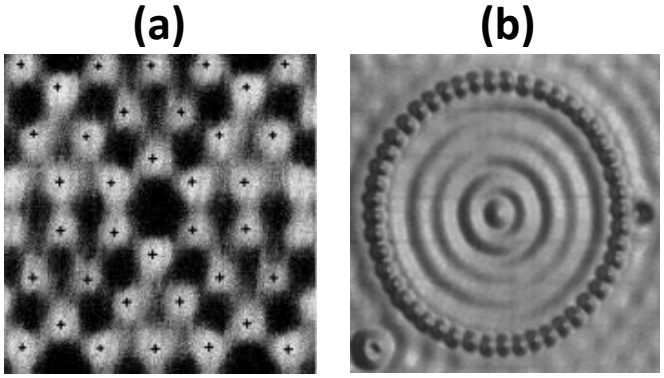

Fig. 2.6: (a) Reconstruction (7 × 7) of a surface of Si(111), taken from [3]. (b) Spatial image of the eigen states of a quantum corral formed by manipulation of 48 Fe atoms on Cu(111), taken from [2].

2.4.2 Principle of tunneling

The operation of the STM relies on the tunneling effect through a potential barrier as shown in the Figure 2.7. Indeed, quantum mechanics allows electrons passage of an m_e (electron mass) through the barrier even if their kinetic energy E is less than the height of the barrier U_0. A wave function can thus describe this process [4].

$$\psi(z) = \psi(0)e^{-\frac{\sqrt{2m_e(U_0-E)}z}{\hbar}} \qquad (2.1).$$

The probability of presence of the electron inside the barrier is therefore proportional to $|\psi(z)|^2 = |\psi(0)|^2 e^{-2\left(\frac{\sqrt{2m_e(U_0-E)}z}{\hbar}\right)}$. The exponential decay of the probability in Figure 2.7 explains the high sensitivity of STM.

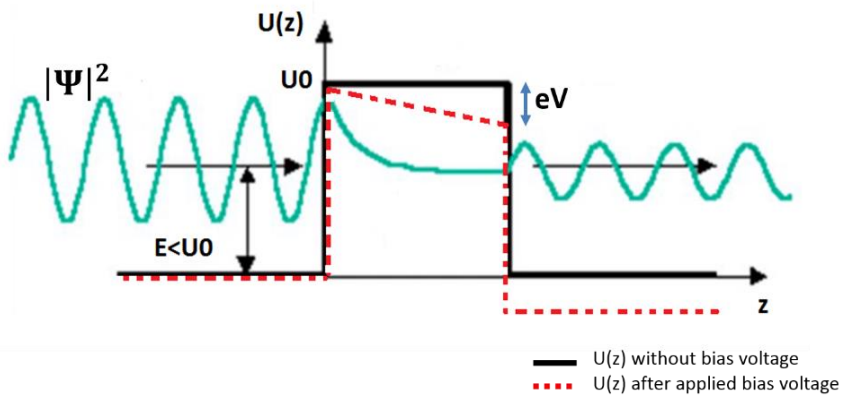

Fig. 2.7: Quantum regime, representation of tunneling barrier before (black line) and after (dashed red line) applied bias voltage, an electron has a certain probability to penetrate the barrier and tunnel through.

The tunneling effect is observed experimentally in the metal-insulator-metal junction. In STM, insulator is the gap between the tip (metallic) and the surface (metallic, conductive). The width of the barrier corresponds to the tip-surface distance *z*. when the tip is sufficiently close to the surface (about 1 nm), by applying a voltage bias, we obtain a tunnel current (of the order of a few pico to a few nano-amperes). The tunneling current depends exponentially on *z* which allows the tip-surface distance to be controlled with high precision. The displacement of the tip relative to the surface is ensured by a piezoelectric tube allowing a displacement in all directions (x, y, z) as shown in the Figure 2.8.

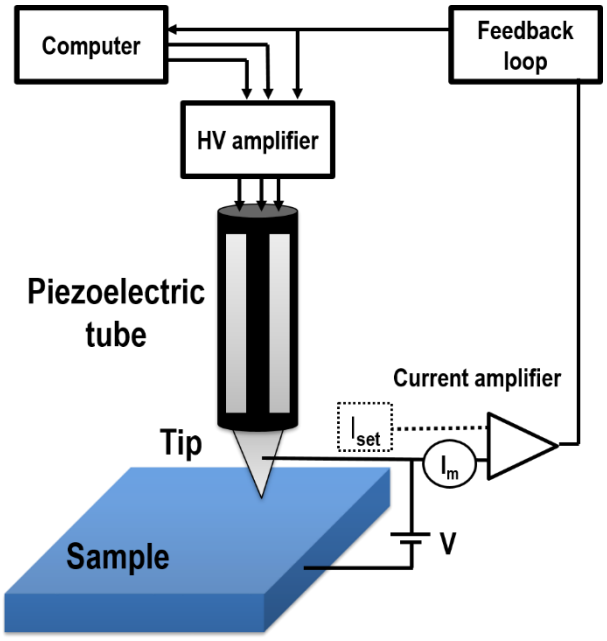

Fig. 2.8: Illustration of the main components ensuring the STM operation.

To image the sample surface, two scanning modes can be used:

• Constant current mode: the tunneling current is defined constant and using a feedback loop controlling the elongation of the piezoelectric tube in *z* direction, we record the tip-surface topography (as shown in the Figure 2.9 (a)). In this mode, the tip reproduces perfectly the corrugations of the surface. The recorded image is a real 3D map of the surface.

• Constant height mode: here, the feedback loop is locked, the tip-surface distance is kept constant, the current variations are measured (as shown in the Figure 2.9 (b)). In this mode, it must first be ensured that the surface is perfectly flat to prevent damage to the tip.

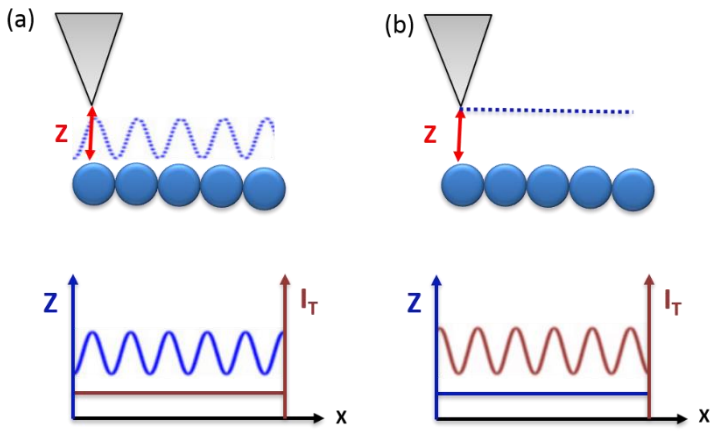

Fig. 2.9: Illustration of the two STM operating modes: (a) Constant current scanning mode. (b) Constant height scanning mode.

The active part of the microscope is represented in Figure 2.10 (b). This part is connected to a cryostat ensuring the good thermalization of the sample, piezoelectric tube and tip to LN and/or LHe temperatures. An STM / AFM program makes it possible to control the movements of the piezoelectric tube for the approach of the tip step-by-step, so as not to damage the apex on the surface of the sample. The piezoelectric tube sensitivity to an applied voltage os typically reduced by factor 2 between liquid nitrogen temperature (77 K) and liquid helium temperature (4 K). The tip is attached magnetically in its receptacle at the lower end of the piezo-electric tube by a permanent magnet. The translational driving signals (x, y, z) of the tube together with the parameters of tunnel current and bias voltage are collected and conveyed along the cryostat to the top and then tied by BNC connectors to DSP (Digital Signal Processor) electronic component. The DSP is controlled by the computer through STM/AFM program.

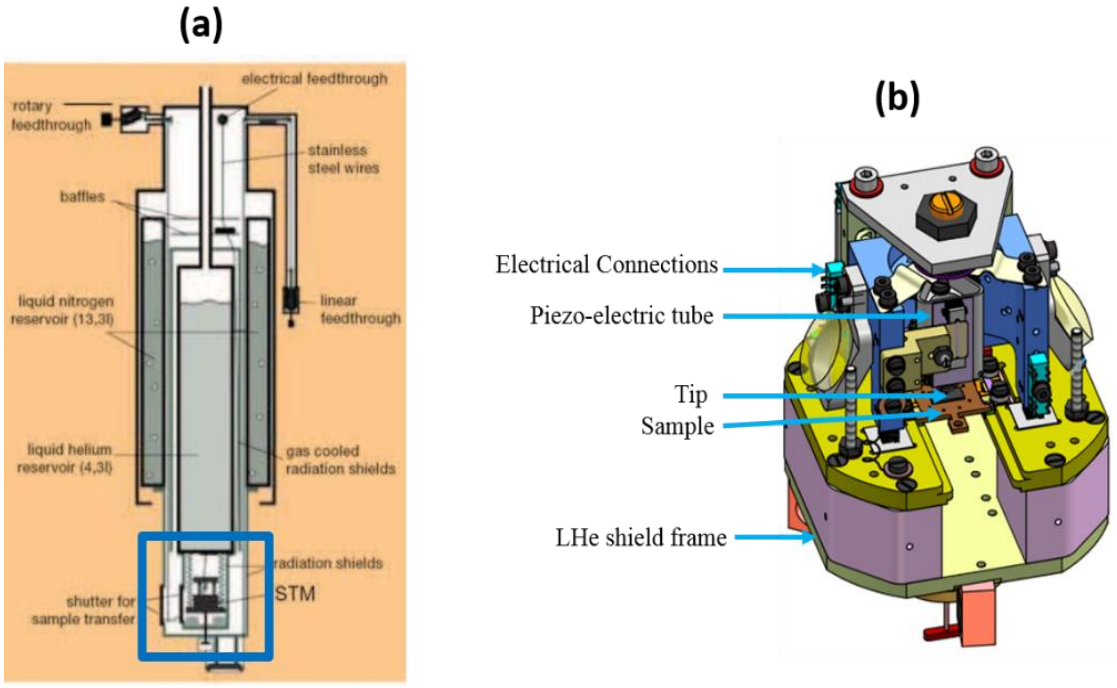

Fig. 2.10: Schematic representation of a cryostat connected to an STM (marked by the blue square). (b) 3D image of the STM head (provided by Createc®).

Our microscope can operate at either 300K (room temperature) or low temperatures (4.6K and 77K). The microscope has two reservoirs as shown in the Figure 2.10 (a). The first one is external, and may contain liquid nitrogen (about 13 liters) while the second contains (about 4.3 liters) either liquid nitrogen (to work at 77 K) or liquid helium (to work at 4.6 K). The autonomy of operation is about 72 hours when we work at 77 K and 48 hours when we work at 4.6 K.

Tersoff and Hamann's model

To interpret the first STM images, Tersoff and Hamann [5, 6] developed a model based on the Bardeen formalism [7], for the tunneling current on a metal-insulator-metal junction:

$$I(V) = \frac{2\pi e}{\hbar}\sum_{s,p}\left|M_{p,s}\right|^2 f(E_p)[1 - f(E_s - eV)]\delta(E_p - E_s) \qquad (2.2)$$

With $f(E)$, the Fermi function and $M_{p,s}$ the transition matrix between the Ψ_p state of the tip and Ψ_s of the surface, with respective energies E_p and E_s, and V the applied voltage (bias) between the tip and the sample. The transfer matrix is defined by:

$$M_{p,s} = \frac{\hbar^2}{2m_e}\int (\Psi_p^*\vec{\nabla}\Psi_s - \Psi_s\vec{\nabla}\Psi_p^*)d\vec{S} \qquad (2.3)$$

To model the tip, Tersoff and Hamann have considered that the tip is comparable to a spherical potential well of φ_p height, corresponding to the work function of the tip. The relationship can be written as:

$$I(V,z)) \propto \frac{eV}{\hbar}\int_{-\infty}^{+\infty}\rho_s(E)\rho_p(E+eV)T(E,z)[f(E-eV)-f(E)]dE) \qquad (2.4)$$

Where z is the tip-surface distance, ρ_s and ρ_p are respectively the density of state of the surface and the tip, and $T(E,z)$ is the transmissivity such as:

$$T(E,z) = \exp\left(-\frac{2}{\hbar}\sqrt{m_e(\varphi_s+\varphi_p-2E+eV)}z\right) \qquad (2.5)$$

Where φ_p and φ_s are the work function of the surface and the tip respectively.

At low temperatures, we obtain the following relation:

$$I(V,z,T\neq 0K)) \propto e^{-\alpha z}\int_{-\infty}^{+\infty}\rho_s(E)\rho_p(E-eV)[f(E-eV)-f(E)]dE \qquad (2.6)$$

With $\alpha = \frac{\sqrt{2m(U_0-eV)}}{\hbar}$, U_0 is the barrier height for zero voltage.

Therefore, the measured tunneling current depends on the electronic states of the surface and the tip.

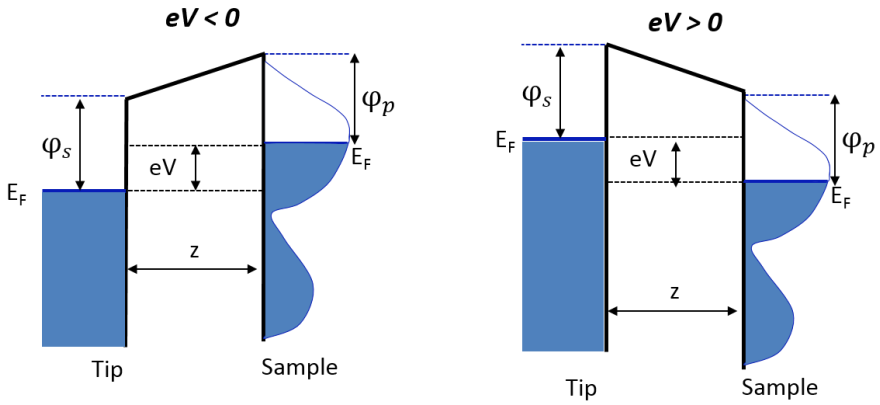

Fig. 2.11: Illustration of the tunneling junction between the tip and the sample when a voltage V is applied: (Left): Negative V (the electrons go from the sample to the tip); (Right): the electrons go from the tip to the sample.

2.4.3 Scanning tunneling spectroscopy (STS)

The scanning tunneling microscope is not only capable of imaging a sample surface, but can also be used for spectroscopic measurements at the atomic scale. Scanning tunneling

spectroscopy (STS) can measure the local electronic structure [8] of the sample as well as inelastic processes excited by tunneling electrons. STS can provide informations of the functionality of a molecule or an atom, which is essential for possible applications like molecular electronics. It is also possible to observe fundamental phenomena such as the spin-flip of an atomic spin [9], or the Kondo resonance of a single atom [10].

When looking at the electronic properties of an object on a metallic surface, two types of spectroscopies can be achieved:

1) A local spectroscopy where we measure the differential conductance (dI/dV) (proportional to LDOS) at a fixed position of the tip above the object (atom, adatom or molecule).

2) A mapping of the differential conductance measured at any point of an image at a fixed voltage V_0, dI/dV = f (V_0, x, y).

The relation between the differential conductance (dI/dV) and LDOS of the surface can be found by calculating the first derivatives of tunneling current Equation (2.6) with respect to the applied bias voltage V. When assuming a constant tip DOS equals to the DOS at Fermi level, and if we assume T to be constant in energy close to the Fermi level, the differential conductance (dI/dV) can be written as:

$$\frac{dI}{dV}(V,T) \propto \rho_s(eV) \qquad (2.7)$$

So, the conductance is proportional to the local density of states (LDOS) of the surface at one specific point.

In our case, the surface is often covered with molecules. With their own well defined electronic states coupled to the substrate. Particularly relevant are two specific states, the frontier orbitals corresponding to Highest Occupied Molecular Orbital (HOMO) and the Lowest Unoccupied Molecular Orbital (LUMO). Accordingly, the Fermi level is found in the middle of the HOMO-LUMO gap. The positions of these levels are strongly modified by the interactions between the molecule and the substrate [11-13]. This issue will be discussed from the experimental results of this thesis.

Figure 2.12 shows an example of STS measurements on $TbPc_2$ deposited on Cu(111) The spectra of figure 2.12 b show two apparent peaks: The first one located in the occupied region at around - 700 meV and the other at around + 700 meV, which could be assigned to HOMO

and LUMO resonances respectively, yielding an apparent gap of about 1.4 eV. The Figure 2.12 c shows the dI/dV maps recorded above the isolated $TbPc_2$ molecule at -700 meV and exhibits a conductance localization above the central Tb ion of the molecule (Red) no conductance contribution from the Pc ligand (blue) is observed at this energy.

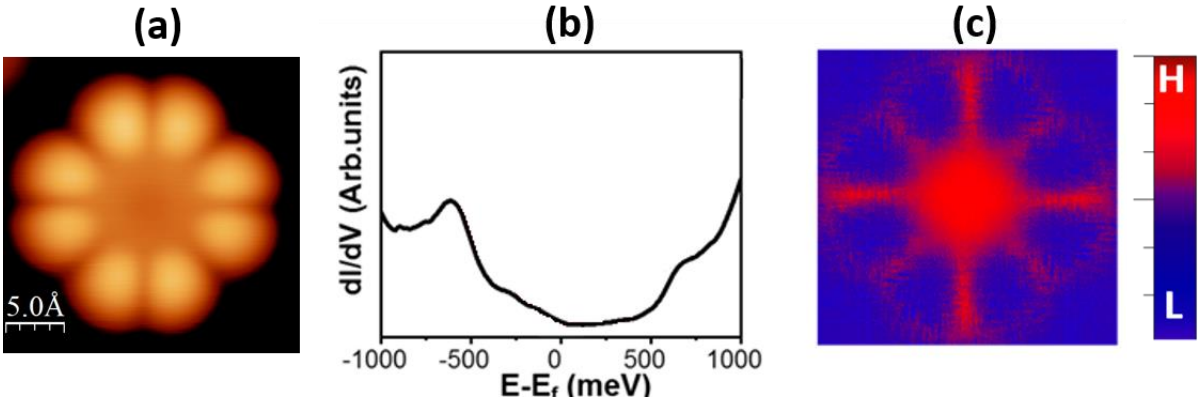

Fig. 2.12: Example of experimental results obtained by STM/STS on $TbPc_2$ deposited on Cu(111). (a) Topographic STM image of $TbPc_2$. (b) Conductance spectrum (dI/dV) acquired at the center revealing the HOMO and LUMO states. (c) dI/dV maps at occupied states (-0.7 V). Red: high conductance, blue: low conductance.

REFERENCES

[1] G. Binnig, H. Rohrer, C. Gerber and E. Weibel. Tunneling Through a Controllable Vacuum Gap. *Applied Physics Letters* 40, 178. (1982)

[2] M. F. Crommie, C. P. Lutz and D. M. Eigler. Confinement of Electrons to Quantum Corrals on a Metal Surface. *Science* 218, 262. (1993).

[3] G. Binnig, H. Rohrer, C. Gerber and E. Weibel. 7x7 Reconstruction on Si(111) Resolved in Real Space. *Physical Review Letters* 50, 120. (1983)

[4] C. Cohen-Tannoudji, B. Diu and F. Laloë. Mécanique Quantique (1998).

[5] J. Tersoff and D. R. Hamann. Theory of the Scanning Tunneling Microscope. *Physical Review B* 31, 805. (1985)

[6] J. Tersoff and D. R. Hamann. Theory and Application for the Scanning Tunneling Microscope. *Physical Review Letters* 50, 1998. (1983)

[7] J. Bardeen. Tunneling from a Many-Particle Point of View. *Physical Review Letters* 6, 57. (1961)

[8] G. Binnig, KH. Frank, H. Fuchs, and N. Garcia. Tunneling spectroscopy and inverse photoemission: image and field states. *Physical Review Letters* 55, 991. (1985)

[9] A J. Heinrich, J A Gupta, C P Lutz, and D M Eigler. Single-atom spin-ip spectroscopy. *Science* 306, 466. (2004)

[10] V. Madhavan, W. Chen, T. Jamneala, M.F. Crommie and N.S Wingreen. Local spectroscopy of a Kondo impurity: Co on Au(111). *Physical Review* 64**,** 1. (2001)

[11] H. Ishii, K. Sugiyama, E. Ito and K. Seki. Energy Level Alignment and interfacial electronic structures at organic/metal and organic/organic interfaces. Advanced Materials 11, 605. (1999)

[12] L. A. Bumm, J. J. Arnold, T. D. Dunbar, D. L. Allara and P. S. Weiss. Electron Transfer through Organic Molecules. Journal Physical Chemistry B 103, 8122. (1999)

[13] T. G. Gopakumar, J. Meiss, D. Pouladsaz and M. Hietschold. HOMO-LUMO Gap Shrinking Reveals Tip-Induced Polarization of Molecules in Ultrathin Layers: Tip-Sample Distance-Dependent Scanning Tunneling Spectroscopy on d 8 (Ni, Pd, and Pt) Phthalocyanines. Journal of Physical Chemistry C 112, 2529. (2008)

CHAPTER 3

Structural properties of MPc_2 (M = Tb,Y) growth on metal surfaces Au(111), Ag(111) and Cu(111)

3.1 Introduction

Nowadays, the process of molecular self-assembly [1-3] is a technique for the formation of new organic or metal-organic components. The spontaneous formation of molecular nanostructures allows the growth of ordered supramolecular networks with specific architectures. The design of the molecular network is based on the non-covalent interactions. A particularly interesting molecule class $LnPc_2$ has attracted much interest from chemists and physicists in recent decades, their adsorption, mobility, and inter- and intra-molecular interaction depend essentially on the substrates, crystalline lattice, chemical nature and symmetry [4-7].

In this chapter, we have focused on the adsorption of the $TbPc_2$ molecule on Au(111), Ag(111) and Cu(111) surfaces in order to study the structure of molecular domains growth. Furthermore, we study the growth of YPc_2 on Au(111) to have a point of comparison with $TbPc_2$. Subsequently, we are interested in the molecule adsorbed as a second monolayer in order to identify its coupling with respect to the first monolayer.

The molecules of $TbPc_2$ and YPc_2 are deposited by sublimation under ultra-High-Vacuum (UHV) and at room temperature. First, we describe the formation of $TbPc_2$ and YPc_2 self-assemblies on Au(111) substrate. Then we describe the different adsorption geometries of first- and second-layer of $TbPc_2$ on Ag(111) substrate. Finally, the molecules of $TbPc_2$ and YPc_2 are deposited by sublimation under ultrahigh vacuum (UHV) and at room temperature. Two types of lateral intermolecular interactions and molecule-substrate lead to the formation of periodic molecular networks. We present the distribution of the $TbPc_2$ molecules on the Cu(111) surface, isolated self-assembly on first- and second-layer. On different substrates, we discuss the

different network parameters, the crystallographic direction with respect to the substrate and apparent adsorption height of individual and molecular domain.

3.2 MPc_2 (M = Tb, Y) growth on Au(111)

Terbium and Yttrium double-decker molecules have been synthesized following the protocol described in [8] by Dr. Svetlana Klyatskaya in the group of Prof. Dr. Mario Ruben at the Karlsruhe Institute of Technology (KIT). The molecule is composed of two phthalocyanine ligands (Pc, chemical formula $C_{32}H_{18}N_8$) and a lanthanide metal atom. The MPc_2 molecule (M = Tb, Y) consists of a central metal ion (M) coordinated to two phthalocyanines (Pc), the metal ion is therefore sandwiched between two ligands as shown in Figure 3.1 (b). In this structure, the M ion is coordinated to eight pyrrole nitrogen (four N from each ligand) and plays the role of a semi-flexible joint to ensure the orientation (up to 45 °) of the upper Pc with respect to the lower Pc (V_1 with respect to V_2 in Figure 3.1 (b)).

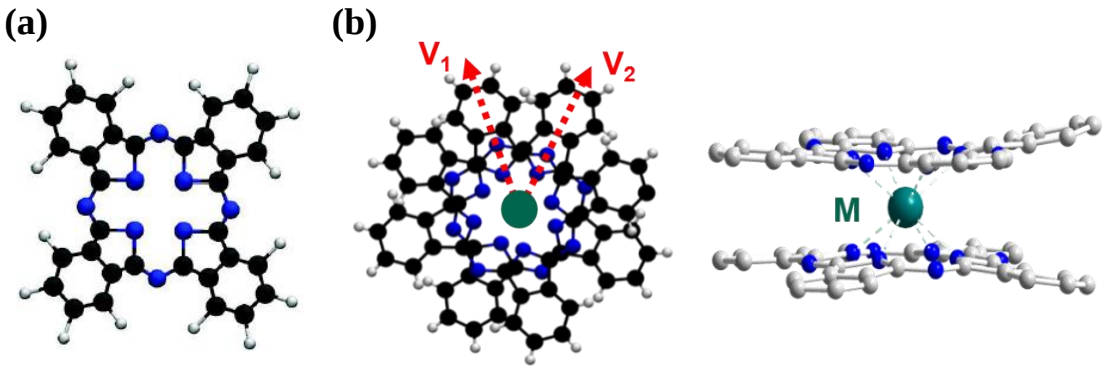

Fig. 3.1: (a) Model of phthalocyanine ligand (Pc), the chemical formula is $C_{32}H_{18}N_8$. Color code: Blue = Nitrogen; Black = Carbon; White = Hydrogen; Green = M (Terbium or Yttrium). (b) MPc_2 molecule, Top and side view, V_1 and V_2 are respectively the symmetry axis of the upper and lower Pc.

We have used the STM at 4.8 K to reveal the self-assembly behavior of MPc_2 molecules on the Au(111) surface. Our previous experiments have shown that the molecule has a high mobility on the gold surface at room temperatures and at 77K, which makes it almost impossible to make topographic images on the growth area at this temperature. Figures 3.2 (a) and (b) show that the $TbPc_2$ molecule is visualized in STM by the 8 lobes of its upper ligand originating from the π-orbitals in coherence with the single molecule studies, where 8 lobes associated with the upper ligand are clearly visible [9,10]. With a coverage rate equal to one monolayer (ML), we notice that the growth of $TbPc_2$ on Au(111) leads to two different molecular arrangements:

Phase I represented in Figure 3.2 (a) and Phase II represented in Figure 3.2 (b).

As shown in the Figure 3.2 (a), The molecular domain I (with Phase I) is oriented along D at an angle of 40° with the crystallographic direction [1$\bar{1}$0] of Au(111) substrate. On the other hand, in the domain II, the presence of small voids surrounded by green circles in Figure 3.2 (b) proved that the molecular layer results from the coalescence of several domains that have different directions.

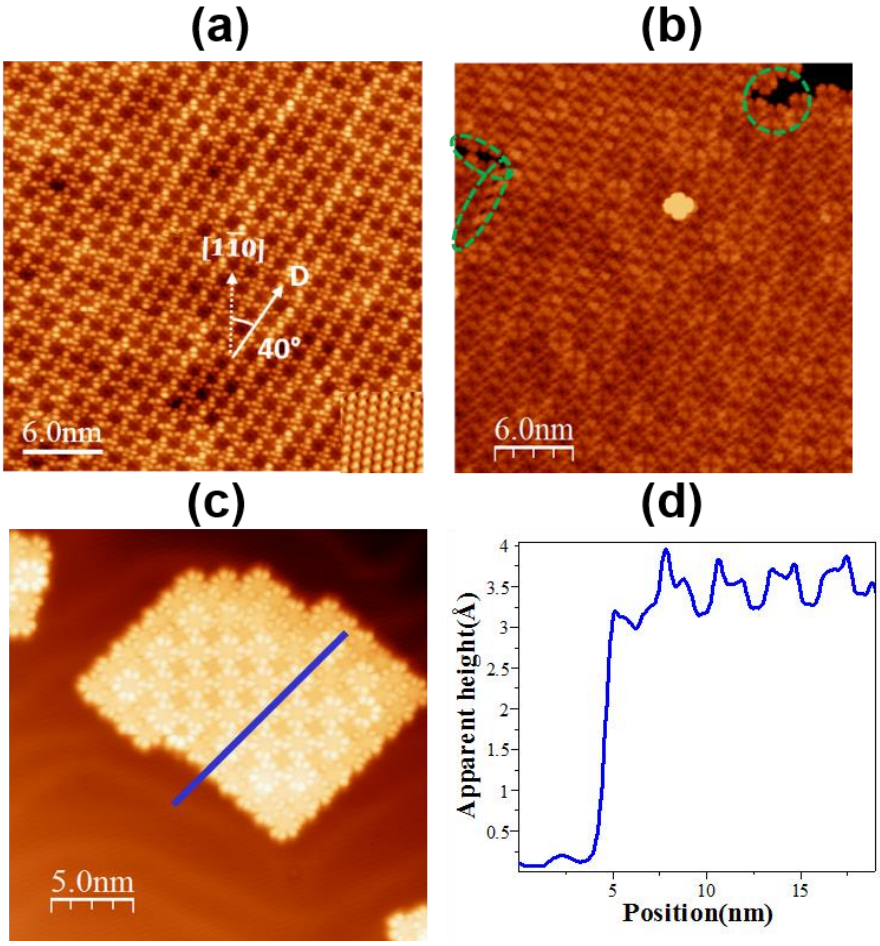

Fig. 3.2: STM images of $TbPc_2$ grown on Au(111). (a) Molecular domain of Phase I (V_S = -1.0 V, I_T = 80 pA). The molecule orientation makes an angle of 40° with respect to the [1$\bar{1}$0] direction of the Au substrate (inset: 2 nm x 2 nm; V_S = -0.2 V, I_T = 100 pA); (b) Molecular domain of Phase II (V_S = -0.7 V, I_T = 70 pA). (c) molecular domain growth of YPc_2 on Au(111) shows blue line scan across the monolayer (blue line). (d) Apparent height of YPc_2 domain.

With a lower coverage than a monolayer, as shown in Figure 3.2 (c), the adsorption of MPc_2 reveals rectangular islands oriented in the same direction D. The height of the molecular films adsorbed on Au(111) depends essentially on the molecular structure of the network and the crystallographic directions of the substrate [11], it is of the order of 0.35 nm, comparable to

individual single YPc_2 molecule on Au(111) [10]. Other height profiles were found on the two different growth domains of $TbPc_2$ on Au(111), we have found that they have the same apparent height of 0.4 nm.

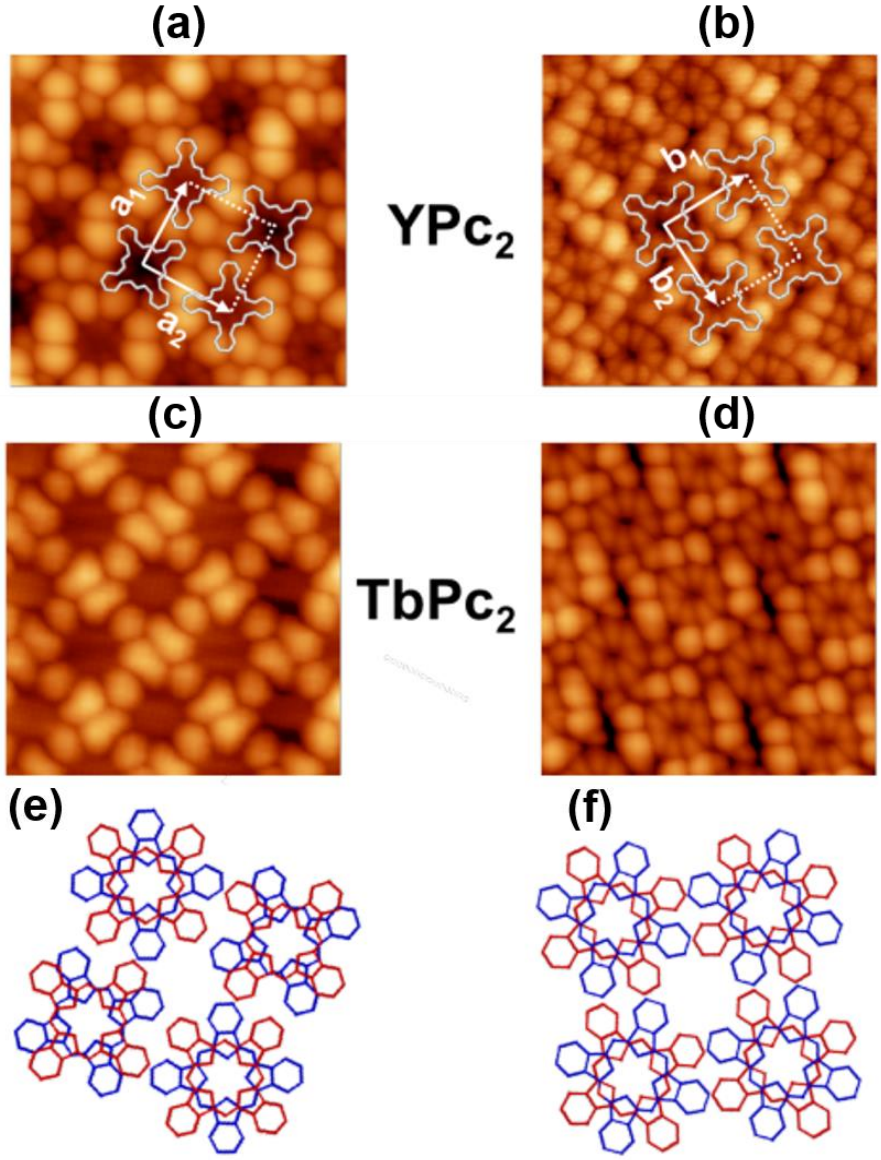

Fig. 3.3: STM images of molecular layers on Au(111) showing the two arrangement phases $TbPc_2$ and YPc_2 molecules in the molecular domain. (a) and (c) Phase I, image (5 nm x 5 nm) recorded at I_T = 90 pA and V_S = -0.8 V. (b) and (d) Phase II, image (5 nm x 5 nm) recorded at I_T = 90 pA and V_S = -1 V. Schematic models for the unit cells showing the upper Pc's (Blue) and bottom Pc's (red) for (e) Phase I and (f) Phase II.

A notable difference has been observed between the molecule belonging to the domain that has Phase I and these molecules belonging to the domain that has Phase II, which correspond to strongly interacting and weakly interacting neighboring molecules. The strongly

interacting domains (Phase I) involve overlapping of molecular orbitals of the upper Pc ligand (four lobes out of eight) of neighboring molecules whereas in the weakly interacting ones, Phase II, the molecules are arranged side by side (no overlap). The domains are characterized by square unit cells as illustrated in Figures 3.3 (c) and (d). Figures 3.3 (a) and (b) show simultaneously the superimposed crystallographic models with their unit cells corresponding to Phase I and Phase II for $TbPc_2$ or YPc_2. The square network of Phase I in Figure 3.3 (a) is characterized by the unit cell vectors $a_1 = a_2 = 1.43 \pm 0.06$ nm whereas the square network of the Phase II in Figure 3.3 (b) is characterized by the unit cell vectors $b_1 = b_2 = 1.50 \pm 0.06$ nm. As a result, the density of molecules is higher in Phase I than in Phase II, namely 0.49 nm^{-2} compared to 0.44 nm^{-2}, in full consistency with the fact that due to the orbital overlap, Phase I is more compact than Phase II.

Based on the assumption that all lower Pc-ligands of the films must have the same crystallographic orientation on Au(111) [12], two molecular models that are compatible with the experimental findings for Phase I and II are shown in Figure 3.3 (e) and (f) respectively. In Phase I, the upper Pcs have an alternate checkerboard configuration rotated by 45° and 30° with respect to the lower Pcs, whereas in Phase II, all the molecules have the same orientation and adopt an azimuthal angle of 45° between upper and lower Pc. A remarkable fact is that the molecules in Phase II show eight inner lobes that are clearly visible in Figure 3.3 (b) that are not resolved for the molecules of Phase I that only show their eight outer lobes. The fact that inner lobes are usually only imaged properly in isolated $TbPc_2$ molecule on Au(111) confirms the weak interaction between molecules in Phase II.

3.3 $TbPc_2$ growth on Ag(111)

Very few experiments have been done on the $TbPc_2$ adsorption on Ag(111). In this part, we have carried out a completed study on the $TbPc_2$ / Ag(111) system in order to evaluate the role of the substrate in the molecular arrangement geometry in first and second layer.

The STM images in the Figures 3.4 (a) and (b) show two Phases of $TbPc_2$ self-assemblies on Ag(111). In Phase I (same arrangement observed in paragraph 3.2, Phase I of TbPc2 on Au(111)), the molecules interact with each other by their upper Pc ligand, and the overlap interactions are thus observable on the 4 lobes (among 8) of each molecule with those of the neighboring molecules. On the other hand, in Phase II, we note a weak intermolecular interaction where molecules are adsorbed side by side. In this configuration, the molecules of the domain are crystallographically oriented in a different way. Indeed, each one is oriented

with a rotation of 30° with respect to the next neighboring molecule. Lattice parameters of the two Phases presented in Figures 3.4 (a) and (b) depict a unit cell containing two neighboring molecules with the following parameters $a_1 = a_2 = 1.8 \pm 0.08$ nm (Phase I) and $b_1 = b_2 = 2.2 \pm 0.08$ nm.

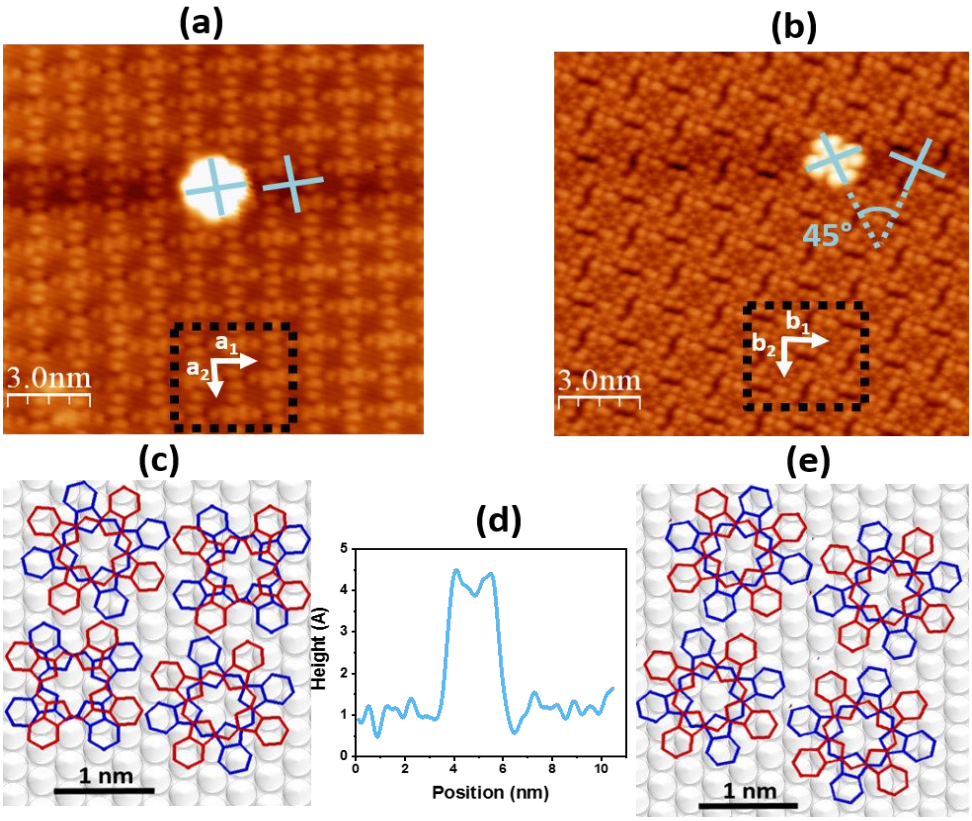

Fig. 3.4: Two types of $TbPc_2$ domains on Ag(111), where the molecules interacted within two arrangement phases: (a) Phase I and (b) Phase II. The two cyan crosses in (a) and (b) indicate that the upper Pc ligand of the $TbPc_2$ molecule in the second layer forms an angle of 0° and 45° with respect to its counterpart in the first layer in the two molecular Phases I and II respectively. The inset marked by dashed black line shows the unit cells parameters of two molecular phases: $a_1 = a_2 = 1.8 \pm 0.08$ nm (Phase I), $b_1 = b_2 = 2.2 \pm 0.08$ nm (Phase II). (c) and (e) Schematic models for the unit cells showing the upper Pc's (Blue) and bottom Pc's (red) for (a) Phase I and (b) Phase II. (d) Apparent height of the $TbPc_2$ molecule in second layer.

As previously emphasized by [13-15], the $LnPc_2$ molecule is adsorbed parallel to the first layer by forming a parallel π-π stacking between the upper Pc ligand of the molecule in the first layer and the lower Pc Ligand of the molecule in second layer. In our case, as exhibited in the STM images (Figure 3.4) by the cyan crosses, the $TbPc_2$ molecule in the second layer is rotated by 0° (Phase I) and 45° (Phase II) with respect to the one below. The apparent height of the

adsorbed molecule in second layer is of the order of 0.35 nm, which is comparable to that measured (0.3 nm) on isolated molecule directly adsorbed on Ag(111) [15]. Due to the fact that this molecule is easily manipulated by the tip of the STM, we can confirm that this corresponds to second layer of $TbPc_2$ molecules and not to Tb_2Pc_3 triple-deckers [16].

3.4 $TbPc_2$ growth on Cu(111)

3.4.1 Isolated molecule

The $TbPc_2$ molecule exhibits high stability when adsorbed on Cu(111) which is not the case on other substrates like Au(111) and Ag(111). Consequently, the distribution of these molecules on the surface is influenced by an attractive molecule-substrate interaction [17], allowing a preferential crystallographic orientation as shown in the Figure 3.5 (a). The superposition of two-dimensional lattice (green circles) suggests that the $TbPc_2$ molecular axis are aligned along the $[\bar{1}10]$ and $[\bar{1}\bar{1}2]$ directions of the Cu(111) surface. The size of the molecule is about 2 nm and its apparent adsorption height is 2.5 Å.

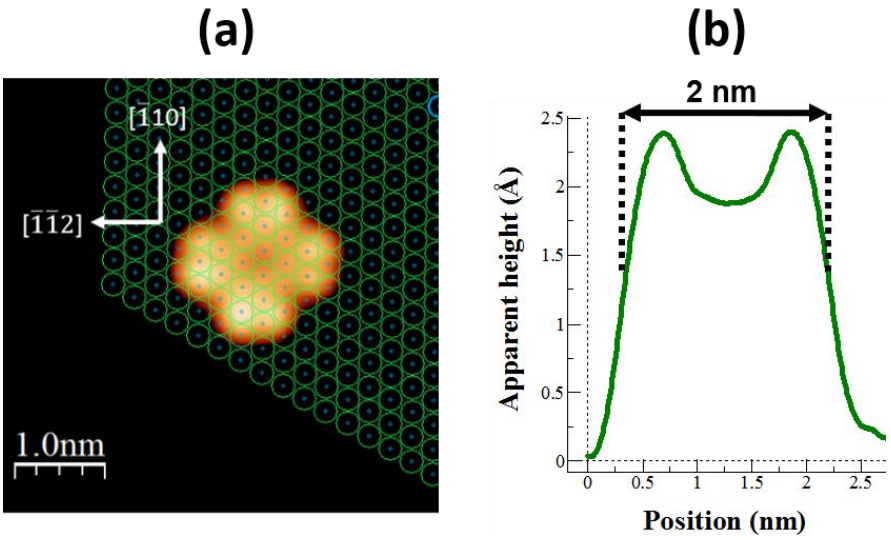

Fig. 3.5: (a) STM topographic image of an individual $TbPc_2$ on Cu(111) obtained at (V_S= 0.7, I_T= 20 nA), the molecular axes are aligned with the high symmetry and directions of the Cu(111). (b) Apparent height of the individual $TbPc_2$ molecule adsorbed on Cu(111).

3.4.2 Self-assembling domain

To better understand the interactions involved, these molecules have been studied at higher coverage after evaporation at room temperature. Up to one monolayer, in the molecular network observed in Figure 3.6, the molecules are not oriented in a single direction on the

Cu(111) crystal, but in two different directions forming various angles of 25 ° and 35 ° with respect to the lattice direction of [1$\bar{1}$0]. This network seems to be formed by molecular rows where molecules have alternance orientation along C_1 and C_2. However, in this topographic conformation each molecule has the 8 outer lobes as well as the inner lobes characterizing the orbitals of the higher Pc ligand of the molecule.

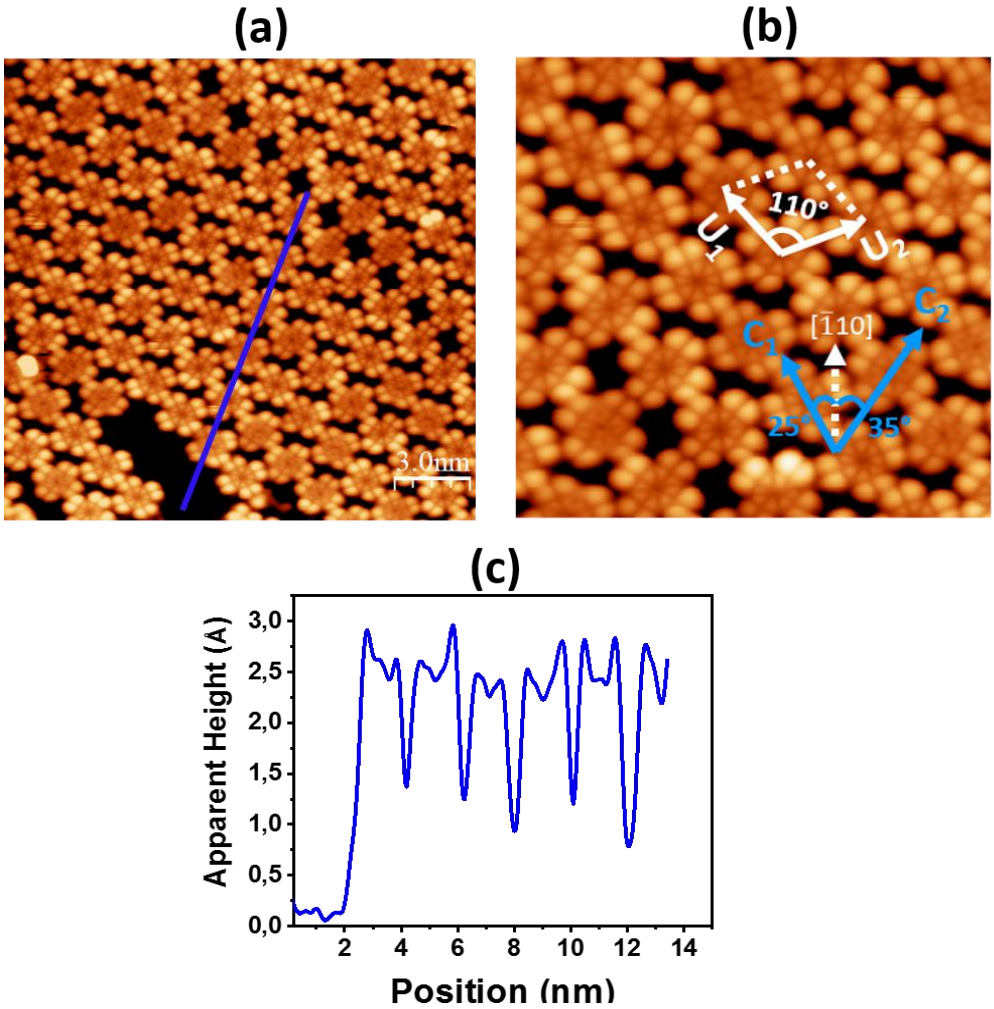

Fig. 3.6: (a) STM topographic images (V_S= -0.9 V, I_T= 30 pA) of $TbPc_2$ growth on Cu(111). The blue line shows the adsorption profile of molecular domain growth. (b) STM topographic image of molecular domain shows the adsorption direction of $TbPc_2$ molecules with respect of crystallographic direction of Cu(111) substrate. (c) Apparent height of Molecular domain.

The cell of the molecular lattice is characterized by the diamond shape, it is represented by two vectors U_1 and U_2 in Figure 3.6 (b) of equal standards of 1.82 ± 0.12 nm. This value is very close to the maximum distance between two extreme carbon atoms in the individual molecule adsorbed on Cu(111). In addition, the adsorption height of a molecular domain (2 Å) is comparable to that measured on the individual molecule. From this topographic information,

we can suggest that the topographic behavior of the molecule in a domain is similar to that of the molecule individually adsorbed on the surface of Cu(111). Therefore, we can consider that the molecule-substrate interactions are the most dominant one.

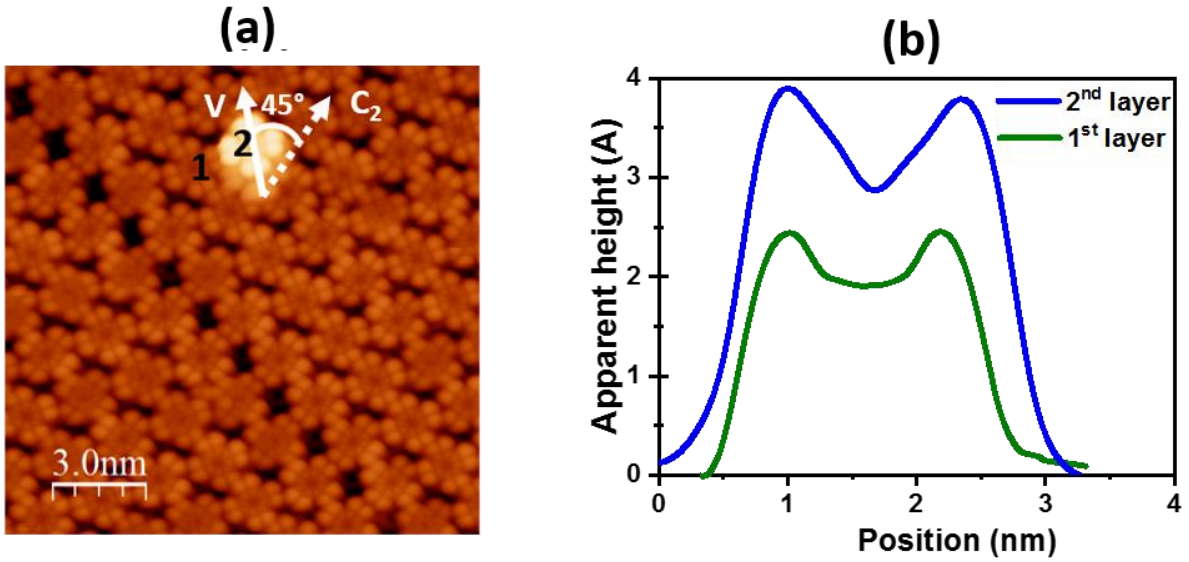

Fig. 3.7: STM topographic image of $TbPc_2$ monolayer grown on Cu(111) shows as well the adsorption of molecule 2 (2^{nd} layer) and its orientation with respect to the 1^{st} layer. (b) Molecular profiles measured along two opposite lobes. 3.5 Å are measured from the bottom layer to the upper ligand of the second layer shown in blue curve, a comparison of 1.5 Å with the molecular height (2 Å) of the first layer molecule is shown by green curve.

Second layer molecules, labeled 2 in Figure 3.7 (a), have been investigated. As well and as before, they have been moved by manipulation with the tip, to ensure that no triple-decker is involved. We can suggest that this case presents an intact double-decker molecule adsorbed in second layer by forming a parallel π-π stacking with the molecule bellow with a rotation angle of 45°. Second layer molecules also show eight lobes under STM imaging. As expected, due to the first layer decoupling, the second layer $TbPc_2$ shows an increased height, see the profile of Figure 3.7 (b). The height of the second layer molecule is measured to be 3.5 Å, this value is by 1.5 Å higher compared to isolated molecule (2 Å) directly adsorbed on Cu(111).

3.5 Conclusion

In this chapter, we have studied the structure and molecular geometries of self-assembled $TbPc_2$ molecules on Au(111), Ag(111) and Cu(111) surfaces and YPc_2 molecules on Au(111).

We have shown the Phases of molecular arrangement of $TbPc_2$ and YPc_2 molecules on different substrates (Au(111), Ag(111) and Cu(111)) as well as the detailed influence of intermolecular interactions (lateral interaction) in each Phase on the modification of the network parameters (unit-cell and molecular density). Then, the adsorption of $TbPc_2$ in the second layer on Ag(111) and Cu(111) was reported in this chapter to identify its adsorption geometry and its crystallographic direction relative to the substrate.

REFERENCES

[1] M. Ruben. Self-assembly of supramolecular nanostructures: ordered arrays of metal ions and carbon nanotubes. *Nanoscale and Bio-Inspired Computing* .Chapter 12. (2009)

[2] U.Schlickum, R. Decker, F. Klappenberger, G.Zoppellaro, S. Klyatskaya, W. Auwarter, S. Neppl, K. Kern, H. Brune, M. Ruben and J.V. Barth. Chiral Kagomé Lattice from Simple Ditopic Molecular Bricks. J. Am. Chem. Soc. 130, 11778-11782. 2008

[3] D. Ku¨hne, F. Klappenberger, R. Decker, U. Schlickum, H. Brune, S. Klyatskaya, M. Ruben and J. V. Barth, J. Phys. Chem. C, 2009, 113, 17851–17859.

[4] K. Katoh, Y. Yoshida, M. Yamashita, H. Miyasaka, B-K. Breedlove, T. Kajiwara, S. Takaishi, N. Ishikawa, H. Isshiki, Y-F. Zhang, T. Komeda, M. Yamagishi, and J. Takeya. Direct Observation of Lanth nide(III)-Phthalocyanine Molecules on Au(111) by Using Scanning Tunneling Microscopy and Scanning Tunneling Spectroscopy and Thin-Film Field-Effect Transistor Properties of Tb(III)- and Dy(III)-Phthalocyanine Molecules. *Journal of the American Chemical Society*, 131, 9967. (2009)

[5] T. Komeda, H. Isshiki, J. Liu, Y-F Zhang, N. Lorente, K. Katoh, B-K. Breedlove, and M. Yamashita. Observation and electric current control of a local spin in a single-molecule magnet. *Nature Communications*, 2, 217. (2011).

[6] L. Vitali, S. Fabris, A-M. Conte, S. Brink, M. Ruben, S. Baroni, and K. Kern. Electronic Structure of Surface-supported Bis(phthalocyaninato) Terbium(III) Single Molecular Magnets. *Nano Letters* 8:3364. (2008).

[7] J. Schwöbel, Y. Fu, J. Brede, A. Dilullo, G. Hoffmann, S. Klyatskaya, M. Ruben, and R. Wiesendanger. Real-space observation of spin-split molecular orbitals of adsorbed single-molecule magnets. *Nature Communications*, 3:953. (2012).

[8] F. Branzoli, P. Carretta, M. Filibian, M. Graf, S. Klyatskaya, M. Ruben, F. Coneri, and P. Dhakal, *Physical Review B* 82, 134401 (2010).

[9] A. Amokrane, S. Klyatskaya, M. Boero, M. Ruben and J-P. Bucher. The Role of π-Radicals in the Spin Connectivity of Clusters and Networks of Tb Double-Decker Single Molecule Magnets, *American Chemical Society* Nano 11, 10750-10760, (2017).

[10] Y. Zhang, H. Isshiki, K. Katoh, Y. Yoshida, M. Yamashita, M. Hitoshi, B. Breedlove, T. Kajiwara, S. Takaishi and T. Komeda, Low-Temperature Scanning Tunneling Microscopy Investigation of Bis(phthalocyaninato)Yttrium Grown on Au(111): From Individual Molecules to Two-Dimensional Domains. *Journal of Physical Chemistry C* 113, 9826–9830, (2009).

[11] Zhang, Y.; Guan, P.; Isshiki, H.; Chen, M.; Yamashita, M.; Komeda, T. Bis (phthalocyaninato) yttrium Grown on Au(111): Electronic Structure of a Single Molecule and the 31 Stability of Two-dimensional Films Investigated by Scanning Tunneling Microscopy/ Spectroscopy at 4.8 K, Nano Res. 2010, 3, 604–611.

[12] F. Ara, Z.K. Qi, J. Hou, T. Komeda, K. Katoha, M.Yamashita. A Scanning Tunneling Microscopy Study of the Electronic and Spin States of Bis (phthalocyaninato) terbium(III) ($TbPc_2$) Molecules on Ag(111). Dalton Transactions 45, 16644-16652, (2016).

[13] M. Toader, M. Knupfer, R. Dietrich, T. Zahn, M. Hietschold, Initial Growth of Lutetium(III) Bis-phthalocyanine on Ag(111) Surface. *Journal American Chemical Society*, 133, 5538–5544. (2011)

[14] Y. He, Y. Zhang, I.-P. Hong, F. Cheng, X. Zhou, Q. Shen and K. Wu, Low-temperature scanning tunneling microscopy study of double-decker DyPc2 on Pb Surface. *Nanoscale*, 6, 10779-10783, (2014).

[15] Anis Amokrane Thesis "Tunneling spectroscopy of mono- and di-nuclear organometallic molecules on surfaces" tel-01580023. (2016).

[16] J. Hellerstedt, A. Cahlík, M. Švec, B. de la Torre,; M. Moro-Lagares, T. Chutora, B. Papoušková, G. Zoppellaro, P. Mutombo, M. Ruben, R. Zbořil and P. Jelinek, On-surface structural and electronic properties of spontaneously formed Tb_2Pc_3 single molecule magnets. *Nanoscale* ,33, 15553-15563. 2018

[17] B. Warner, F. El Hallak, N. Atodiresei, P. Seibt, H. Prüser, V. Caciuc, M. Waters, A. J. Fisher, S. Blügel, J. Slageren and S. Hirjibehedin, Sub-Molecular Modulation of a 4f Driven Kondo Resonance by Surface Induced Asymmetry. Nature Communication, 7, 12785, (2016).

CHAPTER 4

Kondo issue in lanthanide double-decker molecular magnets on metal surfaces with ligand and 4f electron contributions

4.1 Introduction

In this chapter, we consider the adsorption of the $TbPc_2$ molecule on Au(111), Ag(111) and Cu(111) surfaces in order to study the Kondo effect at the molecule by STS. After describing the $TbPc_2$ molecular configuration on different substrates, we will address the HOMO and LUMO states of the molecule according to the nature of the substrate and focus on the observation of the Kondo effect by STS. Finally, we will discuss the origin of this effect and its dependence on the degree of interaction (weak to strong) with the substrate.

4.2 TbPc2 on Au(111)

4.2.1 HOMO and LUMO states

To better understand the electronic structure of the terbium double-decker molecule, we have performed multiple spectroscopic measurements on the molecule adsorbed on the surface of Au(111). We analyze the electronic structure of the self-organized molecule in Phase I as well as in Phase II (presented in section 3.2, chapter 3) to show the influence of intermolecular interaction on the position of the HOMO and LUMO states of $TbPc_2$.

In order to determine the HOMO and LUMO states of $TbPc_2$ adsorbed on Au(111), we have recorded dI/dV spectra over a ± 1 voltage range. These spectra are recorded with a tungsten tip positioned on the ligand and the center of the molecule in the two molecular domains I and II (shown in the Figures 4.1 (e) and (f)). As reported by Amokrane et al. in their works [1], the π-radicals can be described by considering the distribution of lobes from the STM image either

overlapping or dangling. In Phase I, as represented in the simplified diagram of Figure 4.1 (c), we observe that the two lobes overlap (red spot) and dangling (blue spot) in the same molecule which is due to the intermolecular interaction with the neighboring molecules. On the other hand, in Phase II (Figure 4.1(d)), all the lobes are dangling due to the absence of intermolecular interaction between neighboring molecules.

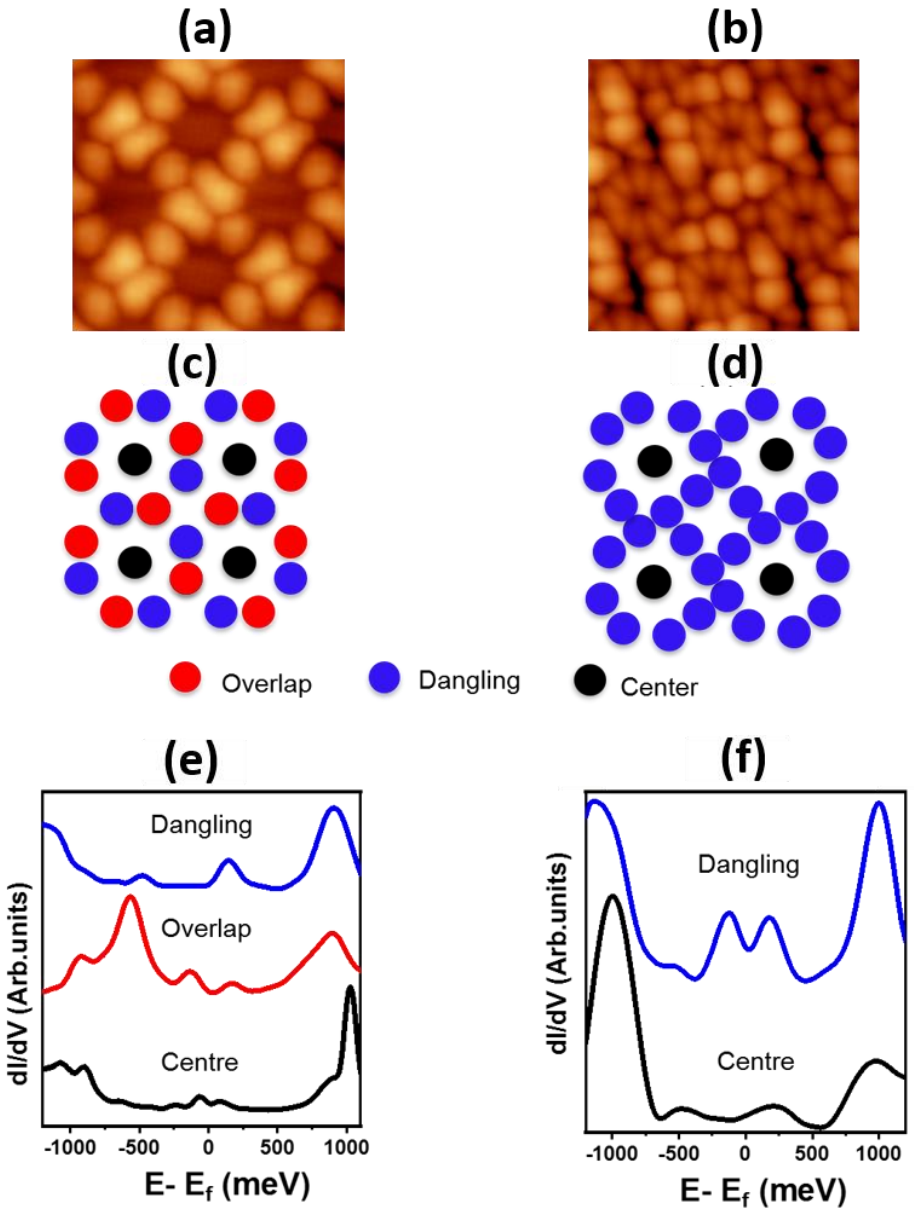

Fig. 4.1: (a) and (b) STM images of 4 adjacent $TbPc_2$ molecules self-assembled onto two phases I and II respectively. (c) and (d) Schematics representations of the unit cells showing the location above the molecules where the dI/dV have been recorded on Phase I and Phase II respectively. (e) and (f) dI/dV spectra recorded above the blue, red and black spots in $TbPc_2$ network. Set point parameters: V_S = -0.4 V, I_T = 100 pA and modulation voltage: 30 mV (pp). T= 4.6 K.

Comparing the two Figures 4.1 (e) and (f), we find that the STS spectra recorded on the center and on the lobes (dangling and overlap) show a difference between HOMO-LUMO gap (defined by the difference between the energies of the two peaks near the Fermi level) of the molecule in Phase I and that in Phase II. This is clearly observable on blue spectra where the difference is of the order of 350 meV: the gap of the molecule in Phase I is 650 meV and in Phase II is 300 meV. However, this difference reflects the influence of the interaction of the molecule with the substrate, ie, the structure of the self-arrangement of molecules in Phase I is more stable than that in Phase II. Furthermore, this phenomenon is observable by comparing the black spectra, where we note a difference of 550 meV at the center of the molecules in Phase I (gap = 200 meV) and in Phase II (gap = 750 meV). As a result, we can conclude that the lateral interactions induces a modification of the energy states (HOMO and LUMO states) of the central Tb-atom, and this is mainly due to the interaction between 4f-electrons and the π-electrons in $TbPc_2$.

4.2.2 Kondo effect

In this part, we are interested in the detection of the Kondo effect by STS. The Figure 4.2 shows the dI/dV spectra for energies very close to the Fermi level recorded above two molecules of $TbPc_2$ self-assembled on Au(111) within Phase II. The obtained spectra clearly show a resonance, the peak shape as well as its position suggests the presence of a Kondo effect. We observe a peak when the tip is located on both, the inner and outer lobes of the molecule. In contrast, the peak disappears when the tip is positioned on the center of the molecule. Thus, the observed peaks probably originate from the unpaired π-radical spin existing in the Pc ligand of $TbPc_2$ molecule [1-3], more particularly, on the inner and outer lobes.

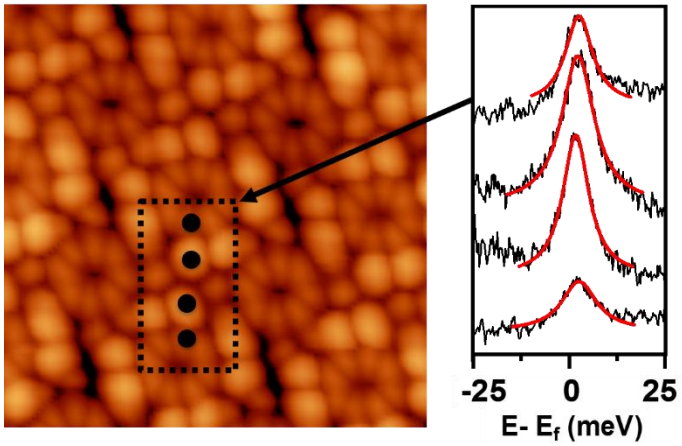

Fig. 4.2: Topographic STM image of $TbPc_2$ films with Phase II showing the places (marked by black circles) where spectroscopy was performed on inner & outer lobes of two adjacent

molecules. Inset: the Kondo resonances above the areas shown in the topography image. Data acquired with a modulation voltage of 5 mV (pp), at T = 4.6 K, fitted by a Fano function (red line).

The shape of the zero-bias peaks observed at the Fermi level have been fitted by the Fano function [4] (red curve): With

$$\varepsilon = \frac{eV - E_0}{\Gamma} \qquad (4.1)$$

where E_0 and Γ are the position and temperature-dependent half-width at half-maximum of the Kondo feature and q is the ratio of tunneling into the resonance and into the continuum. The width of the peaks is determined as $\Gamma = 8.55 \pm 0.24$ meV. This value can be used in Equation (4.2) [5] to calculate the Kondo temperature:

$$\Gamma(T) = \sqrt{(3.5K_BT)^2 + (\sqrt{6}eV_{rms})^2 + 2(k_BT_K)^2} \qquad (4.2)$$

The Kondo temperature obtained for $TbPc_2$ is $T_K = 41$ K. The same Kondo temperature obtained for inner and outer lobes within experimental errors, emphasizing that inner and outer lobes belong to the same π-radical. The fact that $q = 1.17 \pm 0.02$ meV shows that there is a roughly equal tunneling into the spin center and into the continuum [6], which is relevant for the weak interaction of the upper Pc ligand with the substrate. As will be shown in the following this situation is quite different from the strong interaction case of $TbPc_2$ /Cu(111), where the direct tunneling into the spin center becomes dominant.

4.3 Local spectroscopy on $TbPc_2$ in comparison with YPc_2

In order to investigate the interaction between π- and f-electrons in lanthanide double decker molecules deposited on Au(111), we have simultaneously studied the structural and electronic properties of YPc_2 on the Au(111) by LT-STM/STS. Regarding the electronic structure, the Yttrium ion (Y^{3+}) is very close to that the lanthanide ion, and this ion is only spectator in the radical-radical interactions involved in the mechanisms responsible for magnetic coupling. $TbPc_2$ is the most interesting of the two molecules because of its single molecule magnet behavior due to f-electrons, however YPc_2 provides an interesting system to compare with since the Y^{3+} ion has an empty 4d- and 4f-electron shell. It is therefore possible to evaluate the role of the π-electrons in the electronic interaction among molecules, and to find out to which extent they impact on the f-electrons.

In the paragraph 4.2.1, we have seen that the intermolecular interactions (lateral interactions) induce a modification of the energy states of the central atom Tb evidenced by STS measurements carried out on the center of the $TbPc_2$ molecule in the two Phases I and II. To exclude this hypothesis, we consider phase II of the $TbPc_2$ and YPc_2 self-assemblies on Au(111) to limit the interactions within the molecule (intramolecular interaction) and consequently the incidence of f-electrons on the π-electrons ligand Pc. In this sense, we performed dI/dV measurements on the Pc ligand as well as on the center of the $TbPc_2$ and YPc_2 presented in the Figure 4.3.

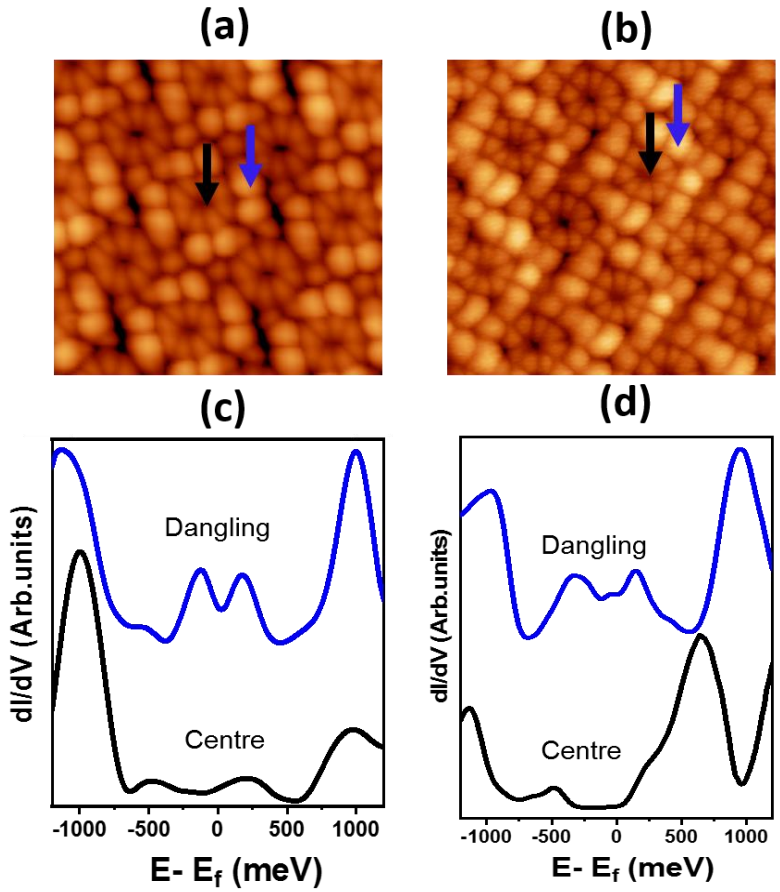

Fig. 4.3: (a) and (b) High resolution STM images (5 × 5 nm^2) of the Phase II of $TbPc_2$ and YPc_2 molecular domains growth on Au(111), respectively. Blue and black arrows indicate the point where the spectra dI/dV was recorded. (c) and (d) dI/dV spectroscopy from -1.2 eV to + 1.2 eV on the center and the dangling lobe of the two molecules $TbPc_2$ and YPc_2 as shown in (a) and (b) respectively.

By way of comparison, the blue spectra in Figures 4.3 (c) and (d) (recorded on the Pc ligand) are similar, namely that the HOMO and LUMO peaks energy positions are at -200 meV and +200 meV respectively. Yet, on the centers (black spectra Figures 4.3 (c) and (d)), we note

a displacement in energy of the LUMO orbital of +250 in the central area of the $TbPc_2$ molecule (Figure 4.3 (c)) and of +600 in the central area of YPc_2 (Figure 4.3 (d)). In this way, the differences appear only on the center of the molecule, which is reasonable, since Tb^{3+} bearing 4f-electrons and empty-electron ions such as Y^{3+}. By comparing the measurements recorded on the Pc ligand in both cases ($TbPc_2$ and YPc_2), we can conclude that the f-electrons have no contribution on π-electrons of the Pc ligand in the $TbPc_2$ molecule.

We have demonstrated an additional Kondo measurement on the Pc ligand of the two systems $TbPc_2$ / Au(111) and YPc_2 / Au(111). However, it has been reported that the Kondo effect is a signature of the presence of an unpaired π-electron located on the $TbPc_2$ ligand Pc and that this appearance is highly sensitive to the molecular configuration of self-assembly [1]. In the case where the molecules interact weakly, Phase II, we show in this configuration that a Kondo peak appears on all the lobes of the molecule $TbPc_2$ as well as on the molecule YPc_2.

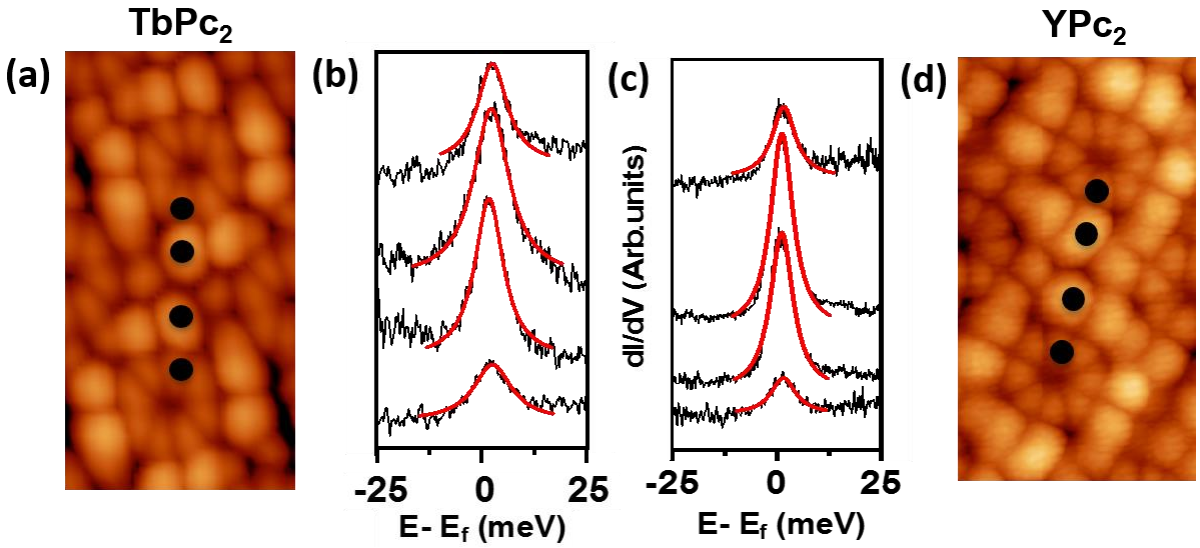

Fig. 4.4: (a) and (d) Topographic images STM of YPc_2 and $TbPc_2$ films within Phase II, showing the places (black circles) where spectroscopic data were performed on inner and outer lobes. (b) and (c) the Kondo resonances above the areas shown in the topography image in (a) and (d). data acquired with a modulation voltage of 5 mV (pp), at 4.6K, fitted by Fano function (red line).

The Figure 4.4 shows recorded Kondo peaks when the tip is located on the inner and outer lobes of the $TbPc_2$ molecule as well as on the YPc_2 molecule. The most probable origin of this appearance is the presence of an unpaired excessed electron delocalized on π-orbital of Pc ligand. Referring to the relationship (4.2), the Kondo temperatures obtained for YPc_2 and $TbPc_2$

are T_K = 29 K and T_K = 41 K respectively. The molecular configuration of the double decker molecules has no impact on the modification of the Kondo temperature (unlike Phase I reported by Amokrane et al. [1]), the values are close to that of isolated $TbPc_2$ molecule (38K). Therefore, we can conclude that the π-radical is still present at the Pc ligand of two molecules $TbPc_2$ and YPc_2. Moreover, according to the spectroscopic measurements, we demonstrate the weak contribution of the f-electrons on the π-electrons in the $TbPc_2$ molecule.

4.4 $TbPc_2$ on Ag(111)

Very few experiments have been done on the $TbPc_2$ adsorption on Ag(111) [7,8].Therefore in this part, we have carried out a completed study on the $TbPc_2$ / Ag(111) system in order to evaluate the role of the substrate on the appearance of the π-radical of the molecule at the first and second layer.

4.4.1 HOMO and LUMO states

The Au(111) substrate is rather inert towards the $TbPc_2$ molecule and therefore the π-radical of the molecule remains intact upon adsorption on the surface. For sake of comparison, we also use the more reactive Ag(111) substrate and take advantage of the adsorption induced charge-transfer [7,8] to get a deeper insight into the single-molecule properties and molecule-molecule interaction. Adsorption induced charging, leading to $[TbPc_2]^-$, may quench the ligand spin. The charge transfer occurring from the Ag(111) substrate to the $TbPc_2$ molecules in the first monolayer has recently been confirmed by a total energy DFT calculation [8].

Figure 4.5 shows the dI/dV spectra recorded in both molecular Phases (I and II), above the ligands of first- and second-layer $TbPc_2$ molecules on Ag(111), corresponding to green and blue spectra, respectively. In Phase II, the green spectrum in Figure 4.5 (a) shows pronounced peaks at -700 meV and +600 meV consistent with those mentioned previously [8] and have been ascribed to the HOMO and LUMO orbitals thus leading to a gap of 1.3 eV. However, in Phase I, the overlapping interaction between the ligands induces an energy shift of the HOMO orbital towards the Fermi level, thus leading to the new gap of 1 eV. In both molecular Phases, the molecule in the second layer shows a HOMO peak that is shifted upwards by 450 meV compared to the green spectrum, leading to a narrowing of the HOMO - LUMO gap to about 750 meV, very close to the gap measured by Amokrane et al. on Au(111) [1]. The $TbPc_2$ molecule adsorbed in the second layer on Ag(111) thus behaves electronically very much like the molecule adsorbed directly on Au(111).

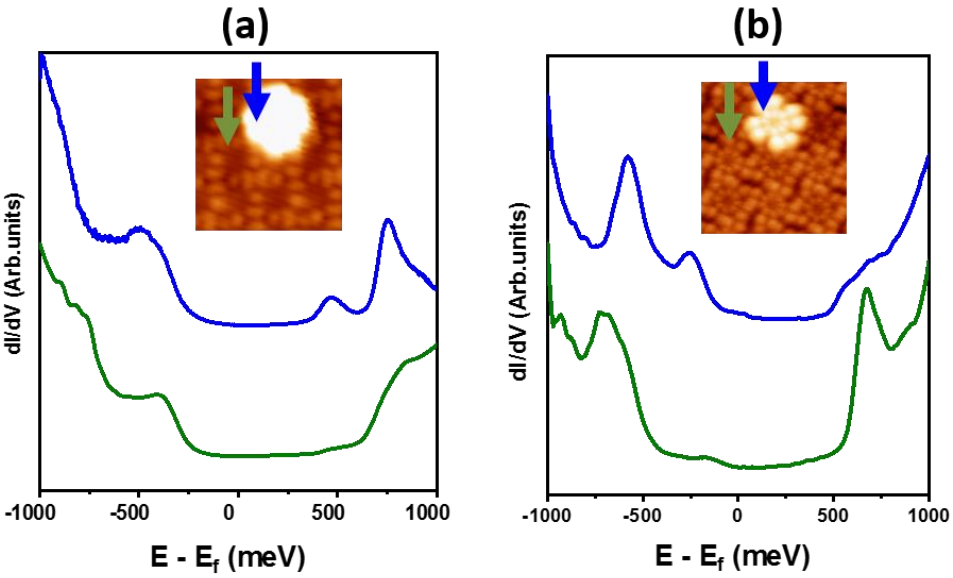

Fig. 4.5: dI/dV spectroscopy performed above the areas (Ligand) shown in the topography STM image (Inset) of Phase I (a) and Phase II (b), same color code. The spectra show a comparison between the HOMO/LUMO states of the $TbPc_2$ adsorbed of first- and second-layer.

4.4.2 Kondo effect

In this part, we have used Kondo spectroscopy over a range of energy ± 50 meV above the $TbPc_2$ ligand of first- and second-layer. The Figure 4.6 shows that a Kondo peak appears only on the molecule of the second layer. The origin is attributed to the unpaired electron located on π-orbital in the second layer. Referring to the works reposted by Ara et al. [7] and Hellerstedt et al. [8], a charge transfer occurring from the Ag(111) substrate to the first molecular layer can thus be considered as a decoupling layer due to the pairing-up of first layer radicals. However, the spin located on the ligand of the second layer is responsible for the appearance of the Kondo effect thus observed in the figure. As presented Figure 4.6 a, the substrate produces spins interacting with the delocalized electron of the ligand in first layer, thus killing the Kondo effect in this first layer. On the other hand, since the second layer molecule is decoupled from the surface, its π-radical remains intact leading to a Kondo peak in the second layer.

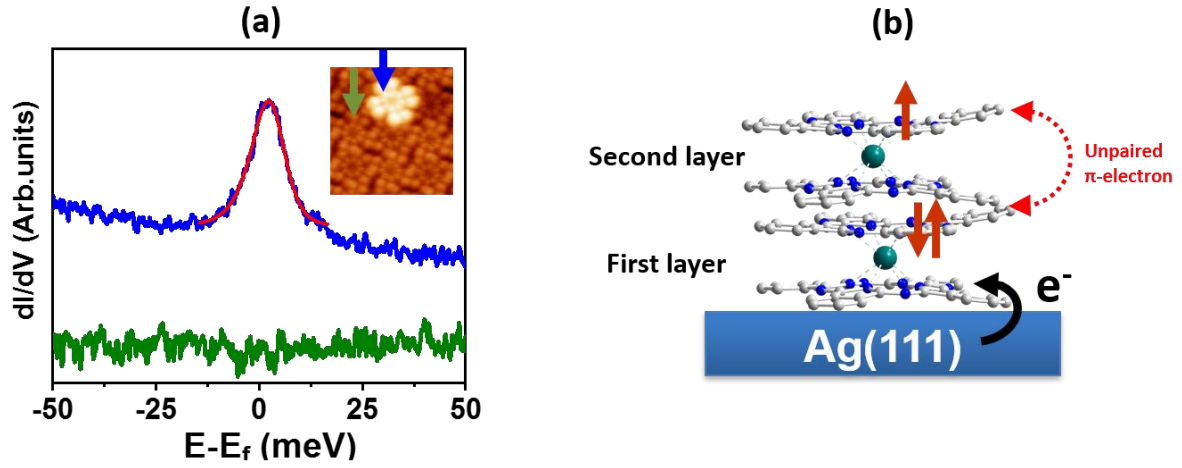

Fig. 4.6: (a) dI/dV spectra showing a Kondo resonance (blue line) on the ligand of the molecule in second layer, the peak disappears when the tip is positioned above first layer. (b) Basic schematics of $(TbPc_2)_2$ (first and second layer) show: The pairing of two electrons in the first layer caused by charge of the Ag(111) substrate, and the appearance of the delocalized electron in molecule of second layer resulting the Kondo resonance.

The shape of the resonance is similar to the previously measured Kondo resonance above the $TbPc_2$ grown on Au(111) (Phase II), which is well described by a Fano function Equ. (4.1). Accounting for thermal broadening and voltage modulation, this leads to a Kondo temperature of T_K = 42 K, compared to that measured on isolated $TbPc_2$ molecule.

4.5 $TbPc_2$ on Cu(111)

It has been shown that in single and double-decker molecules adsorbed on metallic surfaces (Au(111) and Ag(111)) the Kondo effect can be caused by an unpaired π-orbital of the ligand. Moreover, recently, 4f- driven Kondo resonance has been demonstrated by studying the $DyPc_2$/Cu (001) system by STM/STS measurements supported by DFT calculations [9]. Indeed, they showed a strong hybridization of the d- and f- orbitals of $DyPc_2$ molecule with the substrate. A Kondo screening was observed via the coupling between the 4f moment and the Cu conduction electrons bath. In the case of $TbPc_2$, the 3+ oxidation state results in one electron in the 4f orbital and one unpaired electron in a radical state. This could induce the detection of Kondo resonance on the ligand, located on the lobes of the molecule, as the case of $TbPc_2$/Au(111) [1,2]. It was not expected that a Kondo resonance would be detected on the center (Terbium ion) of the molecule adsorbed on Cu(111), Ag(111) or Au(111) substrate. We have demonstrated, in our works, that the Kondo resonance is located throughout the molecule (ligand and center), caused by the strong interaction molecule-substrate produced between

$TbPc_2$ and Cu(111). In contrast to the case of Ag(111), an electron transfer occurred between the Ag atoms and the molecule which causes the quench of the spin. On Cu(111), we suggest that a molecule-substrate hybridization via the 4f-orbitals is responsible for the appearance of Kondo resonance on the central site of the molecule.

4.5.1 Tunneling spectroscopy on isolated molecule

In order to explore the electronic states of the isolated $TbPc_2$ molecule adsorbed on Cu(111). we have recorded the dI/dV spectra with the STM tip positioned on the ligand and the center as shown in the Figure 4.7 (b). The spectra show a similar appearance with two apparent peaks, the first one located in the occupied region at around - 700 meV and the other at around + 700 meV, which could be assigned to HOMO and LUMO resonances respectively, yielding an apparent gap of about 1.4 eV. They are also present in the first layer $TbPc_2$ on Ag(111) (see Figure 4.5 (b) in paragraph 4.4.1) which may lead to the wrong conclusion that $TbPc_2$/Cu(111) and $TbPc_2$/Ag(111) show similar behavior. To analyze the spatial distribution of the electronic states more in detail, dI/dV maps were recorded above an isolated molecule. At -700 meV, the dI/dV map shows a conductance localization above the central Tb ion of the molecule (Figure 4.7 (e)), no conductance contribution from the upper Pc is observed at this energy. By contrast, at +700 eV, the empty states contribute an almost uniform conductance over the molecule (lobes and central area) as shown in Figure 4.7 (f).

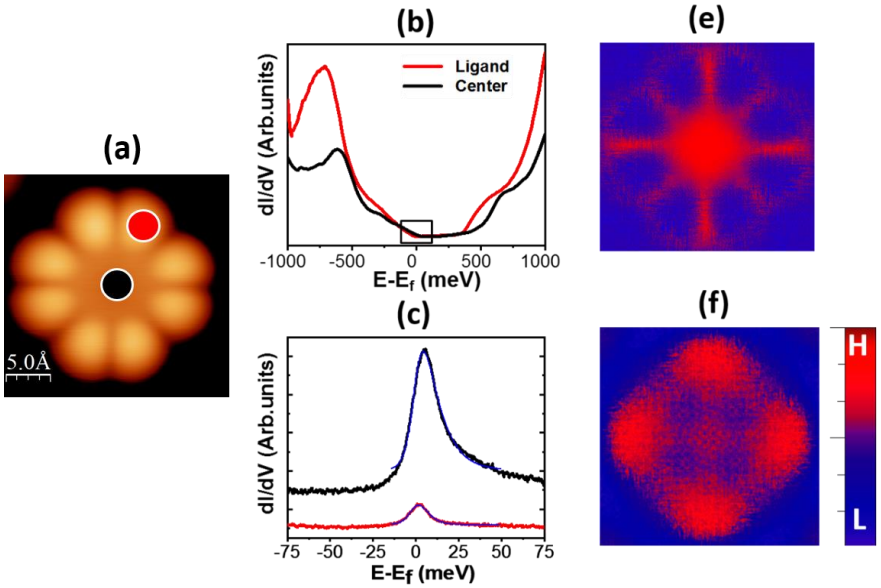

Fig. 4.7: (a) STM topographic image of an individual $TbPc_2$ on Cu(111) obtained at (V_S= 0.7, I_T= 20 nA), the molecular axes are aligned with the high symmetry and directions of the Cu(111). (b) dI/dV spectra measured at ligand (red) and center (black) sites of the molecule. **(c)**

The inset in (b) shows the Kondo peaks acquired above the ligand (red) and center (black) of the molecule with a modulation voltage of 5 mV (pp). (e) and (f) dI/dV maps in the bias of occupied states (-0.7 V) and unoccupied states (+0.7 V) respectively. Red: high conductance, blue: low conductance.

In addition, we focused in the detection of a Kondo resonance by STS. The Figure 4.7 (c) shows the dI/dV spectra within a range of -75 meV to 75 meV. A Kondo peak is observed when the tip is positioned at the center and over the rest of the molecule. Nevertheless, the molecule shows quite high and distinct Kondo temperatures of T_K = 97 K and T_K = 62 K for the center and the ligand respectively. Furthermore, the probability of electron tunneling into the Tb compared to the tunneling into the bulk continuum is increased significantly, as evidenced from the increase in the Fano factor from q = 1.8 on the ligand to q = 5.5 above the Tb ion. Remember that these two contributions (tunneling into spin and continuum) are roughly equal over the ligand for the weak interaction cases where $q \approx 1$. The significantly different Kondo temperature also speaks in favor of a different origin of spin centers, 4f-electrons on the one hand and ligand, π-electrons on the other. These results are quite different from those reported in the literature for $DyPc_2$ on Cu(100) where a constant T_K = 33 K was measured all over the molecule and $q \approx 1$ [9]. We therefore conclude that the screening is much more efficient for $TbPc_2$/Cu(111) due to the strong hybridization between the 4f orbitals of Tb and the itinerant *spd* electrons from the Cu(111) substrate via the lower Pc-ligand. This result also confirms that the molecule-substrate interaction is dominant for $TbPc_2$ on Cu(111) contrary to $TbPc_2$ on Au(111), which is dominated by the lateral interactions ruled by intermolecular orbital overlaps as shown above.

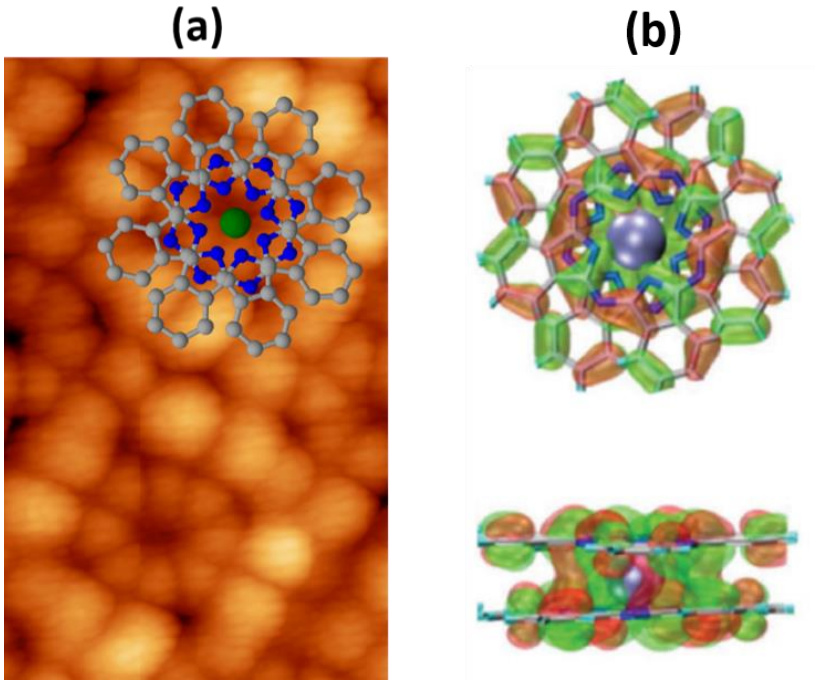

Fig. 4.8: (a) STM image of $TbPc_2$ domain on Au(111) with a superimposed atomic structure of $TbPc_2$, revealing the location of the orbital of each N,C and Tb atom in the STM topographic image. (b) DFT calculation of the wave function corresponding to a spin-up state at −0.5 eV evidencing the simultaneous contribution to inner and outer lobes. Red and green colors correspond to positive and negative signs of the wave function.

The fact that inner and outer lobes show the same Kondo temperature may suggest that both 'Kondo' lobes belong to one and the same spin center. We decided to investigate this aspect in more detail. The first principles calculations of free standing molecules within the DFT framework have proven to describe well the interaction among $TbPc_2$ molecules on Au(111). We therefore use the same approach here. As an example, Figure 4.8 (b) shows the wave function corresponding to a spin up state at −0.5 eV. This figure clearly shows that the same spin polarized wave function contributes to both inner and outer lobes. It is therefore not surprising that inner and outer lobes show the same screening, thus the same T_K.

Furthermore, our results show that the inner lobes are geometrically very close to the molecule's center and coincide with the location of the nitrogen atoms of the Pc ligands (Figure 4.8 a) . Since the spin polarized orbitals of the Pc's are the one associated with the spin radical it is clear that the radical is hybridized with the 4f Tb electrons. Together with the spectroscopic data discussed above, our experimental results therefore show additional evidence for the

hybridization of the 4f-electrons of Tb with the substrate through the lower Pc, as postulated on similar systems by means of DFT calculations [9].

4.5.2 Tunneling spectroscopy on molecular domain

The dI/dV spectroscopic measurements acquired above the center and the ligand of the $TbPc_2$ molecule of first- and second layer are shown in Figure 4.9 (b). The substrate interaction induces a significant modification in the electronic structure of the $TbPc_2$ molecule. In the case of molecule 1 (first layer), where it is in direct contact with copper substrate, the molecule belonging to a domain behaves as an individual molecule. As a matter of comparison, the HOMO and LUMO peaks positions are similar to one of the individual molecule (see Figure 4.7 (b)) above the ligand and center. However, when the molecule is decoupled from the substrate, which is the case of the molecule **2** (second layer), we observe a small shift of about 100 meV of the HOMO peak whereas the LUMO is rejected above 1 eV.

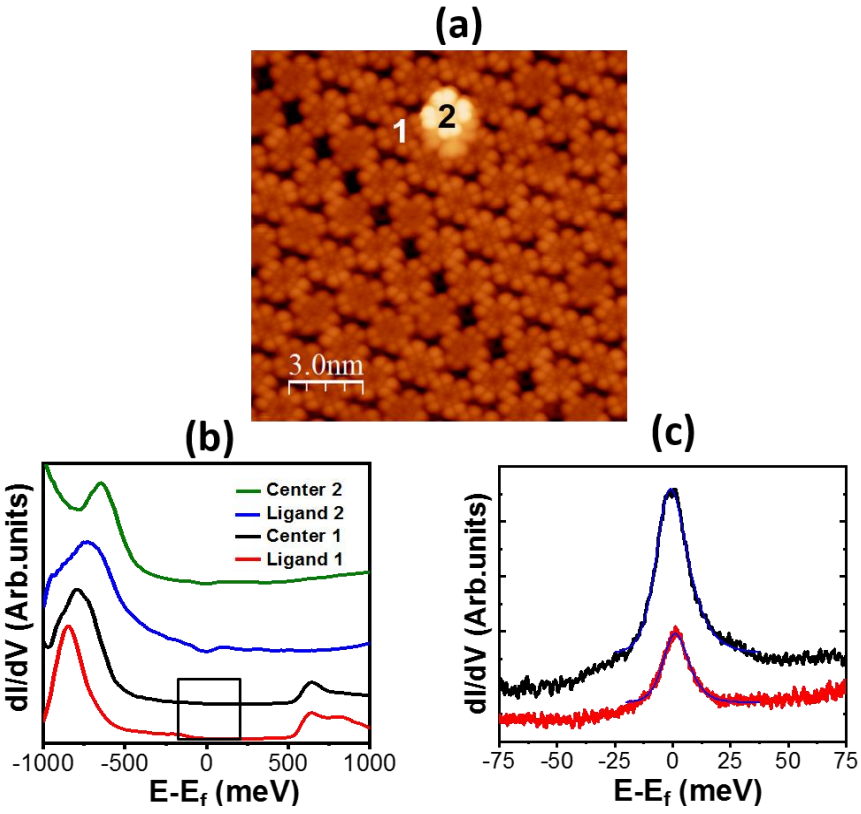

Fig. 4.9: (b) STM topographic image (V_S= -0.9 V, I_T= 30 pA) of $TbPc_2$ growth on Cu(111). (b) dI/dV spectra measured at molecule **1** (first layer) sites: Ligand (red) and center (black) and at the molecule **2** (second layer) sites: Ligand (blue) and center (green). (c) The inset in (b) shows the Kondo peaks acquired above the ligand (red) and center (black) of the molecule in the first layer with a modulation voltage of 5 mV (pp).

As in the case of the individual molecule, the Kondo resonance is present throughout the molecule **1** adsorbed in first layer. In contrast, it is quenched in molecule **2** (second layer). This can confirm that even in the case of the molecular domains of $TbPc_2$ only the substrate-molecule interaction is dominant, unlike the other substrates of Au(111) or Ag(111) where intermolecular overlap interactions cannot be neglected. Comparing the Kondo temperatures in both cases (individual molecule shown in Figure 4.7 (c) and molecule **1** inserted in a molecular domain shown in Figure 4.9 (c)), a small change of the Kondo temperature is observed however with T_K = 85 K and T_K = 68 K above the center and the ligand respectively. This difference may just result from the difficulty in finding exactly the same spot where to take the dI/dV. According to these results, we suggest that molecular spin-spin interaction between the first and second layer could be responsible for the disappearance of Kondo effect in the second layer.

4.6 Conclusion

Based on a good understanding of the self-organization phenomena of $TbPc_2$ molecules on the Ag(111), Au(111) and Cu(111) surfaces, we have been able to study local electronic properties for isolated molecules (only on Cu(111)) and within self-assemblies on the three substrates. Both occupied and unoccupied states of the $TbPc_2$ molecules have been identified. The conductance spectra allowed us to interpret the influence of the substrate nature on the modification of the frontier orbitals of the molecule.

Furthermore high-resolution tunneling spectroscopy measurements were conducted to study the appearance of the Kondo effect. This effect has been demonstrated for the molecules adsorbed on Au(111), Ag(111) (first and second layer) and on Cu(111) (first and second layer). The interpretation lies in the nature of the interaction of the molecule with the substrate leading to the contribution of π-radical in the appearance of Kondo resonance on the ligand (case of Au(111) and Ag(111)) and on the contribution of 4f-electrons in the appearance of Kondo resonance on the ligand and center of the molecule (case of Cu(111)).

REFERENCES

[1] A. Amokrane, S. Klyatskaya, M. Boero, M. Ruben and J-P. Bucher. The Role of π-Radicals in the Spin Connectivity of Clusters and Networks of Tb Double-Decker Single Molecule Magnets, *ACS* Nano 11, 10750-10760, (2017).

[2] T. Komeda, H. Isshiki, J. Liu ,Y. Zhang, N. Lorente, K. Katoh, B. Breedlove and M. Yamashita. Observation and electric current control of a local spin in a single-molecule magnet. *Nature Communication* 2, 217, (2011).

[3] Müllegger, S.; Tebi, S.; Das, A. K.; Schöfberger, W.; Fachinger, F.; Koch, R. Radiofrequency Scanning Tunneling Spectroscopy for Single-Molecule Spin Resonance. Phys. Rev. Lett. 2014, 113, 133001

[4] Fano, U. Effects of Configuration Interaction on Intensities and Phase Shifts. Phys. Rev. 1961, 124, 1866.

[5] Hellwig, R.; Paintner, T.; Chen, Z.; Ruben, M.; Seitsonen, A. P.; Klappenberger, F.; Brune, H.; Barth, J.V. Epitaxy-Induced Assembly and Enantiomeric Switching of an On-Surface Formed Dinuclear Organocobalt Complex. ACS Nano 2017, 11, 1347-1359.

[6] Ternes, M.; Heinrich, A. J.; Schneider, W. D. Spectroscopic manifestations of the Kondo effect on single adatoms. J. Phys. Condens. Matter 2009, 21, 053001.

[7] Ara, F.; Qi, Z. K.; Hou, J.; Komeda, T.; Katoha, K.; Yamashita, M. A Scanning Tunneling Microscopy Study of the Electronic and Spin States of Bis(phthalocyaninato) terbium(III) (TbPc2) Molecules on Ag(111). Dalton Trans. 2016, 45, 16644-16652

[8] Hellerstedt, J.; Cahlík, A.; Švec, M.; de la Torre, B.; Moro-Lagares, M.; Chutora, T.; Papoušková, B.; Zoppellaro, G.; Mutombo, P.; Ruben, M.; Zbořil, R.; Jelinek, P. On-surface structural and electronic properties of spontaneously formed Tb2Pc3 single molecule magnets. Nanoscale 2018, 33, 15553-15563

[9] B. Warner, F. El Hallak, N. Atodiresei, P. Seibt, H. Prüser, V. Caciuc, M. Waters, A. J. Fisher, S. Blügel, J. Slageren and S. Hirjibehedin, Sub-Molecular Modulation of a 4f Driven Kondo Resonance by Surface Induced Asymmetry. Nature Communication, 7, 12785, (2016).

CHAPTER 5

Positioning $TbPc_2$ on the cavities of $Co(NC\text{-}Ph_n\text{-}CN)_3$ metal-organic networks

5.1 Introduction

The self-assembly of molecular precursors assisted by a metallic surface has recently emerged as a new pathway for creating new promising molecular architectures for molecular electronics. As organic precursors, our choice fell on polyphenyl dicarbonitrile linkers (NC-Phn-CN (n = 3-6)) which are evaporated under ultra-high vacuum (UHV) on a metallic surface [1]. Their obtained self-assemblies have been widely studied by tunneling microscopy (STM). The design of molecular structures is based on non-covalent interactions (hydrogen bonding, metal-ligand interaction, Van der Waals interaction or electrostatic interaction) [2] with specific geometries that allow well-established hierarchical organization. After seeding the molecular layer (NC-Phn-CN self-assemblies (n = 3 to 6)) with cobalt atoms on the same surface, a spontaneous coordination interaction is produced leading to the formation of a metal-organic honeycomb network of $Co(NC\text{-}Ph_n\text{-}CN)_3$ [3,7,8].

The 2D coordination networks comprising hexagonal cavities can be used as templates for engineering the host-guest system. They can be specifically adapted to immobilize individual molecules or clusters whose size is adapted to that of the nanopore network. The implementation of a Host-Guest system [4] by a coordination network $Co(NC\text{-}Ph_n\text{-}CN)_3$ ensuring the role of host with SMM molecules ensuring the guest is a massive task. Experimentally, this will depend on a control of the evaporation temperature of organic precursor and a calibration of the amount of cobalt to be deposited to generate the coordination interaction. Upon deposition of SMM molecules an unsuspected modification of the original structure of the network can occur. The partial or total break of the coordination between the Co and the organic precursor $NC\text{-}Ph_n\text{-}CN$ may take place because of the chemical interactions between various atoms composing the host and the guest.

In the previous chapter, we have seen that when the SMM molecules of $TbPc_2$ are evaporated on one of the Au(111) and Ag(111) surfaces, they spontaneously form molecular domains of about 80 nm. A spectral study has been consequently revealed and shows that the dI/dV conductance recorded on the molecule (ligand and center) varies according to the nature of the substrate and the nature of the mutual interactions existing in the molecular network. In this chapter, in order to isolate an individual molecule (monomer) or clusters of molecules (dimer, trimer or tetramer), we decided to make metal-organic networks $Co(NC\text{-}Ph_n\text{-}CN)_3$ with hexagonal nanopores and adjustable periodicity. The pores will be exploited to locate and confine the SMM molecules of $TbPc_2$ as shown schematically in Figure 5.1 and ultimately to measure their electronic and magnetic properties.

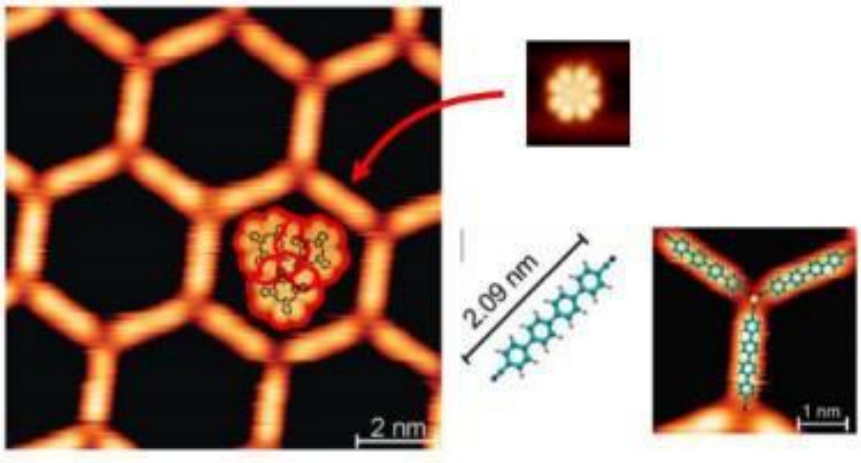

Fig. 5.1: Two-dimensional metal-organic network based on dicarbonitrile tetraphenyl linkers ($NC\text{-}Ph_4$ -CN) self-assembled with cobalt atoms on Ag(111) [3]. A $TbPc_2$ trimer obtained by atomic manipulation on a free surface by Amokrane et al. [5] visualized at the same scale and superposed to the original network image to show what a $TbPc_2$ trimer inside a pore would look like. The figure at the lower right shows a knot of the hexagonal network.

5.2 Self-assembly of Dicarbonitrile-polyphenyl molecular linkers ($NC\text{-}Ph_n\text{-}CN$) on Ag(111)

5.2.1 Dicarbonitrile-polyphenyl molecular linkers ($NC\text{-}Ph_n\text{-}CN$)

The molecular structure of Dicarbonitrile-polyphenyl is composed of n groups of phenyl (Ph) and two carbonitrile groups (CN) at each ends. The lengths of these molecular ligands vary from 1.7 to 3.2 nm (N ... N) by the number of phenyl groups incorporated (n = 3, 5, 6). The synthesis of these structures is based on a Suzuki coupling scheme involving the respective bis-

iodophenylene precursors and 4-phenylboronic acids in the presence of a catalytic amount of Pd (0) [6].

NC-Phn-CN linkers have many applications in organic chemistry, the physisorption of these structures on metallic surfaces has led to many studies in the formation of supramolecular networks. These supramolecular networks used to immobilize a variety of guest molecules. Host-guest chemistry in such two-dimensional (2D) porous networks will allow us to study the properties of molecules (for example SMM) confined in supramolecular cavities.

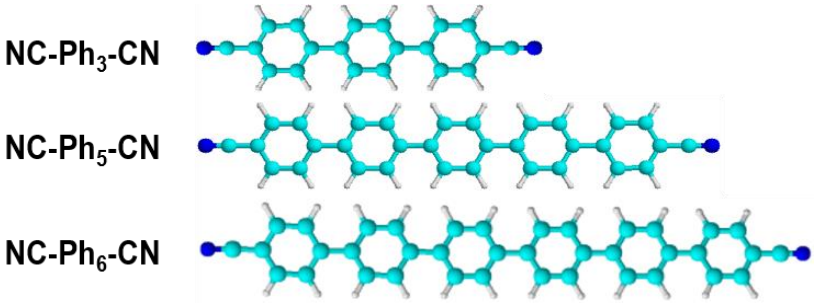

Fig. 5.2: Dicarbonitrile-polyphenyl Molecular structure of NC-Ph_n-CN : n = 3, dicarbonitrile-terphenyl molecule (NC-Ph_3-CN) ; n = 5, dicarbonitrile-pentaphenyl molecule (NC-Ph_5-CN) ; n = 6 dicarbonitrile-hexaphenyl molecule (NC-Ph_6-CN). Color code: Blue=Nitrogen; Cyan=Carbon; White=Hydrogen.

5.2.2 Self-assembly of dicarbonitrile terphenyl (NC-Ph_3-CN) on Ag(111)

The dicarbonitrile terphenyl linker is composed of 3 phenyls group and 2 carbonitrile group (one at each ends), its size is about 1.6 nm. On Ag(111), at the evaporation temperature of 430 K, the adsorption of the linkers on the surface leads to the formation of a regular organic network (Figure 5.3 (a)) where they self-arrange spontaneously according to a chevron phase [7] (Figure 5.3 (b)). This network is stable at temperatures below 380 K. In the similar network to one reported by Schlickum et al. [7] shown in Figure 5.3 (c), the interaction between adjacent molecular linkers is provided by the non-covalent forces between a carbonitrile endgroup and two adjacent phenyl groups. This interaction is periodic on the network.

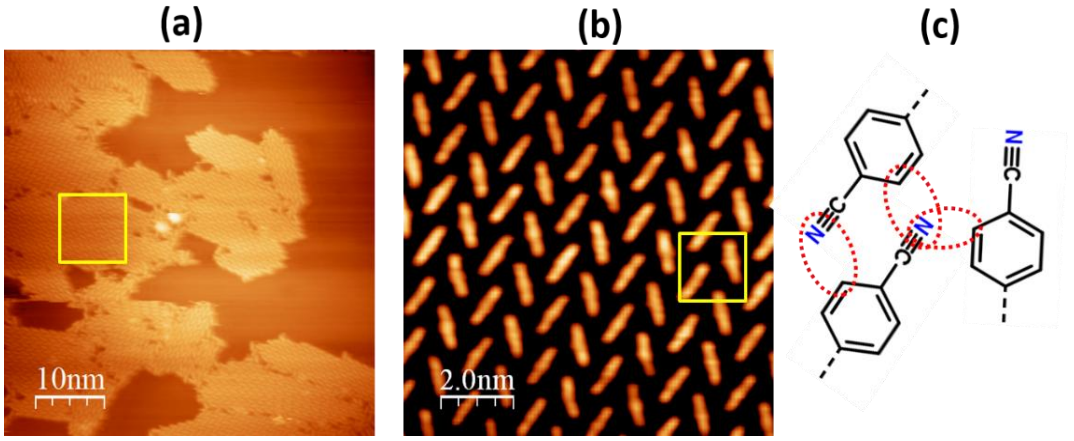

Fig. 5.3: (a) Topographic STM image of NC-Ph_3-CN linkers self-assembled on Ag(111). (b) Yellow square in (a), High – resolution STM image showing the molecular packing with chevron phase. (c) Yellow square in (b), corresponding schematic model showing the interaction (dashed red line) between adjacent carbonitrile endgroup and phenyl groups.

5.2.3 Self-assembly of dicarbonitrile pentaphenyl (NC-Ph_5-CN) on Ag(111)

The self-organized phases of NC-Phn-CN are strongly influenced by the size of the molecule [1]. In fact, in the case of dicarbonitrile pentaphenyl (NC-Ph_5-CN), the addition of two phenyls group in the molecule of the NC-Ph_3-CN base causes the change of the network architecture, where we distinguish four molecular arrangement phases (S, R, C and K) represented in Figure 5.4. Compared to previous studies [1], we notice the appearance of new phases of molecular arrangement, such as Square (Figure 5.4 a), Rhombic and Compact (Figure 5.4 b).

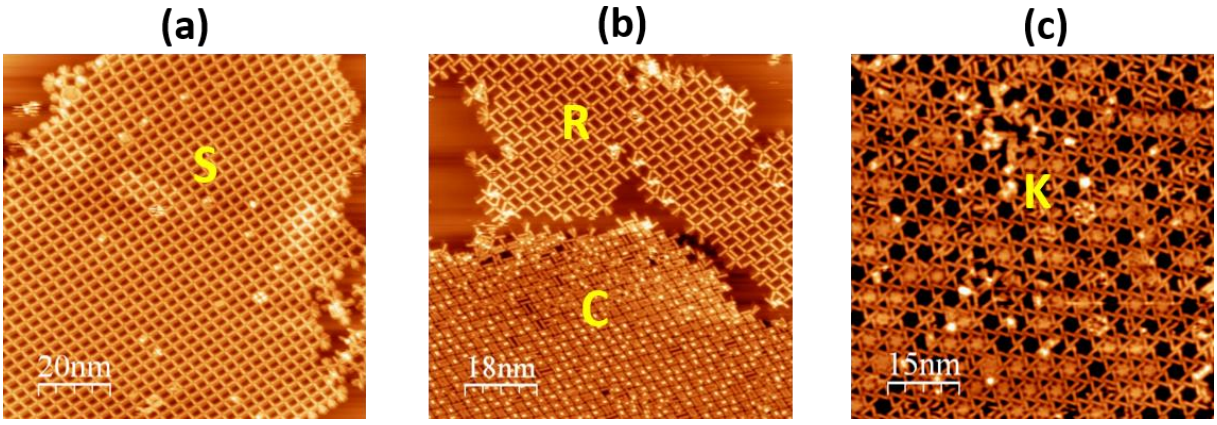

Fig. 5.4: Topographic STM images of NC-Ph_5-CN linkers self-assembled on Ag(11) showing the molecular packing with different phases : (a) Square (S); (b) Rhombic and Compact (R and C); (c) Kagome (K).

5.2.3.1 NC-Ph$_5$-CN self-assembled on Square phase

We assign the name square to the phase of molecular auto-arrangement in the nanoporous lattice observed in Figure 5.5 (a). In this phase, the adjacent molecules interact with each other by the non-covalent forces between the carbonitriles endgroup (Figure 5.5 (b)). Consequently, they form a periodic and stable network at temperatures below 380 K.

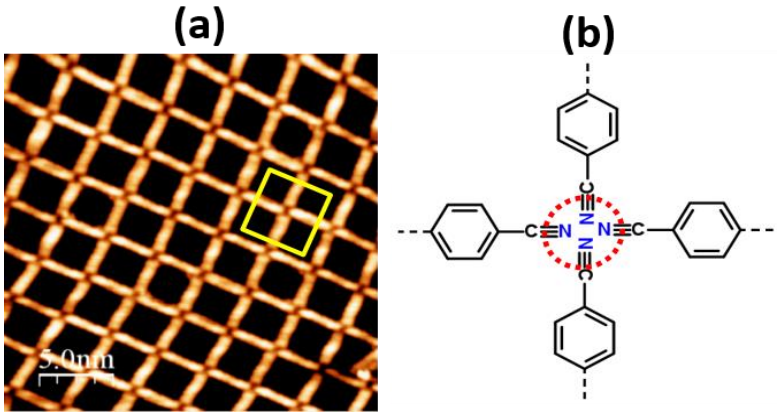

Fig. 5.5: (a) High – resolution STM image showing a square lattice of NC-Ph$_5$-CN linkers. (b) Yellow square in (a), corresponding schematic model showing the interaction (dashed red line) between adjacent carbonitriles endgroup.

5.2.3.2 NC-Ph$_5$-CN self-assembled on Rhombic phase

The second structure observed by STM presented in Figure 5.6 (a) is named rhombic. The periodic lattice in this phase is obtained by the non-covalent interaction between the carbonitrile endgroup and the phenyl group of adjacent molecules as shown in Figure 5.6 (b). The stability of this network is also proven at temperatures below 380 K following an annealing at this temperature.

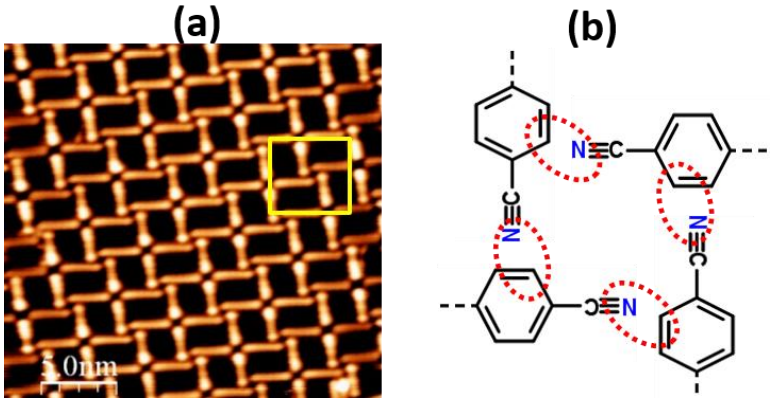

Fig. 5.6: (a) High – resolution STM image showing the rhombic molecular network of NC-Ph$_5$-CN linkers. (b) Yellow square in (a), corresponding schematic model showing the interaction (dashed red line) between adjacent carbonitrile endgroup and phenyl group.

5.2.3.3 NC-Ph_5-CN self-assembled on Compact phase

In this phase, the molecules form regular rows of three arranged vertically, separated by rows of three molecules arranged horizontally as shown in Figure 5.7, thus recalling the Rhombic structure but instead of one molecule there are three arranged in a package.

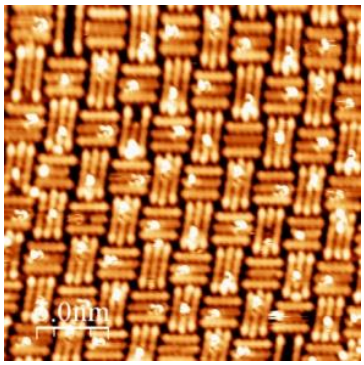

Fig. 5.7: High – resolution STM image showing the molecular packing in NC-Ph_5-CN network with compact phase.

5.2.3.4 NC-Ph_5-CN self-assembled on Kagomé phase

A fourth structure, the most complex one was observed in self-assembly of NC-Ph_5-CN on Ag(111) is the Kagome phase as shown in Figure 5.8 (a). In this phase, the molecules form patterns in the form of a 6-vertex star with a hexagonal cavity, hence the name Kagome [1]. The molecular lattice is formed by the specific non-planar nodes characterized by the rotation of the terminal Ph-CN groups and molecular flexure. Two types of cavities are identified on the network, one empty hexagonal cavity shown in Figure 5.8 (b) and another one where a molecular rotor is confined inside as shown in Figure 5.8 (c). D. Kühne et al [4] revealed the same situation in coordination networks $Co(NC\text{-}Ph_6\text{-}CN)_3$ where they interpreted that the molecular rotor is formed by three rotating NC-Ph_6-CN molecules in the cavity. The confined monomers are always attached to the network in a specific geometry, reflecting a surface templating effect and weak attractions between phenyl hydrogen and CN endgroups.

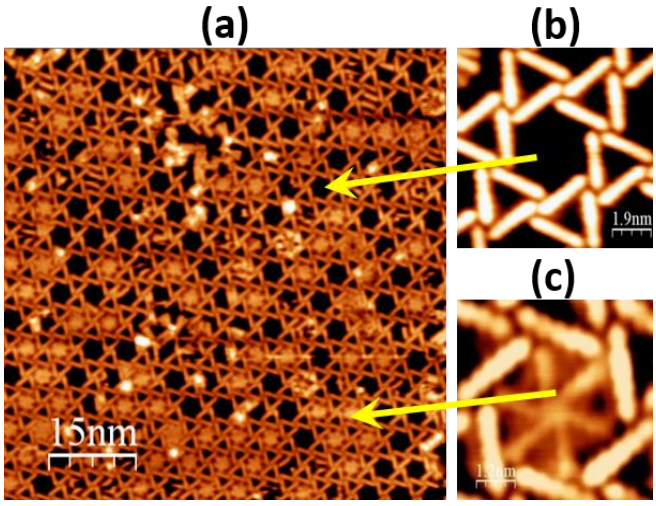

Fig. 5.8: (a) High – resolution STM image showing the molecular packing in NC-Ph_5-CN network with Kagomé phase. (b) The empty Kagome nanopore structure on network marked by yellow alloy. (c) Molecular rotor formed by NC-Ph_5-CN rotating molecules in the nanopore of the network.

5.2.3 Self-assembly of dicarbonitrile hexaphenyl (NC-Ph_6-CN) on Ag(111)

In this section, we topographically analyze the self-assembly of NC-Ph_6-CN molecule on Ag(111). This molecule is the longest in the molecular family of NC-Ph_n-CN (n = 3 - 6), its size of about 3 nm, allows adsorption according to a densely packed parallel phase on the silver surface as shown in Figure 5.9 (a), compared to the results of D. Kühne et al. [2] . In this phase, the molecular density is much higher than the density of the other structures (NC-Ph_3-CN and NC-Ph_5-CN) where the adjacent molecules have the same horizontal orientation on Ag(111) thus forming ordered molecular rows. The self-assembly is driven by the non-covalent interaction between adjacent carbonitrile endgroup and adjacent phenyls group as shown in Figure 5.9 (c).

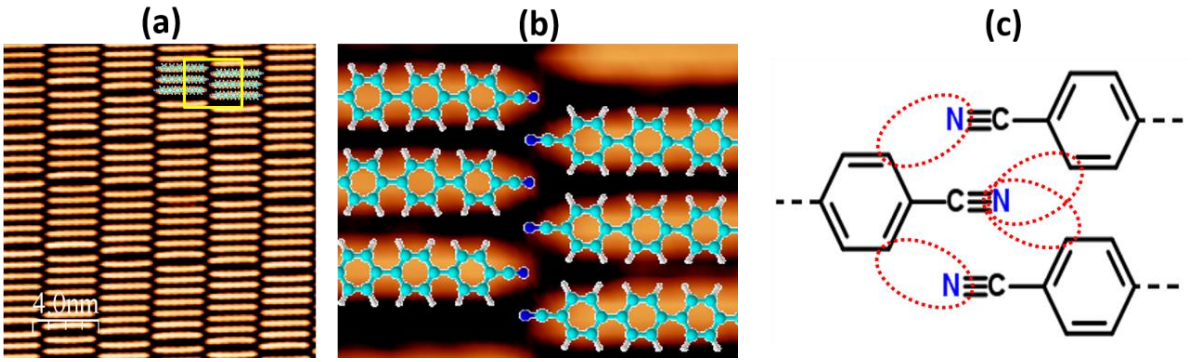

Fig. 5.9: (a) Topographic STM image of NC-Ph_6-CN linkers self-assembled on Ag(111). (b) Yellow square in (a), High – resolution STM image superimposed with molecular template showing the molecular packing with densely packed parallel phase. (c) Corresponding schematic model showing the interaction (dashed red line) between adjacent carbonitrile endgroup and phenyl groups.

5.3 Formation of 2D Co (NC-Ph_n-CN)$_3$ coordination network

According the coordination strategy reported by Schlickum et al. [3] and Stepanow et al. [8]. In this study we have reproduced the same metal-organic networks in order to use the nanopores for the confinement of SMM. The molecular linkers described before are used in combination with cobalt (Co) atoms to form a porous networks on Ag(111) as shown in Figure 5.10 (b). The coordination pattern in the network has a threefold symmetry of cobalt with three molecular ligands on Ag(111) as shown in the inset of Figure 5.10 (b). The Co atom center is coordinated by three carbonitriles endgroup, thus forming a honeycomb structure with hexagonal cavities spreading over long distances from the Ag(111) surface (up to a hundred nanometers). Due to a strong hybridization between the metal center and the Ag(111) substrate [7] involving a dipole interaction between the Co and Ag metals, the coordination network has a capacity to be stable at temperatures below 350 K this is observed after annealing cycles on the substrate.

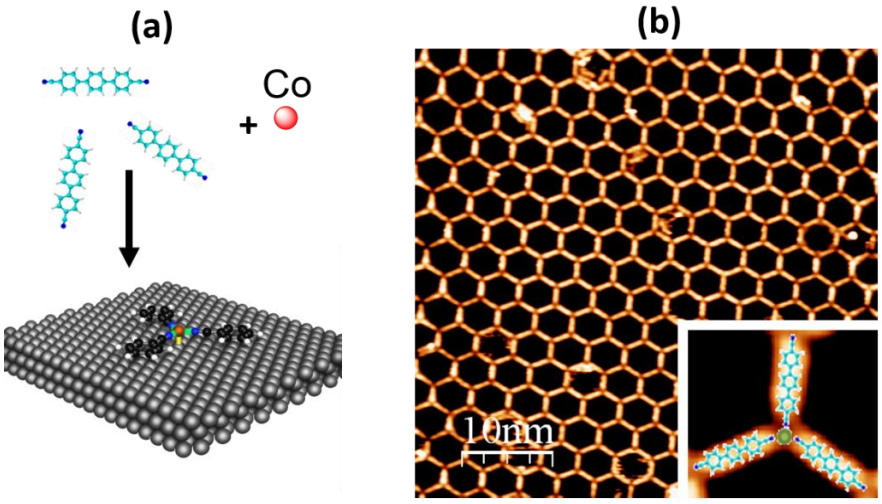

Fig. 5.10: (a) Simplified schematic illustrates the deposition of NC-Ph_n-CN molecular linkers and the co-deposition of Co atom on the Ag(111) surface. (b) High-resolution STM image of the honeycomb network of Co (NC-Ph_n-CN)$_3$ on Ag(111), the inset shows the STM topography of threefold Co(CN endgroup)$_3$ network node superimposed by corresponding templates.

Figure 5.11 shows two honeycomb networks that have been formed by coordination between cobalt atoms and NC-Ph_3-CN (Figure 5.11 (a)) and NC-Ph_6-CN (Figure 5.11 (b)) molecular linkers. However, the change in the length of the linker allows the tuning of the diameter (D) Co-Co of the porous nanomeshes network, it is about 4.2 nm (D1) for the network Co(NC-Ph_3-CN)$_3$ and 6.8 nm (D2) for the network Co(NC-Ph_6-CN)$_3$. As a result, the nanomeshe area is of 8 nm^2 and 24 nm^2 respectively.

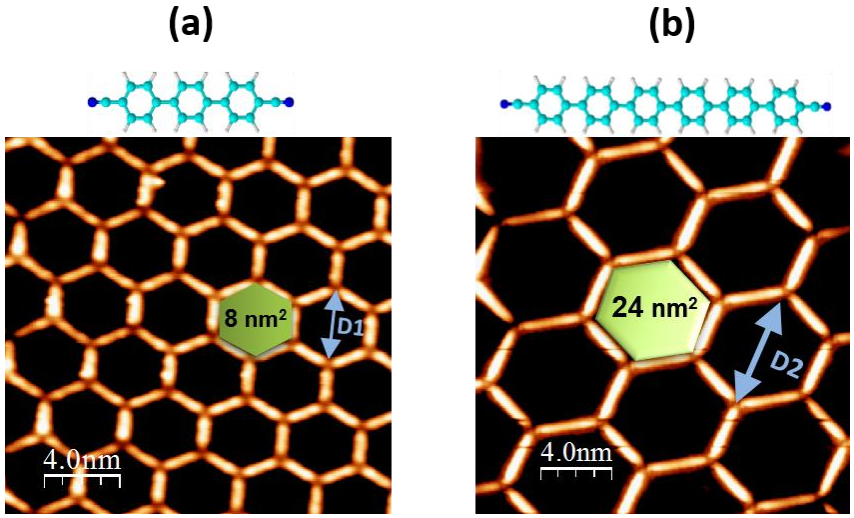

Fig. 5.11: (a) and (b) High-resolution STM image of the honeycomb networks of Co(NC-Ph_3-CN)$_3$ and Co(NC-Ph_6-CN)$_3$ respectively, showing the diameters (cyan area) and (green area) of porous nanomeshes of the two networks.

5.4 Addressing $TbPc_2$ in $Co(NC\text{-}Ph_3\text{-}CN)_3$ network nanopores

In this section, we have investigated the possibility to positioning the $TbPc_2$ SMM on the nanopores of $Co(NC\text{-}Ph_3\text{-}CN)_3$ network in order to get the Host-Guest structure as described in Figure 5.1. Technically, we use the metal-organic coordination network formed on Ag(111) and successively, under UHV and at room temperature, we evaporate the $TbPc_2$ molecules. At 77 K the small-scale STM image in Figure 5.12 (a) reveals that the single molecule adsorbed above the network. From the profile (Figure 5.12 (b) performed on the topographic image) we suggest that a strong interaction between the Tb metal center of the $TbPc_2$ molecule and the Co atom of the $Co(NC\text{-}Ph_3\text{-}CN)_3$ allows the molecule to localize on the Co-coordination node.

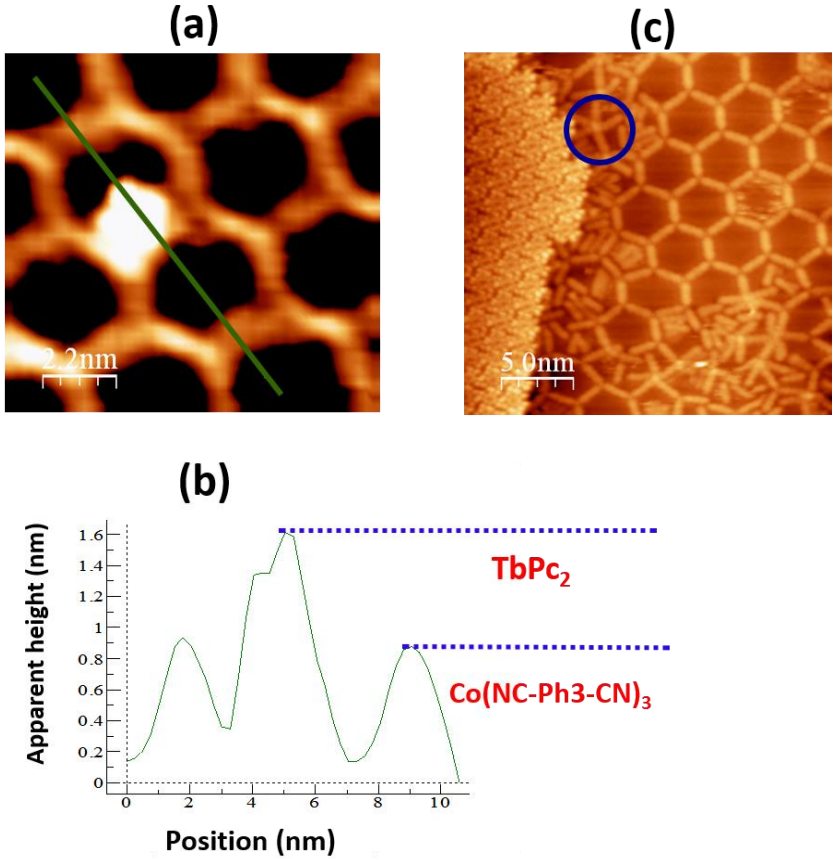

Fig. 5.12: High-resolution STM image of $TbPc_2$ SMM adsorption (a) on $Co(NC\text{-}Ph_3\text{-}CN)_3$ and (c) on Ag(111) surface. (b) Height profile extracted along the green line in (a) shows that the $TbPc_2$ is placed above the Co (NC- Ph_3-CN)$_3$ network.

After increasing the $TbPc_2$ coverage, as shown in the Figure 5.12 (c), the molecules are directly adsorbed on the Ag(111) surface and formed a large and well-ordered domain. The molecular domain thus observed is comparable to domain II observed in section 3.5 (Chapter 3). From previous studies on the growth of $TbPc_2$ on Ag(111), we have seen that

topographically the stability of molecular domains is highly influenced by the temperature at which the substrate is held. However, at the temperature of 77 K, the diffusion of the molecules on the surface causes a difficulty to record a well resolved topography. Given this information, we can suggest that in this case the instability of the $TbPc_2$ molecules generates a partial break of the $Co(NC\text{-}Ph_3\text{-}CN)_3$ network as shown in Figure 5.11 (c) rendering the confinement of these molecules in the nanopores impossible. A new coordination process between a Tb ion and five $NC\text{-}Ph_3\text{-}CN$ molecular linkers is instead observed (surrounded by a blue circle in Figure 5.12 (c)). This is due to a decomposition of $TbPc_2$ making a combination with free ligands possible.

Contrary to the well known host-guest system, of C_{60} confinement in the TMA network template [9,10], our experiments carried out on the confinement of $TbPc_2$ molecules on $Co(NC\text{-}Ph_3\text{-}CN)_3$ network does not lead to the desired result (Figure 5.1).

5.5 Conclusion

In this chapter, we have studied the formation of supramolecular networks on Ag(111) at molecular scale. The identification of self-organized phases and the adsorption geometry were performed on the nanostructures of $NC\text{-}Ph_n\text{-}CN$-(n=3,5,6) molecular linkers. We have also seen a difference in patterns of formed networks. The number of phenyl group incorporated in the molecule allows the molecule to interact differently with its neighbors in the network.

At room temperature, the combination with metallic atoms leads to a coordination interaction between the molecular linkers $NC\text{-}Ph_n\text{-}CN$ with Co atoms. Consequently, the formation of metal-organic networks with hexagonal nanopores is tunable with the change of the length of the molecular linker. The networks are thermally robust and extend over μm^2 large areas as single domains.

The localization of guest $TbPc_2$ SMM molecules in the nanopores of the host network seems complex at 77K. The deposition of the SMM molecules results in a breakdown of the coordination network, whereas, the overall architecture of the network becomes disordered and the threefold node of coordination might be instable.

In order to achieve a host-guest structure where $TbPc_2$ molecules play the role of the guest, it would be necessary both to obtain a stable organic network (for example as in the BTB organic molecules), this will allow us to limit all the Tb interactions and another magnetic metal, and on the other hand consider a co-deposition mode of $TbPc_2$ molecules on a substrate maintained at temperatures below 20 K to prevent its diffusion.

REFERENCES

[1] U.Schlickum, R. Decker, F. Klappenberger, G.Zoppellaro, S. Klyatskaya, W. Auwarter, S. Neppl, K. Kern, H. Brune, M. Ruben and J.V. Barth. Chiral Kagomé Lattice from Simple Ditopic Molecular Bricks. *J. Am. Chem. Soc*. 130, 11778-11782. (2008)

[2] D. Kühne, F. Klappenberger, R. Decker, U. Schlickum, H. Brune, S. Klyatskaya, M. Ruben and J. V. Barth, *J. Phys. Chem. C*, 113, 17851–17859. (2009)

[3] U. Schlickum, R. Decker, F. Klappenberger, G. Zoppellaro, S. Klyatskaya,M. Ruben, I. Silanes, A. Arnau, K. Kern, H. Brune, and J. V. Barth. Metal-organic honeycomb nanomeshes with tunable cavity size. *Nano Letter*, 7:3813– 3817. (2007)

[4] D. Kühne, F. Klappenberger, W. Krenner, S. Klyatskaya, M. Ruben and J. V. Barth, *Proc. Natl. Acad. Sci. U. S. A.* 107, 21332–21336. (2010)

[5] A. Amokrane, S. Klyatskaya, M. Boero, M. Ruben and J-P. Bucher. The Role of π-Radicals in the Spin Connectivity of Clusters and Networks of Tb Double-Decker Single Molecule Magnets, *ACS* Nano 11, 10750-10760, (2017).

[6] Collonge, J.; Buendia, J.; Sabadie, J. Bull. *Soc. Chem. Fr*. 1967, 4370– 4374.

[7] U. Schlickum, F. Klappenberger, R. Decker, G. Zoppellaro, S. Klyatskaya. M. Ruben, K. Kern, H. Brune and J. V. Barth. *J. Phys. Chem. C*, 114, 15602–15606. (2010)

[8] S. Stepanow, N. Lin, F. Klappenberger, G. Zoppellaro, M. Ruben, H. Brune, J. V. Barth and K. Kern. Surface-assisted assembly of 2D metal-organic networks that exhibit unusual threefold coordination symmetry. *Angew*. Chem. 46.710-713. (2007), 7:3813– 3817. (2007)

[9] J. Plas, O. Ivasenko, N. Martsinovich, M. Lackinger and S. De Feyter, *Chem. Commun*., 52, 68–71. (2016)

[10] D. Cui, J. M. MacLeod, M. Ebrahimi, D. F. Perepichka and F. Rosei, *Chem. Commun* 51, 16510. (2015)

General conclusion

Experimental investigations show that $TbPc_2$ molecules adopt molecular arrangements dependent on the nature of the supporting substrate. On the low reactive substrate like Au(111), the molecules tend to interact laterally with the neighboring molecules through their Pc ligand, the molecule-molecule interaction is the most dominant in this case. On Ag(111), the interaction of the molecule with the substrate becomes more important. We have observed a modification of the molecular geometry of the lattice where we measure an intermolecular distance greater than that measured on the Au(111), and consequently the molecular lattice becomes more extended on the surface. On Cu(111), a strong interaction of the molecule was topographically observed by scanning the surface at temperatures higher than 4.6 K. The molecule-substrate interaction is the most dominant in this case, what is proved by spectroscopic measurements (STS), showing that the electronic behavior of the isolated molecule is very similar to that inserted in a molecular domain.

We have determined by STS the HOMO and LUMO states of the $TbPc_2$ molecule resulting from 1) the weak interaction with the Au(111) surface and the lateral intermolecular interactions with the neighboring molecules, 2) the charge transfer coming from the surface of Ag(111) and 3) the strong hybridization of the molecule on the Cu(111) substrate. Moreover, a resonance in the tunnel conductance at the Fermi level has been demonstrated depending on the nature of the substrate. The interpretation of this observation lies in the appearance of a Kondo effect resulting from the π-radical carried by the ligand Pc when the molecule is deposited on Au(111) and Cu(111). This effect disappears when the molecule is adsorbed on Ag(111) under the charge transfer effect that occurs between the substrate and the molecule. In addition, a comparative study with YPc_2 on Au(111) enabled us to evaluate the impact of the π-electrons located on the Pc ligand on the 4f-electrons of the central ion. Nevertheless, we have been able to demonstrate that the same π-radical is present on the two molecules YPc_2 and $TbPc_2$. For the first time, a Kondo effect is detected on the center (Tb) of the molecule deposited on Cu(111) due to the hybridization of 4f-electrons of Tb^{3+} with the *spd* orbitals of the substrate.

We have studied a coverage large than a monolayer so that second ML adsorbed molecules are decoupled from the surface of Ag(111) and Cu(111). On Ag(111), we detect a Kondo effect on the ligand of the molecule in second ML, which is consistent if we consider

the pairing up of spin radicals on the ligand of the first ML. On Cu(111), no Kondo effect is detected on the molecule in the second ML. We suggest in this case that the spin-spin molecular interaction between the two monolayers through the Pc ligands is responsible for the appearance of spin radical on the ligand of the second ML.

Parallel to the main subject, an additional work has been carried out on the confinement de $TbPc_2$ in the metal-organic network with tunable nanopores of the $Co(NC\text{-}Ph_n\text{-}CN)_3$ type. After fabricating the network on the surface Ag(111), the deposition of $TbPc_2$ breaks off the network, with the impossibility of locating these molecules in the nanopores.

Rabei BARHOUMI

POSITIONING AND ADDRESSING SINGLE MOLECULE MAGNETS WITH AN STM TIP

Résumé

Les aimants moléculaires de type $TbPc_2$ avec leur anisotropie magnétique élevée associée à des temps de relaxation longs de l'aimantation sont de bons candidats pour le codage et l'enregistrement de l'information. Leur robustesse et leur propension à s'arranger en réseaux se prêtent bien à une étude de leur structure électronique et magnétique par STM/STS à très basse température (4.5 K). Dans ce travail de thèse, il a été possible de mettre en évidence un écrantage Kondo des électrons π et 4f de la molécule de $TbPc_2$ par les électrons du substrat métallique. Les propriétés magnétiques de la molécule dépendent de leur degré d'interaction avec le substrat et des interactions latérales avec les autres molécules. Ainsi le radical π de la molécule est préservé sur Au(111) mais disparait sur Ag(111) sous l'effet d'un transfert de charge entre le substrat et la monocouche moléculaire. Enfin, lorsque la molécule est en interaction forte avec le substrat de Cu(111), un accès direct aux états 4f de l'ion central de Tb est observé par STM comme le montre la détection d'un effet Kondo sur l'ion central de Tb.

Mots-clés: aimants moléculaires, effet Kondo, microscope à effet tunnel, spintronique, magnétisme des électrons 4f, interface métal-organique, intrication quantique.

Résumé en anglais

With their large magnetic anisotropy associated with long relaxation times of the magnetization, $TbPc_2$ molecular magnets are good candidates for encoding and recording data. Their robustness and their propensity to arrange into networks lend themselves well to a study of their electronic and magnetic structure by STM/STS at very low temperature (4.5 K). In this thesis work, it was possible to highlight a Kondo screening of the π and 4f electrons of the $TbPc_2$ molecule by the electrons of the metal substrate. The magnetic properties of the molecule depend on their degree of interaction with the substrate and lateral interactions with other molecules. Thus, the π radical of the molecule is preserved on Au (111) but disappears on Ag (111) under the effect of a charge transfer between the substrate and the molecular monolayer. Finally, when the molecule is in strong interaction with the Cu(111) substrate, a direct access to the 4f states of the central Tb ion by STM is possible as shown by the detection of a Kondo effect on the central Tb ion.

Keywords: Single molecule magnets, Kondo effect, scanning tunneling microscopy, spintronics, 4f-electron magnetism, metal-organic interface, quantum mechanical entanglement.